UNIVERSITY OF TWENTE.

# 28 GHz Gapwaveguide-based Phased Array Antennas for 5G Applications

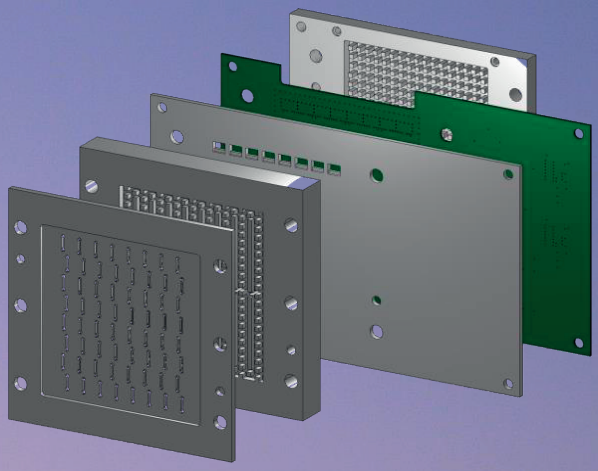

Alireza Bagherimoghim

PhD Thesis

# 28 GHz Gapwaveguide-based Phased Array Antennas for 5G Applications

by

Alireza Bagherimoghim

# 28 GHz Gapwaveguide-based Phased Array Antennas for 5G Applications

Dissertation

to obtain
the degree of doctor at the University of Twente,
on the authority of the rector magnificus,
prof. dr. ir. A. Veldkamp
on account of the decision of the graduation committee,
to be publicly defended
on Friday 22 September 2023 at 10:45h

by

Alireza Bagherimoghim

born on 14$^{th}$ of June 1991
in Tehran, Iran

This dissertation has been approved by:

| | |
|---|---|
| Promoter: | prof. dr. ir. A. B. J. Kokkeler |
| Co-promoter: | dr. A. Alayón Glazunov |

The research described in this thesis was carried out in the Radio Systems Group, which is part of the Faculty of Electrical Engineering, Mathematics and Computer Science at the University of Twente, Enschede, The Netherlands.

The author's position was funded by European Union's Horizon 2020 research and innovation programm under the Marie Skłodowska-Curie grant agreement No. 766231 — WAVECOMBE — H2020-MSCA-ITN-2017.

Copyright © 2023 by Alireza Bagherimoghim.

All rights reserved. No parts of this thesis may be reproduced, stored in a retrieval system or transmitted in any form or by any means without permission of the author. Alle rechten voorbehouden. Niets uit deze uitgave mag worden vermenigvuldigd, in enige vorm of op enige wijze, zonder voorafgaande schriftelijke toestemming van de auteur.

| | |
|---|---|
| ISBN (print): | 978-90-365-5737-5 |
| ISBN (digital): | 978-90-365-5738-2 |
| DOI: | 10.3990/1.9789036557382 |

Printed by Ipskamp Printing
Typeset in LaTeX 2ε

## Members of the graduation committee:

**Chairman & Secretary:**

| | |
|---|---|
| prof. dr. J. N. Kok | University of Twente |

**Promoter:**

| | |
|---|---|
| prof. dr. ir. A. B. J. Kokkeler | University of Twente |

**Co-promoter:**

| | |
|---|---|
| dr. A. Alayón Glazunov | University of Twente |

**Committee members:**

| | |
|---|---|
| prof. dr. ir. D. A. I. Marpaung | University of Twente |
| dr. ir. P. T. de Boer | University of Twente |
| prof. dr. E. Rajo Iglesias | University Carlos III of Madrid |
| prof. dr. ir. M. J. Bentum | Eindhoven University of Technology |
| dr. C. Bencivenni | Gapwaves AB |

# Summary

The fifth generation (5G) of mobile wireless communication aims to provide higher data capacity than the previous generations could. With large frequency bands already licensed at mmWaves, data rates of around 10 Gbit/s can be offered. However, these frequency bands lead to more free space path loss, for example, 20 dB more loss moving from 3 to 30 GHz. Phased array antennas integrated with low-loss antenna elements and high-power front-ends have drawn much attention to compensate for this increased loss.

State-of-the-art phased array antennas for mmWave 5G are designed with antenna elements based on a dielectric substrate and employ front-ends with CMOS and SiGe BiCMOS technology. The antenna elements based on a dielectric substrate typically show a high loss at mmWave frequencies and suffer from low bandwidth. The techniques to increase the bandwidth of such antenna elements usually add to the complexity of the structure by increasing the number of layers. This thesis aims to use gapwaveguide technology as the baseline for antenna element design, which is a low-loss, low-cost, and wideband transmission line at mmWave frequencies.

In this thesis, a phased array is designed with improved characteristics in terms of low antenna and front-end losses. The objective is to propose a cost-effective and scalable phased array while enhancing its complex structure. For 5G communication systems operating at 28 GHz, a high equivalent isotropic radiated power (EIRP) active phased array antenna is proposed. The antenna design is based on the gapwaveguide technology and consists of $16 \times 16$ single $45^\circ$ slant-polarized elements. The proposed design employs a low-complexity printed circuit board (PCB) structure with only six layers, i.e., half of existing wideband solutions. The array antenna incorporates up/down converter integrated circuits (UDCs) and $1 \times 4$ transceiver beamformer integrated circuits (BFICs). Moreover, a compact and highly efficient transition at the end of each channel of the BFICs has been designed to interconnect the antenna elements with the PCB. The antenna's front-end loss, which includes the feed line, mismatch, and ohmic losses, is only 1.3 dB. The array covers a scanning range of $\pm 60^\circ$ in the azimuth plane and $\pm 10^\circ$ in the elevation plane. The $S_{11} < -10$ dB frequency bandwidth is from $26.5 - 29.5$ GHz. The maximum EIRP of the antenna is 65.5 dBm at the saturation point. The presented design offers a compact, robust, and low-loss performance solution meeting the high

transmission power requirements of 5G applications. The transmit error vector magnitude (EVM) performance measurements show that the phased array supports a 31 dB EIRP dynamic range at a maximum 2% EVM when transmitting a 64-QAM modulated signal with 250 MS/s symbol rate at all scanning directions.

Power amplifiers with high output power have interesting applications in fulfilling the need for high power at mmWave 5G. Designing a phased array with such characteristics requires addressing challenges including power handling, thermal dissipation, and temperature stability. Therefore, a cost-efficient, high EIRP (60 dBm), large-bandwidth (26.5− 29.5 GHz) active phased array antenna system has been designed and experimentally verified. The proposed design methodology reduces production costs by employing GaN-based radio frequency front-ends with 31 dBm output power, allowing fewer antenna elements. A fully metallic gapwaveguide technology has been employed, achieving efficient heat dissipation per array's aperture area and low-loss easy-to-manufacture antenna elements. The phased array is realized by sub-arraying an $8 \times 8$ slot array antenna with horizontal polarization. A $\pm 60^{\circ}$ analog beamforming in the $E$-plane is demonstrated. The presented antenna is a potential candidate for compact-size, high-performance 5G base station antennas with excellent temperature stability.

Finally, the performance of hybrid digital-analog multi-beam systems employing the proposed phased array antennas is studied for 5G applications in indoor environments. Comprehensive numerical simulations focused on collocated and distributed phased array antenna deployments in indoor office environments are compared. A hybrid digital-analog multi-user multiple-input multiple-output (MU-MIMO) downlink communication system is considered. The evaluated figures of merit are the gain of the RF power amplifier, the per-user signal-to-interference-plus-noise ratio (SINR), and the resulting achievable sum rate capacity. This study uses measured beamforming radiation patterns from the two 28 GHz state-of-the-art phased array antennas. The channel models employed are the standardized statistical 3GPP 38.901 channel models implemented in the QuaDRiGa software. A beam selection algorithm is implemented to maximize the achievable sum rate, assuming either matched-filtering or zero-forcing precoding. Based on the results, we conclude that the distributed deployment scenario always shows a higher SINR and achievable sum rate capacity at the user locations.

In summary, this thesis contributes to the field of phased array antenna designs for mmWave 5G communication. The research presents innovative designs, characterizes their performance, and analyzes their suitability for 5G applications. The findings provide valuable insights: such as the advantages of using gapwaveguide technology for antenna element design in mmWave phased arrays, improving design methodology by relaxing the complexity and cost, proposal of a cost-efficient, high-power phased array antenna system with large bandwidth and high EIRP, and validation of the benefits of distributed deployment for indoor environments.

# Samenvatting

De vijfde generation (5G) mobiele draadloze communicatiesystemen streven naar het aanbieden van hogere datasnelheden dan vorige generaties. Met de grote bandbreedtes die beschikbaar zijn gekomen op de gelicenceerde milimetergolf (mmWave) banden kunnen datasnelheden van 10 Gbit/s worden aangeboden. Deze frequentiebanden leiden echter tot meer verliezen door de vrije ruimte, bijvoorbeeld 20 dB extra verlies bij een overgang van 3 naar 30 GHz. Het gebruik van fasegestuurde antennes (phased-arrays) met weinig verliezen en hoog vermogen front-ends is een goede optie om deze verliezen te compenseren.

State-of-the-art fasegestuurde antennes voor mmWave 5G zijn normaliter ontworpen met antenne elementen op basis van diëlektrische substraten. Daarbij worden voornamelijk front-ends gebruikt met CMOS- en SiGe BiCMOS technology. De antenne elementen op basis van deze diëlektrische substraten vertonen over het algemeen hoge verliezen bij mmWave frequenties en zijn problematisch vanwege hun kleine bandbreedte. Typische technieken om de bandbreedte van deze antennes te verbreden maken het ontwerp complexer en zorgen voor een toename van het aantal lagen van het substraat. Dit proefschrift beoogt gapwaveguide-technologie te gebruiken als basis voor antenne ontwerp. Deze technologie biedt lage verliezen, lage productie kosten en grote bandbreedtes in de mmWave frequentiebanden.

In dit proefschrift is allereerst, een fasegestuurde antenne ontworpen met verbeterde eigenschappen op het gebied van lage verliezen in de antenne elementen en in het front-end. Hiermee wordt een antenne systeem gepresenteerd dat kosten-effectief en schaalbaar is waarbij de complexe structuur verbeterd wordt. Een phased-array antenne voor communicatiesystemen voor 5G op 28 GHz wordt gepresenteerd met een hoog effectief isotroop gestraald vermogen (EIRP). Het antenne ontwerp is gebaseerd op gapwaveguide technologie and heeft $16 \times 16$ lineair 45° schuin gepolarizeerde elementen. Het voorgestelde ontwerp gebruikt een zes-laags printplaat (PCB) met lage complexiteit, waarmee het aantal lagen wordt gehalveerd vergeleken met reeds bestaande ontwerpen voor grote bandbreedte. De phased-array antenne bevat geintergreerde circuits voor het omhoog en omlaag converteren (UDCs). Ook bevat het systeem een $1 \times 4$ geintegreerd circuit als gecombineerde zender en ontvanger (BFICs). Bovendien is een compacte en hoog-efficiente overgang ontworpen voor de verbinding tussen de antenna en de BFICs om het signaal van de PCB

naar de antenne te leiden. Het verlies van het front-end van het antennesysteem is slechts 1.3 dB, waarbij verliezen van de transmissie-lijn het verschil in golf-impedantie en ohmse verliezen zijn inbegrepen. De antenne dekt een stuur-bereik van $\pm 60^\circ$ graden in het horizontale vlak (azimut) en $\pm 10$ graden in het verticale vlak (elevation). De $S_{11} < -10$ dB frequentie bandbreedteis tussen 26.5 en 29.5 GHz. Het maximale EIRP van de antenne is 65.6 dBm bij het verzadigingspunt. Het voorgestelde ontwerp biedt een compacte en robuuste oplossing die voldoet aan de hoge eisen rondom de vermogensoverdracht in 5G applicaties. De Error Vector Magnitude (EVM) meeting laat zien dat de phased-array antenne een 31 dB EIRP gebied ondersteunt met een maximum van 2% EVM. Deze waarde geldt voor een 64-QAM modulatie schema met 250 MS/s symbool snelheid voor alle scanning hoeken.

Hoog vermogen versterkers hebben interesante toepassingen in het voldoen aan de vraag naar hoog vermogen voor mmWave 5G. Het ontwerp van phased-array antennes met deze eigenschappen vereist verschillende oplossingen, waaronder voor het omgaan met vermogen, hitte dissipatie en temparatuurstabiliteit. Hiervoor is een kosten-efficient, hoog vermogen (60 dBm), breedbandige (26.5 - 29.5 GHz), actieve phased-array antenne ontworpen en experimenteel geverifieerd. De gebruikte ontwerpmethode verlaagt de productieprijs door gebruik te maken van GaN front-ends met 31 dBm uitgangsvermogen, het hoge vermogen geeft de mogelijkheid om minder antenne elementen te gebruiken en zodoende de kosten te drukken. Een volledig metalen gapwaveguide antenne is gebruikt, hetgeen een uitstekende warmte dissipatie geeft per antenne. De ontworpen antennes vertonen lage verliezen en bieden eenvoudige methodes voor het productieproces. Het phased-array systeem is gerealiseerd door het samenvoegen van kleinere antenne elementen waarmee een $8 \times 8$ slotantenne is ontworpen, met een horizontale polarisatie. Een stuurbereik van $\pm 60^\circ$ is gedemonstreerd in het electrische vlak door het gebruik van analoge faseverschuivers. De gepresenteerde antenne is een potentiële kandidaat voor een compact 5G base station met uitstekende thermische stabiliteit.

Tot slot zijn in dit proefschrift de prestaties van hybride digitaal-analoog, meervoudig-stralende, phased-array systemen bestudeerd voor 5G applicaties in indoor omgevingen. Uitgebreide numerieke simulaties zijn uitgevoerd om het verschil tussen op-één-plek-geconcentreerde en gedistribueerde antennesystemen te onderzoeken in kantoor omgevingen. Een hybride digitaal-analoog Multi-User MIMO (MU-MIMO) downlink communicatiesysteem is hiervoor bestudeerd. De waarden die zijn geëvalueerd zijn de versterking door de RF versterker, de verhouding tussen signaal-en-interferentie-plus-ruis (SINR) en de resulterende totale capaciteit. Deze studie neemt de stralingspatronen in acht van de twee state-of-the-art phased-array antenne systemen die eerder zijn geintroduceerd. In deze studie zijn de gestandaardiseerde statistische 3GPP 38.901 kanaal modellen zoals geimplementeerd in de QuaDRiGa software gebruikt. Een bundelselectie algoritme is geimplementeerd voor het maximalizeren van de haalbare capaciteit, met de aanname van matched-filtering of zero-forcing in de precodering. Op basis van deze resultaten, kan de conclusie worden

getrokken dat gedistribueerde antennesystemen een hogere SINR vertonen en een hogere haalbare capaciteit bij de gebruikers hebben.

Samengevat, draagt deze scriptie bij aan het ontwerp van phased-arrays voor mmWave 5G communicatie. Het onderzoek presenteert innovatieve ontwerpen, karakterisatie van hun eigenschappen en analiseert de geschiktheid voor 5G toepassingen. De bevindingen bieden waardevolle inzichten, zoals de voordelen van de gapwaveguide technologie for antenne elementen in de mmWave frequentiebanden, verbetering in de ontwerpmethodes door het verlagen van complexiteit en kosten, voorstellen voor kosten-efficiënte hoog-vermogen phased-array antennesystemen met grote bandbreedte, en de validatie van de voordelen voor het gebruik van gedistribueerde systemen voor indoor omgevingen.

# Acknowledgments

At the end of this journey, I'm deeply grateful to the many individuals who supported, guided and contributed to this thesis. Their efforts, from mentors to friends, have shaped the growth and outcome of this work.

First, I would like to express my deepest appreciation to my main supervisor Senior Associate Professor Andrés Alayón Glazunov for the opportunity to this fruitful PhD journey. His immense support, constructive guidance, and unwavering encouragement have been very valuable throughout this project. Thanks for the interesting discussions, critical comments on my manuscripts, and your patience. You were not only an exceptional supervisor, but also a great friend with whom I could enjoy pleasant conversations and share a relaxing drink after work. I am also deeply thankful to Dr. Carlo Bencivenni, my supervisor at Gapwaves, for his exceptional mentorship, continuous support, insightful feedbacks, and brilliant ideas that have significantly shaped this endeavor and taught me how to think critically. Additionally, I extend my thanks to Adjunct Professor Thomas Emanuelsson, my co-supervisor at the beginning of this journey, for his initial guidance and contribution.

I would like to extend my sincere appreciation to my colleagues at Gapwaves, specially Lars-Inge Sjöqvist and Marcus Hasselblad, for graciously hosting me during my PhD journey. Your support has been instrumental in shaping all the dimensions of my research. The opportunity to work, immerse myself in a dynamic industry environment, and access valuable resources has significantly enriched my experience.

Furthermore, I wish to specially thank Professor André Kokkeler, for expert advices, valuable help, and constructive feedbacks, during the last year of my PhD. I would like to express my gratitude to Professor Christian Fager, Dr. Parastoo Taghikhani, and Dr. Jose-Ramon Perez-Cisneros, for the short but incredibly fruitful collaboration at the Microwave Electronics Laboratory at Chalmers University of Technology.

In the early stages of my PhD journey, I encountered a profound personal challenge that seemed insurmountable. During this tough period, a guiding light emerged in the form of Mrs. Charlotte Elmquist, whose proficient support and compassionate understanding provided me with the strength to overcome the obstacles before me. Her encouragement, patience, and genuine care were a lifeline that helped me navigate through the darkness. I am profoundly grateful

for her presence during a time when it mattered most. I am forever indebted for her immeasurable impact on both my academic journey and personal well-being.

My special thanks to my friends and colleagues, Hanna, Abolfazl, Magnus, Coen, Abbas, Sadegh, Esperanza, Daniel, Johan, Martin, Julius, Philip, Juan-Luis, and Björn, for the shared moments, collaboration, and collective spirit that have made my experience at Gapwaves exceptionally enriching. Your friendship and shared goals have played a significant role in shaping my professional journey. I would like to thank my PhD colleagues, Warren and Mohammad, for the enjoyable moments both at work and afterwork time.

I want to express my heartfelt gratitude to my friends all over the world, Jafar, Mohammadreza T., Ali, Mehdi, Firooz, Ehsan, Amir, Raha, Elham, Maryam, Vahid, Mohammadreza N., Mohammad, Homa, Samira, Mandana, and, Soroush for the invaluable friendship that has been an essential part of my PhD journey. Your presence has added a bright and joyful dimension to the challenges and successes. A big thanks goes to Meysam for his helps before and after moving to Sweden.

Last but not least, I would like to express my deepest gratitude to my lovely parents and wonderful brothers for always supporting, encouraging, and being there for me. Your presence, whether near or far, has been a source of comfort and reassurance needed to navigate the challenges and celebrate the successes.

*Alireza*
*Gothenburg, Sweden*
*August 2023*

# List of publications

## Publications related to this thesis

[A] **A. Bagheri**, H. Karlsson, C. Bencivenni, M. Gustafsson, T. Emanuelsson, M. Hasselblad, A. A. Glazunov, "A 16×16 45° Slant-Polarized Gapwaveguide Phased Array with 65 dBm EIRP at 28 GHz," *IEEE Trans. Antennas Propag.*, vol. 71, no. 2, pp. 1319–1329, Feb. 2023, doi: 10.1109/TAP.2022.3227718.

[B] **A. Bagheri**, H. Karlsson, C. Bencivenni, A. Haddadi, T. Emanuelsson, A. A. Glazunov, "Microstrip to Ridge Gap Waveguide Transition for 28 GHz Steerable Slot Array Antennas," *Eur. Conf. Antennas Propag*, Copenhagen, Denmark, 2020, pp. 1–4, doi: 10.23919/EuCAP48036.-2020.9135076.

[C] **A. Bagheri**, C. Bencivenni, A. A. Glazunov, "mmWave Array Antenna based on Gap Waveguide Technology for 5G Applications," *Int. Conf. Electromagn. Adv. Appl.*, Granada, Spain, 2019, pp. 0492–0494, doi: 10.1109/ICEAA.2019.8878978.

[D] **A. Bagheri**, J. Petersson, A. Haddadi, A. A. Glazunov, "A ±45° Dual-Polarized Antenna for 5G mmWave Applications Based on Gap Waveguide Technology," *Int. Symp. Antennas Propag.*, Xi'an, China, 2019, pp. 1–3.

[E] **A. Bagheri**, H. Karlsson, C. Bencivenni, JR. Perez-Cisneros, P. Taghikhani, C. Fager, A. A. Glazunov, "TX Beamforming EVM Performance of a 65 dBm-EIRP Slant-Polarized Gapwaveguide Phased Array at 28 GHz," *Eur. Conf. Antennas Propag*, Florence, Italy, 2023, pp. 1–4. 10.23919/EuCAP57121.2023.10133798.

[F] **A. Bagheri**, C. Bencivenni, M. Gustafsson, A. A. Glazunov, "A 28 GHz 8×8 Gapwaveguide Phased Array employing GaN Front-end with 60 dBm EIRP," *IEEE Trans. Antennas Propag.*, vol. 71, no. 5, pp. 4510–4515, May 2023, doi: 10.1109/TAP.2023.3240837.

[G] **A. Bagheri**, C. Bencivenni, A. A. Glazunov, "Performance Analysis of mmWave 5G Analog Beamforming Phased Array Antennas in Indoor Environments - Collocated vs. Distributed Deployment," *Under review at Frontiers in Communications and Networks.*

# Other publications

## Papers

[H] W. Y. Yong, A. Haddadi, **A. Bagheri**, T. Emanuelsson, A. A. Glazunov, "Wideband Cavity-Backed Slot Subarray Fed by Gap Ridge Waveguide for 5G mmWave Base Station," *Int. Symp. Antennas Propag.*, Xi'an, China, 2019, pp. 1–3.

[I] G. Meulman, **A. Bagheri**, A. A. Glazunov, "A 2-layer 45°-Slant-Polarised Phased Array Antenna with Baffles Based on Gap Waveguide Technology for mmWave 5G Systems," *Int. Symp. Antennas Propag.*, Osaka, Japan, 2020, pp. 575–576, doi: 10.23919/ISAP47053.2021.9391397.

[J] W. Y. Yong, A. Vosoogh, **A. Bagheri**, C. V. de Ven, A. Haddadi; A. A. Glazunov, "An Overview of Recent Development of the Gap-Waveguide Technology for mmWave and Sub-THz Applications," in IEEE Access, vol. 11, pp. 69378-69400, 2023, 10.1109/ACCESS.2023.3293739.

## Patents

[K] **A. Bagherimoghim**, A. Haddadi, and J. Petersson, "A dual polarized antenna," Oct. 2020, SE Patent SE543201C2.

[L] **A. Bagherimoghim**, C. Bencivenni, and H. Karlsson, "Rotated Ridge Waveguide Antenna," Jun. 2022, SE Patent SE544515C2.

# List of acronyms

| | |
|---|---|
| **3GPP** | 3rd Generation Partnership Project |
| **4G/5G** | 4th/5th Generation of Wireless Communication |
| **ADC** | Analog to Digital Converter |
| **AWG** | Arbitrary Waveform Generator |
| **AWGN** | Additive White Gaussian Noise |
| **AoA** | Angle of Arrival |
| **AoD** | Angle of Departure |
| **BFIC** | Beamforming IC |
| **BS** | Broadside |
| **BiCMOS** | Bipolar CMOS |
| **CDF** | Cumulative Distribution Function |
| **CMOS** | Complementary Metal Oxide Semiconductor |
| **CSI** | Channel State Information |
| **DAC** | Digital to Analog Converter |
| **EBG** | Electromagnetic Bandgap |
| **EIRP** | Effective Isotropic Radiated Power |
| **EU** | European Union |
| **EVM** | Error Vector Magnitude |
| **EoA** | Elevation of Arrival |
| **EoD** | Elevation of Departure |
| **GW** | Gapwaveguide |
| **GaN** | Gallium Nitride |
| **HPBW** | Half-Power Beamwidth |
| **IC** | Integrated Circuits |
| **IF** | Intermediate Frequency |

| | |
|---|---|
| **LNA** | Low Noise Amplifier |
| **LO** | Local Oscillator |
| **LOS** | Line of Sight |
| **MF** | Match Filtering |
| **MIMO** | Multiple-Input Multiple-Output |
| **mmWave** | millimeter-wave |
| **MU-MIMO** | Multi User MIMO |
| **NLOS** | Non-Line of Sight |
| **OTA** | Over the Air |
| **P1dB** | 1 dB Output Power Compression Point |
| **PA** | Power Amplifier |
| **PAA** | Phased Array Antenna |
| **PAE** | Power Added Efficiency |
| **PCB** | Printed Circuit Board |
| **PEC** | Perfect Electric Conductor |
| **PLE** | Path Loss Exponent |
| **PMC** | Perfect Magnetic Conductor |
| **PML** | Perfect Matched Layer |
| **QAM** | Quadrature Amplitude Modulation |
| **QTEM** | Quasi-TEM |
| **QuaDRiGa** | QUAsi Deterministic RadIo channel GenerAtor |
| **RF** | Radio Frequency |
| **RFFE** | RF Front-end |
| **RGW** | Ridge Gapwaveguide |
| **RMS** | Root Mean Square |
| **Rx** | Receiver |
| **SINR** | Signal to Interference plus Noise Ratio |
| **SLL** | Side Lobe Level |
| **SNR** | Signal to Noise Ratio |
| **SPI** | Serial Peripheral Interface |
| **SR** | Sum Rate |
| **SiGe** | Silicon Germanium |

| | |
|---|---|
| **T/R** | Transmit/Receive |
| **TEM** | Transverse Electromagnetic |
| **TRP** | Total Radiated Power |
| **Tx** | Transmitter |
| **UDC** | Up/Down Converter |
| **UE** | User Equipment |
| **VGA** | Variable Gain Amplifier |
| **VNA** | Vector Network Analyzer |
| **XPR** | Cross Polarization Ratio |
| **ZF** | Zero Forcing |

# Contents

**Summary** v

**Samenvatting** vii

**Acknowledgments** xi

**List of publications** xiii

**List of acronyms** xv

**1 Introduction** 1
- 1.1 mmWave 5G . . . 1
- 1.2 Phased Array Antennas for 5G mmWave Applications . . . 3
  - 1.2.1 State of the Art . . . 5
  - 1.2.2 Challenges at mmWave . . . 10
- 1.3 Gapwaveguide Technology . . . 11
- 1.4 Thesis Motivation and Contribution . . . 13
- 1.5 Thesis Outline . . . 14

**2 Gapwaveguide-based Passive Component Design at 28 GHz** 15
- 2.1 Introduction . . . 15
- 2.2 Pin and Ridge Gapwaveguide Design . . . 16
- 2.3 Top PCB Transition . . . 17
- 2.4 Through PCB Transition . . . 20
- 2.5 Horizontally Polarized Antenna Element . . . 21
  - 2.5.1 Integration with Top PCB Transition . . . 23
- 2.6 Dual 45°-slant Polarized Antenna Element . . . 25
- 2.7 45°-slant Polarized Antenna Element for Array Antenna . . . 29
  - 2.7.1 Integration with Through PCB Transition . . . 31
- 2.8 Summary and Conclusions . . . 34

**3 Gapwaveguide-based Large High-EIRP Phased Array Antenna at 28 GHz** 37
- 3.1 Introduction . . . 37

3.2 Phased Array Antenna Design . . . . . 39
3.3 Phased Array Prototype Measurements . . . . . 41
3.3.1 Calibration Measurements . . . . . 41
3.3.2 Radiation Pattern Measurements . . . . . 42
3.3.3 EIRP Measurements . . . . . 46
3.3.4 Comparison with the State-of-Art . . . . . 47
3.4 EVM Verifications . . . . . 50
3.4.1 Measurement Setup . . . . . 50
3.4.2 Results and Analysis . . . . . 50
3.5 Summary and Conclusions . . . . . 53

**4 Gapwaveguide-based High Power Phased Array Antenna at 28 GHz 57**
4.1 Introduction . . . . . 57
4.2 Phased Array Design . . . . . 58
4.2.1 Power Budget Considerations . . . . . 58
4.2.2 Front-end Design . . . . . 62
4.2.3 Antenna Element and Transition Design . . . . . 63
4.3 Calibration and Measurements . . . . . 65
4.4 Summary and Conclusions . . . . . 70

**5 Performance Analysis of mmWave 5G Analog Beamforming Phased Array Antennas in Indoor Environments - Collocated vs. Distributed Deployment 73**
5.1 Introduction . . . . . 73
5.2 System Model and Figures of Merit . . . . . 75
5.2.1 System Model . . . . . 75
5.2.2 Figures of Merit . . . . . 77
5.3 Propagation Channel Models and Simulation Scenarios . . . . . 78
5.3.1 Channel Models . . . . . 78
5.3.2 Channel Emulation in QuaDRiGa . . . . . 80
5.3.3 Beam Selection for Channel Matrix Building . . . . . 81
5.4 Simulation Scenarios and Simulation Steps . . . . . 82
5.4.1 Collocated vs. Distributed Antenna Systems . . . . . 82
5.4.2 Simulation Steps . . . . . 84
5.5 Simulation Results and Analysis . . . . . 86
5.5.1 Path Gain . . . . . 86
5.5.2 RF PA Gains . . . . . 87
5.5.3 Received Signal, Interference and SINR . . . . . 87
5.5.4 Achievable Sum Rate . . . . . 89
5.6 Summary and Conclusions . . . . . 91

**6 Conclusions and Directions for Further Research 97**
6.1 Conclusions . . . . . 98
6.2 Directions for further research . . . . . 100

**A Mathematical derivations and proofs** **103**
A.1 Derivation of SINR formula . . . . . 103
A.2 Relation between $G_{RF}$ and transmit signal powers . . . . . 104
A.3 Proving $\text{SINR}_k$ is an increasing function of $G_{RF}$ . . . . . 105

**Appendix**

**References** **106**

# Chapter 1

# Introduction

## 1.1 mmWave 5G

Since the initial rollout of the fifth-generation technology standard for broadband cellular networks (5G) in 2019, specific requirements on availability, latency, and reliability have been targeted. The improvements that 5G is expected to bring to mobile broadband services include 10- to 100-fold higher data rates and 1,000-fold higher data volumes. To address the demand for more data and performance, 5G radio frequency bands were expanded. All the frequencies previously occupied by 4G are now included, along with additional frequencies up to 6 GHz (Sub-6, also known as FR1) and the high band (mmWave, also known as FR2) spectrums [1].

Each of the 5G low-, mid-, and high-bands have unique speed and range characteristics. Because of the lower frequency characteristic of the low bands (600 to 2600 MHz), this spectrum is particularly well-suited to providing wide area and long-range coverage. 5G mid-bands offer increased capacity, albeit over a shorter distance than low-bands. They typically operate at frequencies ranging from 2300 to 6000 MHz and are suitable for massive Multiple-Input Multiple-Output (MIMO) technology deployments. 5G high bands (found in the 24–40 GHz range) provide large amounts of spectrum and capacity over short distances. They also use massive MIMO to increase capacity and coverage [1].

The allocated FR2 spectrums are exceptionally wide, with at least 800 MHz bandwidth. Pioneering markets such as the United States, Korea, and Japan recognized the 26.5-29.5 GHz (n257, also known as the 28 GHz band) spectrum for 5G use very early on. Later, the World Radio-communication Conference (WRC-19) agreed that the frequency bands 24.25-27.5 GHz (n258) and 37-43.5 GHz (n260 and n259) should be internationally designated for 5G. Such wide bandwidth allocations allow for higher capacity delivery and better handling of peak rates. For the 5G mmWave to be deployed within wide spectrum allocations, large carrier spacings in the frequency domain are

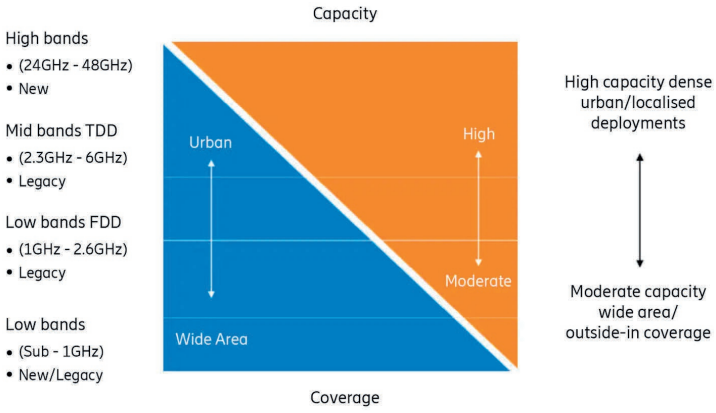


Figure 1.1: The capacity and coverage characteristics of 5G radio frequency range [1].

defined. These large carriers allow shorter transmission time intervals and lower radio-interface latency, enabling them to introduce and support low-latency-sensitive applications [1].

The potential of mmWave technology is accompanied by significant challenges, including hardware design challenges such as active and passive RF components, high path loss, and blocking effects. It is envisioned that the antennas will be connected to RF front-end units that support from 4 to 24 antennas each and, ideally, provide a power amplifier (PA), low noise amplifier (LNA), switch, phase shifter, and variable gain amplifier (VGA) for each antenna. A number of these RF front-end components will then connect with RF transceivers, responsible for signal generation, modulation, and demodulation [2]. Traditional transmission lines, such as hollow waveguide and substrate-based planar technologies, do not fulfill the design and feasibility requirements for passive components such as high-Q band-pass filters and slot array antennas [3]. Free-space path loss is frequency sensitive and grows with the square of the carrier frequency. As a result, increasing the carrier frequency from 3 to 30 GHz will result in a 20 dB power loss, independent of the transmitter-receiver distance. Therefore, we need to use antenna systems with high directive gain or increase the power of the transmitting signal. Electromagnetic waves diffract less over barriers much greater than their wavelength. Links in mmWave are susceptible to obstructions (e.g., humans and furniture) due to their short wavelength [4].

Beamforming is an essential technique in mmWave communication to mitigate the impact of high path loss, losses caused by rain and oxygen absorption, and the higher noise floor associated with a larger signal bandwidth. Beamforming in the transmission is a process that increases the signal level at the receiver location by adjusting the phase and amplitude of transmitting antennas. Similarly, in reception, the signal level increases by adjusting the phase and amplitude of the receiving elements. Beamforming must be considered

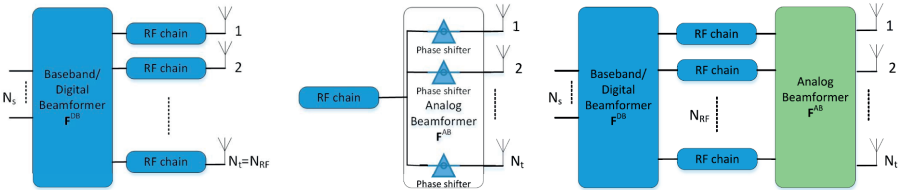


**(a)** Digital beamforming **(b)** Analog beamforming **(c)** Hybrid beamforming

Figure 1.2: Beamforming architectures in mmWave massive MIMO systems [6].

to counter the propagation challenges by concentrating the power in a beam steered toward the user. Along with high directivity in beamforming, the total conductive power needs to be increased. The application specifies the precise power level that must be transmitted to each antenna. The link budget determines the effective isotropic radiated power (EIRP) requirements, which vary for handsets, access points (user premises equipment), small cell base stations, and backhaul. The EIRP requirements for access points or base stations are currently expected to be in the 45–60 dBm range [2].

It was previously thought that frequency bands above 6 GHz were unsuitable for mobile communications due to high propagation losses. Signals at mmWaves are also attenuated by the human body, in addition to walls, foliage, and other obstacles. Therefore, the mmWave mobile deployment framework is expected to be through small cells, as the propagation conditions at higher frequencies have a direct impact on the coverage per cell. The result will be more compact and dense mmWave cells. Moreover, it is anticipated that mmWave will coexist in tight integration with 5G deployments below 6 GHz and 4G LTE [5].

## 1.2 Phased Array Antennas for 5G mmWave Applications

Different beamforming methods are employed on large antenna arrays, and their simplified sketches are shown in Fig. 1.2. Analog beamforming can direct a single data stream using phase shifters and variable-gain amplifiers at RF. This beamforming technique can be implemented with low complexity and power consumption, but it does not suit the massive MIMO communication needs. In contrast, baseband digital beamforming in MIMO systems demands a separate RF chain for each antenna to transmit and/or receive multiple data streams. Digital beamforming has a high power consumption and high cost for mixed-signal and RF chains (ADC/DAC, data converters, mixers, etc.) at mmWave frequencies. Digital beamforming offers great flexibility in terms of implementing efficient beamforming algorithms.

Several studies have proposed a hybrid beamforming architecture based on

Table 1.1: Comparison of beamforming techniques for mmWave massive MIMO communication [7]

| **Features** | **Analog beamforming** | **Digital beamforming** | **Hybrid beamforming** |
|---|---|---|---|
| Number of streams | Single | Multi | Multi |
| Number of users | Single | Multi | Multi |
| Hardware requirement | Least; one RF chain only | Highest; the number of RF chains equals the number of transmit antennas | Intermediate; the number of RF chains less than the number of transmit antennas |
| Energy consumption | Least | Highest | Intermediate |
| Cost | Least | Highest | Intermediate |
| Performance | Least | Optimal | Near-Optimal |
| Suitability for mmWave massive MIMO | Unsuitable; no multi-user | Impractical; prohibitive cost and high energy consumption | Practical and realistic |

the advantages and disadvantages of analog and digital beamforming [6–9]. The goal of hybrid beamforming by combining an analog RF beamformer with a digital baseband beamformer is to reduce the number of RF chains. In turn, it reduces complexity and energy consumption and provides near-optimal performance close to that of pure digital beamforming [10]. The mmWave wireless channel does not have rich multipath propagation characteristics at short distances or in line-of-sight channels with directive antennas. It offers a few paths between TX and RX. These reasons make the hybrid beamforming architecture more suitable for mmWave massive MIMO applications [6]. Otherwise, the mmWave massive MIMO may become either prohibitively expensive and difficult to implement (digital beamforming) or susceptible to beamforming errors that cause users to interfere with one another (analog beamforming). Table 1.1 provides a comparison of beamforming techniques.

There are two main types of hybrid beamforming: fully connected and sub-connected, shown in Fig. 1.3. Each RF chain is connected to all antennas in a fully connected architecture, and each RF chain is connected only to a set of antennas in a sub-connected architecture. The number of signal paths is $N_t \times N_{RF}^2$ (where $N_t$ and $N_{RF}$ are the number of transit antennas and RF chains, respectively) in the fully connected architecture and $N_t \times N_{RF}$ in the sub-connected architecture. The higher the number of signal paths, the higher the complexity of implementation (both hardware and signal processing) and beamforming gain [6,10,11]. Regarding spectral efficiency performance for any combination of transmitting and receiving antennas, regardless of digital or analog signal processing techniques, a fully connected structure always outperforms any other hybrid beamforming architecture. The spectral efficiency of a fully connected structure is about $N_{RF} \log_2 N_{RF}$ b/s/Hz higher than that of a sub-connected structure. However, the fully connected consumes $N_{RF}$ times more power than the sub-connected [6].

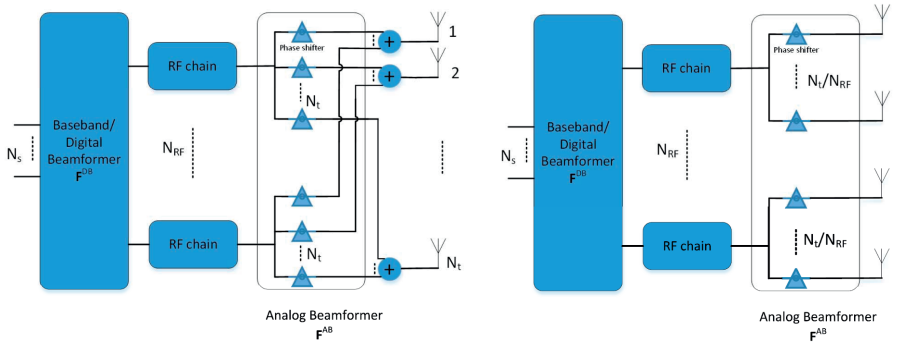


**(a)** Fully connected **(b)** Sub-connected

Figure 1.3: Major types of hybrid beamforming [6].

### 1.2.1 State of the Art

The state-of-the-art mmWave phased array technology has significantly advanced in recent years, revolutionizing wireless communication systems. Phased array systems play a crucial role in harnessing the potential of mmWave by enabling beamforming and beam-steering capabilities. One key area of advancement in mmWave phased array technology is antenna design. The physical size and wavelength constraints have limited the number of solutions based on traditional antenna designs, but recent developments have led to the creation of compact, integrated antenna arrays. These arrays consist of numerous densely packed individual antenna elements, often implemented using microstrip patch or slot antennas [12].

The stacked-patch antenna [13, 14], patch antenna [15, 16], dipole [17], dielectric resonator array [18], gapwaveguide [19,20], and horn [21] are commonly used antenna elements in 5G mmWave phased arrays. Each antenna element type offers advantages and characteristics, such as compact size, ease of integration, high gain, and precise beam control. The choice of antenna element depends on specific system requirements, desired performance, and the trade-offs between size, cost, and complexity.

Furthermore, advancements in semiconductor technology have played a vital role in the development of mmWave phased array systems. State-of-the-art beamforming chipsets for 28 GHz mmWave applications leverage mainly three semiconductor technologies, CMOS (Complementary Metal Oxide Semiconductor), SiGe (Silicon Germanium) BiCMOS, and GaN (Gallium Nitride). Each technology offers unique cost, power consumption, noise performance, linearity, and power handling advantages that cater to different aspects of beamforming system requirements [22]. The choice of technology depends on specific system requirements, such as power levels, efficiency, and integration capabilities, to deliver efficient and high-performance mmWave beamforming solutions.

CMOS-based beamforming chipsets are highly popular due to their cost-effectiveness, low power consumption, and compatibility with mainstream semiconductor manufacturing processes. Advanced CMOS technologies enable the integration of RF front-end components with digital baseband processing on a single chip. This integration facilitates compact and power-efficient beamforming systems suitable for 28 GHz mmWave applications [23, 24]. However, CMOS suffers from limitations in terms of power handling and limited output power capability, which can be a disadvantage in applications that require high transmit power levels. Additionally, CMOS may exhibit higher losses and reduced efficiency at mmWave frequencies,

SiGe BiCMOS technology is widely used for mmWave beamforming chipsets due to its high-frequency performance and low noise characteristics. SiGe processes provide excellent linearity and power-handling capabilities, making them well-suited for high-frequency communication systems. SiGe-based chipsets can deliver low-noise amplification, high-gain power amplification, and efficient phase shifting, enabling precise beamforming at 28 GHz [25,26]. However, SiGe BiCMOS also has limitations at mmWave frequencies. The high-frequency performance of SiGe BiCMOS devices may be restricted due to parasitic effects, limited gain, and reduced power handling capabilities compared to specialized high-frequency technologies like GaN.

GaN technology is emerging as a promising option for high-power and high-efficiency mmWave beamforming chipsets. GaN offers superior power handling, high breakdown voltage, and low parasitic effects. GaN-based chipsets can deliver high-power amplification with high efficiency, enabling longer-range communication. GaN power amplifiers, combined with other analog and digital processing semiconductors technologies, offer significant advantages in achieving efficient beamforming at 28 GHz mmWave frequencies [27]. However, GaN technology has some disadvantages as well. GaN devices are typically more expensive compared to CMOS or SiGe BiCMOS. Additionally, GaN devices may have higher power consumption compared to CMOS, which can be a concern in power-constrained applications.

The integrated phased arrays, which make use of a silicon base to combine the transmit and/or receiving beamforming circuitry and signal processing units, provide increased antenna gain and electrically steered beams. They are a feasible solution for implementing hybrid beamforming architectures. The first implementation of the silicon-based fully integrated phased array antenna was presented in [28] and [29]. It inspired the research on developing mmWave phased arrays based on silicon [22].

Planar arrays with similar topologies are currently being developed for mmWave 5G applications. These phased arrays can be employed in implementing sub-connected hybrid beamforming architectures. The topology of the phased array proposed in [13] is shown in Fig. 1.4. It includes up/down conversion blocks to RF/IF frequencies, a network of power dividers/combiners, beamformer chipsets, and antenna elements.

Beamformer chipsets are one of the most important factors that decide the

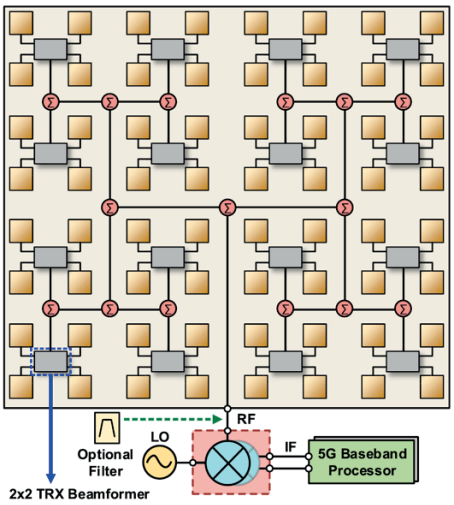


Figure 1.4: The topology of the phased array proposed in [13].

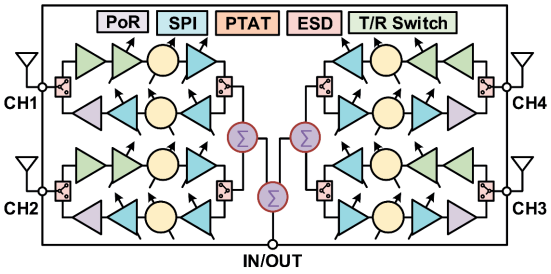


Figure 1.5: The beamformer chipset proposed in [30] and employed in the phased array in [13].

performance of the phased array. Components such as power amplifiers, low noise amplifiers, phase shifters, variable gain amplifiers, power dividers/ combiners, and transmit/receive (T/R) switches are integrated into a beamformer chipset, as shown in Fig. 1.5. The power amplifier and low noise amplifier are crucial to satisfy the power requirement of a link. Phase shifters and variable gain amplifiers are used to set the phase and amplitude of the antenna elements during analog beamforming.

The performance of the state-of-the-art integrated phased arrays is summarized in Table 1.2. Among the parameters listed in Table 1.2, three important aspects to highlight are the semiconductor technology, the antenna technology, and the EIRP. EIRP is a metric used to quantify the power radiated by an antenna system in a specific direction relative to an isotropic radiator. It takes into account both the antenna gain and the output power of the system. The integrated phased arrays are commonly implemented using CMOS and

SiGe technologies. CMOS-based phased arrays often exhibit lower EIRP than SiGe-based arrays. The antenna technologies, including stacked patch antennas, patch antennas, printed dipoles, and gapwaveguides, play significant roles in developing phased arrays. They contribute to developing phased arrays by enabling compact designs, wide bandwidths, efficient power distribution, beamforming capabilities, and integration with semiconductor chipsets.

Table 1.2: Comparison of the state-of-art 28 GHz phased arrays [22]

| | [14] | [31] | [26, 32] | [33] | [17] | [19, 20] |
|---|---|---|---|---|---|---|
| **Frequency [GHz]** | $28-32$ | $28^*$ | $27.2-28.8$ | $24-29.5$ | $26.5-29.5$ | $26.5-29.5$ |
| **Chipset technology** | SiGe BiCMOS | CMOS | SiGe BiCMOS | SiGe BiCMOS | CMOS | SiGe BiCMOS |
| **Channel per chip** | 8TRX | 8TRX | 16TRX | 4TRX | 4TRX | 4TRX |
| **Phase range/ step/ RMS error [°]** | 360 / 5.6 / N/A | 360 / 11.25 / 0.4 | 360 / 4.9 / 1.5 | 360 / 5.6 / N/A | 360 / 11.25 / 0.3 | 360 / N/A / N/A |
| **Gain range/ step/ RMS error [dB]** | 20 / N/A / N/A | 20 / N/A / 0.2 | 8 / N/A / N/A | 27 / N/A / N/A | 10 / 0.1 / 0.04 | N/A / N/A / N/A |
| **TX OP1dB [dBm]** | 11-12 | 11.3 | 13.5 | 11.5-12 | 15.7 | 17 @ Psat |
| **Antenna technology** | Stacked patch | Patch | Stacked patch | Stacked patch | Printed dipole | Gapwaveguide |
| **Polarization** | Dual | Dual | Dual | Single | Single | Single |
| **Array size** | $8\times8$ | $2\times16$ | $8\times8$ | $16\times16$ | $1\times8$ | $2\times8$ |
| **E-/H-plane scan [°]** | $\pm50/\pm25$ | $\pm50/-$ | $\pm50/\pm50$ | $\pm60/\pm50$ | $\pm50/-$ | $\pm45/\pm10$ |
| **EIRP @ OP1dB [dBm]** | 51 | 45.6 @ Psat | 54 | 63.5 | 36.5 | 51 @ Psat |

$^*$ Narrow bandwidth antenna design at 28 GHz center frequency.

### 1.2.2 Challenges at mmWave

Designing phased arrays at mmWave frequencies poses several unique challenges that must be overcome to ensure optimal performance. Some of the key challenges include:

1. Propagation Path Loss: At mmWave frequencies, the propagation path loss experienced by the signal is significantly higher than in lower frequency bands. This increased path loss limits the coverage range and requires highly directional beams to compensate for the signal attenuation. Designing phased arrays that achieve high gain and precise beamforming becomes crucial to overcome propagation challenges.

2. Antenna Elements: The size of individual antenna elements becomes extremely small at mmWave frequencies due to the reduced wavelength. This presents challenges in maintaining a sufficient number of elements within the available physical space to achieve the desired gain and beamforming capabilities. Integration techniques and miniaturization methods are essential to pack many antenna elements into an array while achieving the metrics such as large bandwidth, good matching, and high efficiency.

3. Mutual Coupling: The closely spaced antenna elements in a phased array can lead to mutual coupling effects between antenna elements, where the radiation and currents from one element affect the performance (matching and radiation characteristics) of neighboring elements. At mmWave frequencies, the spacing between the elements is comparable to the wavelength, exacerbating these coupling effects. Designing techniques to minimize mutual coupling and optimize the array performance is a significant challenge.

4. RF active components: RF active components such as power amplifiers, low noise amplifiers, phase shifters, mixers, etc. pose challenges such as bandwidth, linearity, efficiency, saturation, noise figure, integration, and packaging to the design of the mmWave phased arrays. Linearity is important to minimize signal distortion and maintain signal quality. Efficiency and saturation power are extremely important to set the system's efficiency and power capability. On the other hand, the noise figure is important for low-noise amplifiers to determine the wireless system's sensitivity and signal-to-noise ratio.

5. Front-end routing and transitions: Front-end transitions and routing play a crucial role in mmWave systems as they are responsible for establishing an efficient connection, in terms of loss and coupling, between active components (such as amplifiers) and antenna elements. These transitions are essential to ensure proper signal transfer with minimal losses, maintain structure robustness and contribute to cost-effective manufacturing.

6. Power Consumption: The power consumption of mmWave phased arrays can be challenging due to the large number of active components in the system, such as amplifiers and phase shifters. Power amplifiers, in particular, need to provide sufficient output power while maintaining efficiency. Developing power-efficient components and circuitry is crucial to minimize power consumption and extend the battery life of wireless devices.

7. Beamforming Algorithms and Calibration: Advanced beamforming algo-

rithms are necessary to optimize the performance of mmWave phased arrays. However, these algorithms need to account for the increased complexity and the challenges the higher frequencies pose. Additionally, calibrating the phased array to account for manufacturing variations, mutual coupling effects, and environmental changes becomes more intricate at mmWave frequencies.

8. Cost and Manufacturing: The design and manufacturing processes for mmWave phased arrays can be more complex and expensive compared to lower frequency bands. Advanced fabrication techniques, specialized materials, and precise alignment and testing procedures increase costs. Ensuring cost-effective and scalable manufacturing methods is a significant challenge for the widespread adoption of mmWave phased array technology.

Addressing these challenges requires interdisciplinary research and development efforts spanning antenna design, RF circuitry, signal processing, and system integration. By overcoming these hurdles, mmWave phased arrays can unlock the full potential of high-frequency bands, enabling high-speed, high-capacity wireless communication systems and applications.

This thesis focuses on the low-loss wide-band antenna element design used in phased arrays with high EIRP. State-of-the-art phased arrays at 28 GHz use substrate-based antenna elements, as shown in Table 1.2. Antennas are typically integrated with other circuitry, such as mixers, feeding networks, and beamforming networks, e.g., beamformer integrated circuits (BFIC). Multiple layers of printed circuit boards (PCB) are required for BFICs to deliver the DC power and the control signals. When substrate-based antennas are combined with a PCB, the number of PCB layers rapidly increases, and therefore the losses too. This increase may also be necessary to increase antenna bandwidth [34, 35], or to accommodate the routing from the BFIC to the antenna port [23]. However, a high number of layers usually results in high complexity and, therefore in high costs of the PCB design. On the other hand, the waveguide-based planar antennas show better loss characteristics at mmWave frequencies. Gapwaveguide technology can be used to reduce the complexity of the PCB design while supporting a large bandwidth and minimizing feeding losses. It has been used widely to design high gain and low loss slot array antennas at mmWaves [36–38]. This technology has been proposed as a good candidate for providing a fair trade-off between manufacturing cost and manufacturing flexibility of electromagnetic components [19, 39].

Other focus areas of this thesis include the integration of RF active components with the antenna elements, designing the transition from gapwaveguide to microstrip, and making use of power amplifiers with high power, power handling, calibration, and cost-efficiency.

## 1.3 Gapwaveguide Technology

Gapwaveguide is an emerging technology that has gained significant attention in the realm of microwave and millimeter-wave systems. It offers a novel approach to wave propagation, eliminating the need for a conventional dielectric

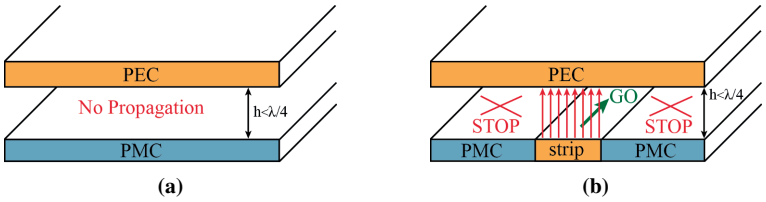


Figure 1.6: Basic principle operation of gapwaveguide [3]. (a) PEC-PMC parallel-plate electromagnetic cut-off. (b) TEM local wave propagation.

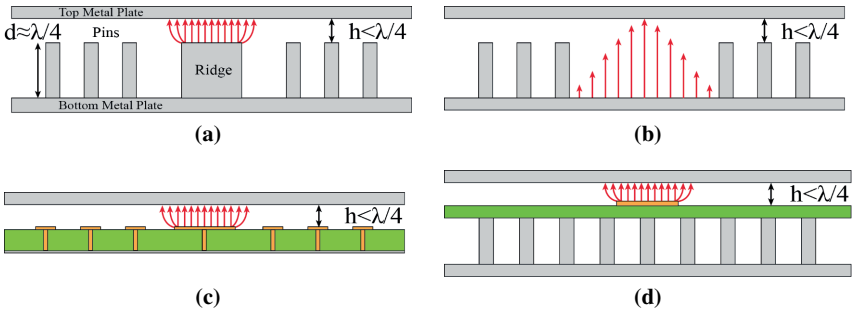


Figure 1.7: Different gapwaveguide geometries and desired propagation modes [3]. (a) Ridge gapwaveguide. (b) Groove gapwaveguide. (c) Microstrip gapwaveguide. (d) Inverted-microstrip gapwaveguide.

substrate [39]. It can be described as a novel wave-guiding mechanism wherein the direction of power flow is controlled by a periodic electromagnetic band gap (EBG) geometry surrounding a guiding structure, such as a strip, ridge, or groove [3]. The notable advantages of gapwaveguides lie in their low-loss characteristics, flexible planar manufacturing, high power handling, and cost-efficiency, especially at mmWave frequencies [40]. The absence of a dielectric substrate significantly reduces signal attenuation, enhancing transmission efficiency. This attribute is particularly advantageous in high-frequency applications, where signal losses can harm overall system performance.

The basic principle of gapwaveguide is shown in Fig. 1.6. In a perfect electric conductor (PEC)-perfect magnetic conductor (PMC) parallel plate structure with less than a quarter-wavelength spacing, no wave can propagate, as shown in Fig. 1.6(a). Introducing a PEC surface in the PMC plate makes it possible to achieve a waveguide structure, as depicted in Fig. 1.6(b). Based on this idea, several configurations of gapwaveguides have been introduced so far (Fig. 1.7).

Furthermore, gapwaveguides exhibit exceptional wide bandwidth capabilities. The inherent structure enables the efficient propagation of electromagnetic waves across a broad frequency range. This wide bandwidth characteristic renders them suitable for applications requiring operation over a considerable fre-

quency spectrum, such as millimeter-wave communication systems. Additionally, the absence of a dielectric substrate in the ridge and groove gapwaveguides simplifies manufacturing and reduces fabrication costs.

Gapwaveguide technology has applications in various fields, including phased array antennas, radar systems, wireless communication, automotive radar, and millimeter-wave imaging. Multiple microwave and millimeter components, such as slot arrays, filters, and diplexers, have been designed and developed during the past decade [J]. Gapwaveguide has shown a competitive performance compared to traditional transmission lines in these fields.

## 1.4 Thesis Motivation and Contribution

This thesis focuses on designing and analyzing advanced phased array systems based on gapwaveguide technology for mmWave 5G applications. The primary objective is to address key challenges in wireless communication systems, including achieving high EIRP, wide-angle beam scanning over a large bandwidth, compact form factor, cost-effectiveness, and reliable performance in indoor environments.

The first significant contribution of this thesis is the design and development of a large phased array system based on gapwaveguide technology. This design focuses on achieving a high EIRP while incorporating a new, compact, low-loss antenna element design. Notably, the implementation of this design is based on a simple printed circuit board (PCB) layout, offering cost-effectiveness and ease of manufacturing.

Furthermore, this phased array system incorporates a 45-degree slanted polarization. This specific polarization orientation enhances signal propagation and reception characteristics, improving the system's performance. By leveraging the advantages of gapwaveguide technology, the large array configuration achieves high-gain and highly directional beams with the desired 45-degree slanted polarization. This innovative combination of gapwaveguide technology, a compact low-loss antenna element design, and the specific polarization orientation establishes a novel approach in phased array antenna design.

The second significant contribution of this thesis is the development of a high-power, compact, and cost-effective phased array system employing GaN front-ends by leveraging the advantages of gapwaveguide and GaN technologies. One key aspect addressed in this design is the efficient management of the substantial heat generated by the GaN front-ends. The integration of gapwaveguides plays a crucial role in handling and dissipating the large amount of heat produced by the GaN front-ends. The gapwaveguide structure effectively helps to channel and dissipate the heat generated by the GaN front-ends, mitigating thermal issues and improving overall system reliability. This design ensures reliable performance and optimal power handling capabilities by utilizing the unique properties of gapwaveguide technology, such as reduced losses and efficient heat dissipation.

Additionally, this design emphasizes the compactness and cost-effectiveness of the phased array system. The integration of GaN front-ends and the utilization of gapwaveguide technology enable a high EIRP while maintaining a compact form factor. This combination facilitates the creation of a cost-effective phased array system.

The third major contribution of this thesis involves the down-link performance analysis of these designed phased arrays in indoor environments. Indeed, indoor wireless communication scenarios pose unique challenges due to signal propagation characteristics, interference, blockage, and multipath effects. The performance analysis evaluates key metrics such as active power consumption, signal quality, interference mitigation, signal-to-interference plus noise ratio (SINR), and achievable sum rate capacity. By conducting a thorough performance analysis, valuable insights can be gained regarding the suitability and effectiveness of the designed phased array systems in indoor environments.

This thesis addresses crucial aspects of phased array systems using gapwaveguide technology. The designs focus on achieving high EIRP, compactness, cost-effectiveness, and robust performance in indoor environments. The findings and analysis from this research will contribute to the advancement of wireless communication systems, particularly in areas such as high-gain antenna design, power efficiency, and improved indoor connectivity.

## 1.5 Thesis Outline

This thesis is organized into six chapters. Chapter two presents the design of passive components, such as transitions and antenna elements based on gapwaveguide, as the building blocks of the phased array antennas at 28 GHz. Chapter three provides the design methodology, fabrication, and evaluation of a gapwaveguide-based high-EIRP large phased array antenna at 28 GHz. The design and experimental verification of a cost-efficient, high EIRP (60 dBm), large-bandwidth (26.5–29.5 GHz) active phased array antenna system is presented in Chapter four. Chapter five analyses the performance of mmWave 5G analog beamforming phased array antennas in indoor environments. Finally, Chapter six outlines the concluding remarks and highlights some directions for further research.

# Chapter 2

# Gapwaveguide-based Passive Component Design at 28 GHz

## 2.1 Introduction

The rapid advancement of wireless communication technologies, particularly in the mmWave frequency range, has driven the need for efficient and reliable passive components to support high-performance systems. In this chapter, the focus is on the design and integration of passive components based on gapwaveguide technology at 28 GHz to be employed in phased array designs. The design of passive components plays a critical role in ensuring seamless integration within the overall system architecture. Specifically, this chapter investigates the design aspects of pin and ridge structures for the gapwaveguide line, microstrip to gapwaveguide transitions and antenna elements based on the gapwaveguide. Additionally, the integration of these transitions with the antenna elements is explored.

The first part of this chapter focuses on the design of pin and ridge structures for the gapwaveguide line. The dimensions and characteristics of these structures are carefully determined to achieve the desired quasi-TEM mode in the line over the desired frequency band of $26.5 - 29.5$ GHz. Next, the design of microstrip to gapwaveguide transitions is discussed. These transitions are essential for signal transfer between different transmission line technologies, enabling the integration of gapwaveguide-based components with other circuitry. The design considerations, such as impedance matching, insertion loss, and coupling, are thoroughly investigated to ensure maximum power transfer.

Furthermore, the chapter delves into the design of antenna elements based on gapwaveguide technology. These elements are crucial for efficient radiation and reception of signals in mmWave systems. The characteristics of the antenna elements, such as their geometry, matching, mutual coupling, and

This chapter is a reprint material as it appears in [A], [B], [C] and [D]. The dissertation author was the primary investigator and author of these papers.

Table 2.1: Pin and ridge gapwaveguide structure key dimensions expressed in $\lambda_0$ at 28 GHz.

| *Parameter* | *Value* | *Parameter* | *Value* | *Parameter* | *Value* |
|---|---|---|---|---|---|
| $a$ | 0.13 | $g$ | 0.005 | $h_r$ | 0.11 |
| $p$ | 0.28 | $w$ | 0.52 | $w_r$ | 0.13 |
| $h$ | 0.17 | | | | |

radiation patterns, are presented. Lastly, the integration of transitions with antenna elements is explored. Through a comprehensive investigation and design process, this chapter aims to provide valuable insights into the design of passive components based on gapwaveguide technology for 28 GHz mmWave phased array applications.

## 2.2 Pin and Ridge Gapwaveguide Design

To allow for the propagation of the quasi-TEM (QTEM) mode in the gapwaveguide transmission lines and at the same time to suppress undesirable modes to minimize leakage, it is vital to ensure that pins on both sides of the transmission line exhibit a PEC/PMC stopband for parallel-plate modes. Periodic pin structure acts as a high impedance surface with an air gap lower than $\lambda/4$. The dispersion diagram of the pin in a unitcell structure is the most important figure to show the stopband [3].

Therefore, the stopband of the pins, which is designed by following the design rules in [39, 41], should coincide with the desired operational bandwidth of 26.5−29.5 GHz. The pin, shown in the inset of Fig. 2.1(a), has been simulated assuming infinite periodic boundary conditions. Pins and other metal parts of the antenna element are simulated and fabricated with aluminum, with an electrical conductivity of $3.56 \times 10^7$ S/m. The corresponding pin dimensions are given in Table 2.1. The simulation procedure is similar to the one discussed in [41]. The corresponding dispersion diagrams of the first two modes are shown in Fig. 2.1(a), with a stopband from $15 - 60.5$ GHz. The wave propagation can be controlled in the desired direction by introducing a ridge between the pin structures. As illustrated in Fig. 2.1(b), a single mode band from $21 - 53$ GHz can be generated using only one pin at each side of the ridge (shown in the inset of Fig. 2.1(b)) with parameters shown in Table 2.1. Infinite periodic boundary conditions obtain the results, while a propagating mode exists only in the $y$-direction within the phased array's operating bandwidth. This QTEM mode is utilized to excite the slots.

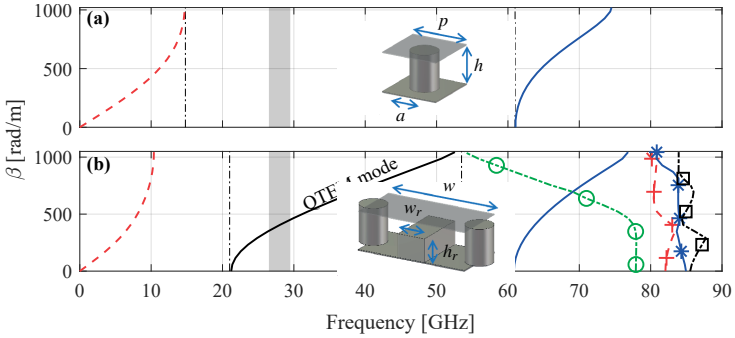


Figure 2.1: Dispersion diagrams for infinite periodic (a) pins and (b) ridges embedded within a pin texture including all the modes. The target bandwidth is highlighted in gray.

## 2.3 Top PCB Transition

All microwave technologies must offer good integration with PCB technology as the carrier of most, if not all, active components. It is thus important that such transitions offer good performance, robustness, and simple integration. This is especially true in phased arrays for 5G applications, where a large number of densely packed antenna elements create issues of spacing and isolation [42, 43]. The three types of transitions presented in this section target specifically this scenario and have thus been tested in an array configuration similar to previously published arrays [20], [C].

In the past years, many microstrip-to-gapwaveguide transitions have been designed. A horizontal contactless transition is presented in [44], but the one wavelength width makes it unsuitable for phased arrays. This issue is solved in [45] with a horizontal, compact, and contactless transition. However, vertical transitions are the only practical solution for phased arrays as they leave the space below the antenna available for PCB routing and active components. Ultra-wideband transitions have also been proposed in [46,47], but the need for galvanic contact between waveguide and microstrip makes them sensitive to assembly [48]. Double- and single-ridge gapwaveguides allow the designing of narrow waveguide-based radiating elements to be used in phased arrays with wide steering ranges. The proposed transitions can be used for gapwaveguide-based arrays, which have been investigated to be promising solutions for upcoming 5G applications [49]. In this section, three types of contactless vertical transitions with application in antenna arrays based on gapwaveguide technology are proposed.

The structure of the transitions is shown in Fig. 2.2. All three transitions consist of a PCB with a rectangular patch coupled to a double-ridge waveguide surrounded by a pin structure. The double-ridge waveguide has dimensions $4.25 \times 2.1$ mm with a ridge height of 1.4125 mm and a ridge width of 1.4 mm.

The double-ridge is extended towards the PCB on each side of the waveguide opening to ensure sufficient coupling between the transition patch and the waveguide. The pin structure is designed to have a stopband in the desired frequency range to increase isolation between adjacent antenna columns, decrease leakage from the microstrip patch, and consequently improve signal transmission level to double-ridge waveguide. The role of pin structure is very essential, and the transitions do not work without them. The pin dimensions are $2.7 \times 1.58$ mm with a pin period of 2.8 mm. A 10 mils Rogers RO4350B-substrate with a relative dielectric constant of $\varepsilon_r = 3.66$ is used for the PCB, with a copper thickness of 0.035 mm and a microstrip width of 0.5 mm. The specific transition type configuration is explained below:

- Type 1 transition has a matching stub in series with the transition patch as shown in Fig. 2.2a. Both the size of the stub and the distance from the patch is tuned to achieve optimal performance. The patch and stub dimensions are $2.42 \times 2.6$ and $2 \times 2.73$ mm$^2$, respectively, and have 1.7 mm distance.

- Type 2 transition is shown in Fig. 2.2b. It uses an inset of the feed into the patch. This gives a more compact design compared to the type 1 transition. Patch dimensions are $2.54 \times 2.73$ mm$^2$, and inset gap and length are 0.42 and 0.24 mm, respectively.

- Fig. 2.2c shows type 3 transition. It uses a quarter-wave transformer to transform the impedance of the microstrip to that of the transition patch. The patch and transformer dimensions are $2.6 \times 2.68$ and $0.43 \times 2.44$ mm$^2$.

The transition patch is optimized individually for each transition type regarding its length, width, and center point offset relative to the center point of the waveguide.

The software Computer Simulation Technology (CST) was used for simulating and optimizing the three transition types. The scattering parameters of each transition are shown in Fig. 2.3a- 2.3c, where the port numbering corresponds to Fig. 2.2. For transition type 1, the scattering parameters in Fig. 2.3a show a wideband performance with a 15 dB return loss bandwidth of 21.3% while having an insertion loss of maximum 0.62 dB within the band of interest. The coupling to the adjacent transition columns is kept below $-15$ dB throughout the simulation range and is less than 20 dB for $26.5 - 29.5$ GHz. The scattering parameters for transition type 2 are shown in Fig. 2.3b displaying a 15 dB return loss bandwidth of 13.3% and isolation towards neighboring columns higher than 17 dB between $26.5 - 29.5$ GHz. The maximum insertion loss within the frequency band is 0.6 dB for transition type 2. For type 3, the results are displayed in Fig. 2.3c and show a 15 dB return loss bandwidth of 16.8% with a maximum insertion loss of 0.49 dB.

A summary of the performance of all three transition types is given in Table 2.2, where advantages and disadvantages are also listed. Comparing the results shows that transition type 1 gives a wideband performance while

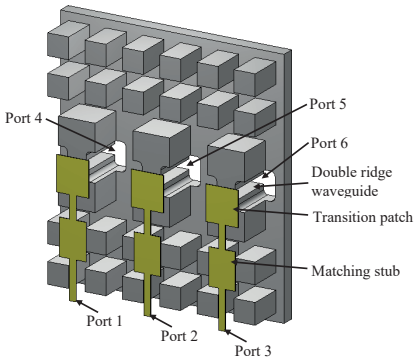


(a) Type 1

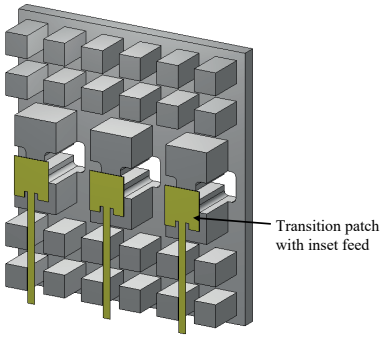


(b) Type 2

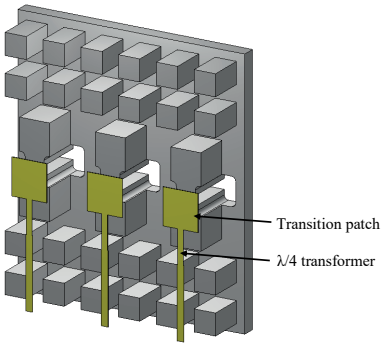


(c) Type 3

Figure 2.2: The structure of three microstrips to double ridge waveguide transitions. In these figures, the substrate and ground layer of microstrip lines are not shown.

Table 2.2: Comparison of transitions performances.

| Transition | Bandwidth [GHz] | | Max. insertion loss [dB] in 26.5 – 29.5 GHz | Advantage | Disadvantage |
|---|---|---|---|---|---|
| | $\lvert S_{22}\rvert < -15$ dB | $\lvert S_{22}\rvert < -10$ dB | | | |
| Type 1 | 6 (21.3%) | 6.8 (24%) | 0.62 | Wideband | Not Compact |
| Type 2 | 3.7 (13.3%) | 5.4 (19.2%) | 0.6 | Compact on PCB | Narrowband |
| Type 3 | 4.6 (16.8%) | 5.8 (21.2%) | 0.49 | Relatively wideband | - |

being less compact than other solutions. Type 2 is the most compact of the transitions but has the disadvantage of being less wideband compared to types 1 and 3.

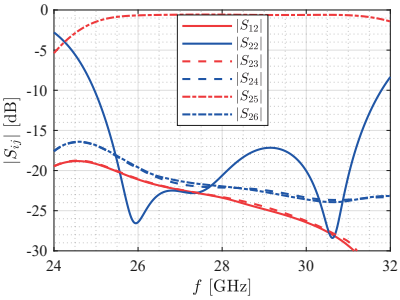


(a) Type 1

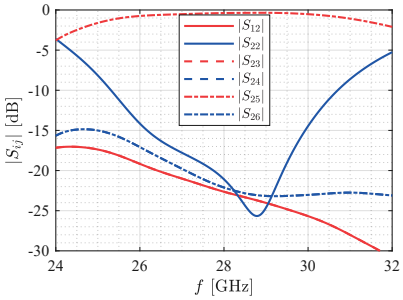


(b) Type 2

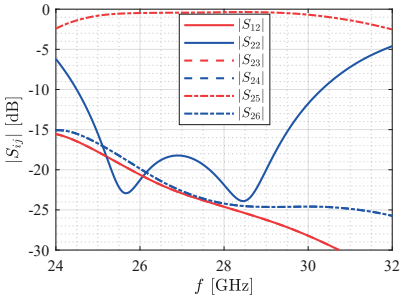


(c) Type 3

Figure 2.3: Scattering parameters of each transition.

## 2.4 Through PCB Transition

A wideband vertical microstrip-probe transition with a backshort cavity is designed, following the principles outlined in [50, 51]. Such transition allows the components facing backward to contact the shield layer directly. The layout of the microstrip probe is shown in Fig. 2.4(a). A rectangular via fence surrounds the probe, allowing for a strong coupling to the gapwaveguide through multiple layers of PCB. The PCB stack-up used for the transition design has 5 layers of substrates (consisting of RO4350B with $\epsilon_r = 3.66$, $\tan\delta = 0.0037$, and thickness = 168 µm as core substrates, and RO4450F with $\epsilon_r = 3.7$, $\tan\delta = 0.004$, and thickness = 102 µm as prepreg substrates), which is typically employed in the design of mmWave phased arrays. The stack-up includes 6 layers of copper with electrical conductivity of $5.96 \times 10^7$ S/m. As shown in Fig. 2.4(b), the backshort cavity comprises cylindrical pins positioned over the probe. The corresponding transition dimensions are given in Table 2.3. The backshort pins are simulated in a unit cell configuration and show a stopband from $25 - 57$ GHz. Four pins on the sides will be shared with neighbor subarray transitions, and overall, 10 pins are used to build a backshort. Fig. 2.5 shows that the transition feeding two ridge gapwaveguides and the transition ports are marked. The

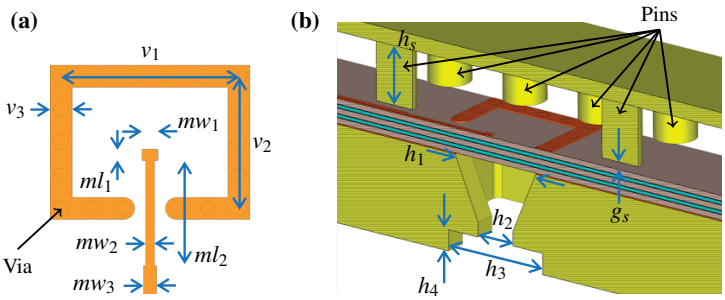


Figure 2.4: Microstrip to double ridge gapwaveguide transition model; (a) layout of microstrip probe, and (b) three-dimensional view of transition at a cross-section which is vertical to the middle of microstrip probe.

Table 2.3: Transition structure key dimensions expressed in $\lambda_0$ at 28 GHz.

| *Parameter* | *Value* | *Parameter* | *Value* | *Parameter* | *Value* |
|---|---|---|---|---|---|
| $mw_1$ | 0.04 | $v_1$ | 0.45 | $h_1$ | 0.28 |
| $mw_2$ | 0.02 | $v_2$ | 0.34 | $h_2$ | 0.12 |
| $mw_3$ | 0.03 | $v_3$ | 0.06 | $h_3$ | 0.33 |
| $ml_1$ | 0.12 | $h_s$ | 0.18 | $h_4$ | 0.06 |
| $ml_2$ | 0.27 | $g_s$ | 0.02 | | |

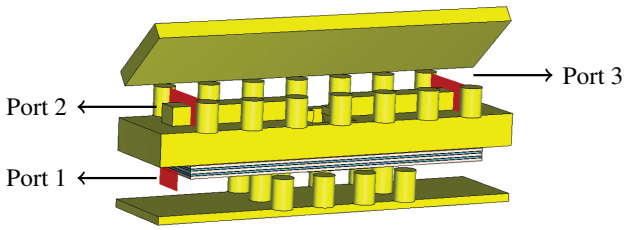


Figure 2.5: The ports locations of the through PCB transition.

simulation results of the transition are depicted in Fig. 2.6.

## 2.5 Horizontally Polarized Antenna Element

This section presents a slot array antenna based on the gapwaveguide technology for 5G applications in mmWaves. The array element comprising 8 slots is shown in Fig. 2.7a and the corresponding structure of the horizontal linear array antenna consisting of 8 vertical elements is shown in Fig. 2.7b. As can be seen from Fig. 2.7a, each element is fed at the center with a double ridge waveguide and with two ridges exciting the 8 radiating longitudinal (along the

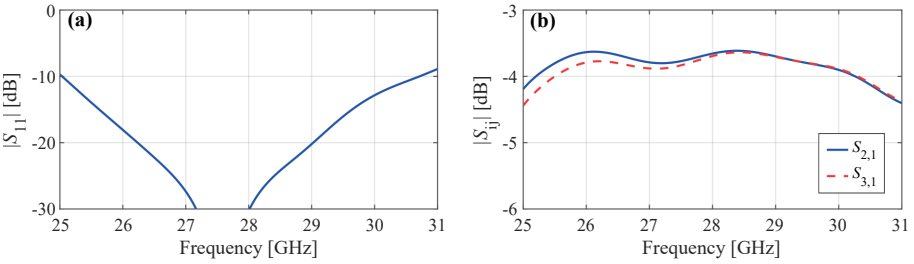


Figure 2.6: (a) Reflection coefficient, and (b) transmission coefficients of the through PCB transition.

$y$-axis) slots. The elements are separated from each other with a row of pins. The pins are designed to stop any leakage between the array elements, and their stop-band covers the operational frequency bandwidth of the antenna. The slots are non-periodic, which provides both better matching and radiation properties. The formation of the slots provides the possibility of having the same E-plane radiation pattern as well as a similar contribution to the scanning E-plane.

The design of the antenna started with the design of the array element as a unit cell. The optimization of the radiating slots and the gapwaveguide line was set out to achieve $|S_{11}| < -10$ dB in the frequency band from 26.5 to 29.5 GHz. Each array element was designed to have minimum coupling to adjacent elements. Then, by placing other array elements and forming the complete array antenna, the final structure of the array antenna was obtained. In the next step, the active reflection coefficients of the antenna elements were optimized to be lower than $-10$ dB, while the main lobe is steered in the E-plane over the scanning angles within the $\pm 45^\circ$ interval. The spacing between the array elements is half the wavelength of the frequency at the center of the covered frequency band.

The antenna was simulated and optimized using Computer Simulation Technology (CST). Fig. 2.8 shows the active reflection coefficient of the array antenna $\Gamma_a$ when the main beam scan angles from the broadside direction to $45^\circ$. As can be seen, its value stays below $-10$ dB within the band of interest, i.e., from 26.5 to 29.5 GHz at all the scan angles of interest. The radiation pattern of the array antenna in the E-plane is shown in Fig. 2.9 for four different frequencies. The total gain of the antenna is 23 dBi computed as the average over the frequency band of operation at the broadside angle. As can be seen, the side lobe level is at least $-10$ dB lower than the main lobe level in all scan angles and frequencies. There is a grating lobe when the array steers to the $45^\circ$ scanning angle which is at its highest level at 29.5 GHz. The existence of grating lobes in array antennas can be avoided with the proper design of the array.

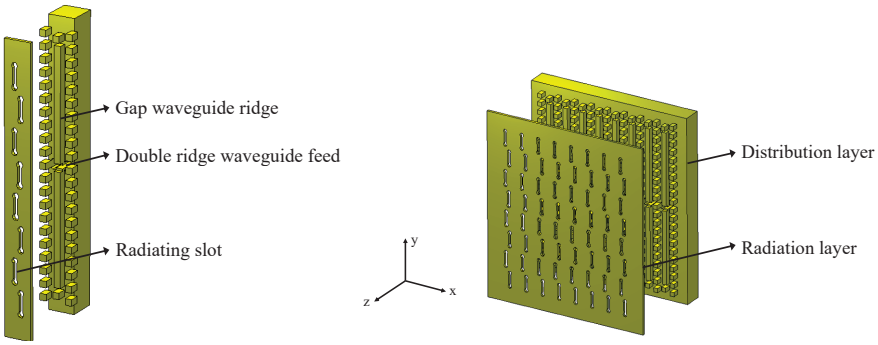


Figure 2.7: Exploded view of (a) the array element and (b) the array antenna.

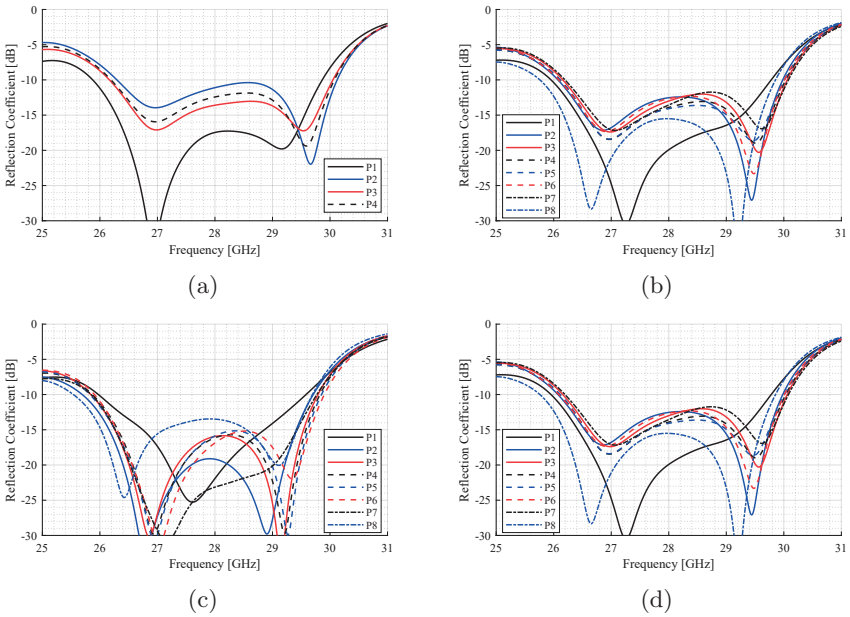


Figure 2.8: Active reflection coefficients of the 8 antenna ports as a function of frequency $f$, when the main lobe of the antenna is steered toward different scanning angles $\theta_s$, (a) 0°, (b) 15°, (c) 30° and (d) 45°.

### 2.5.1 Integration with Top PCB Transition

To further study the performance of the proposed horizontally polarized antenna, we consider the integration with previously designed top PCB transitions. Note that neither the antenna nor the transition has been tuned to each

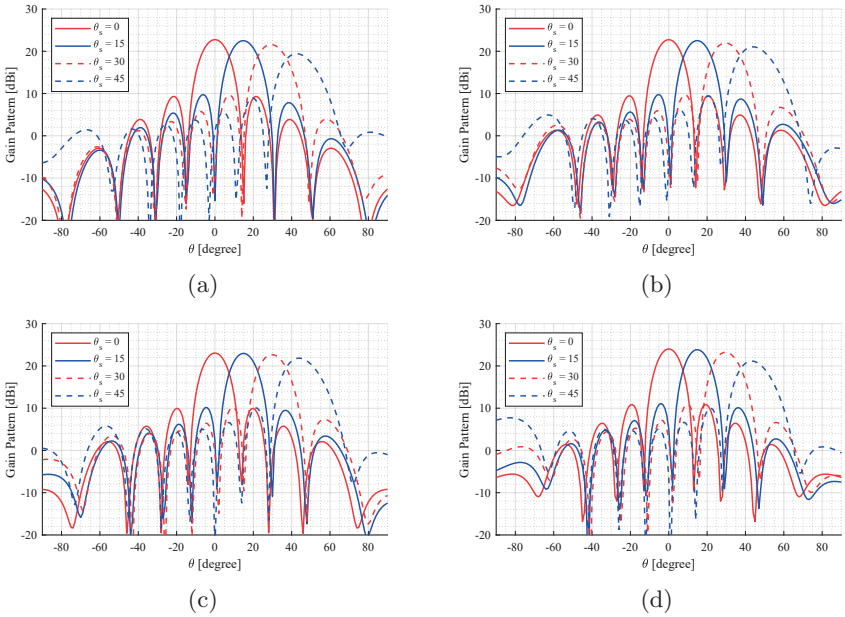


Figure 2.9: Radiation pattern of the array antenna in the E-plane for different scanning angles $\theta_s$ and different frequencies; (a) 26.5 GHz, (b) 27.5 GHZ, (c) 28.5 GHz and (d) 29.5 GHz

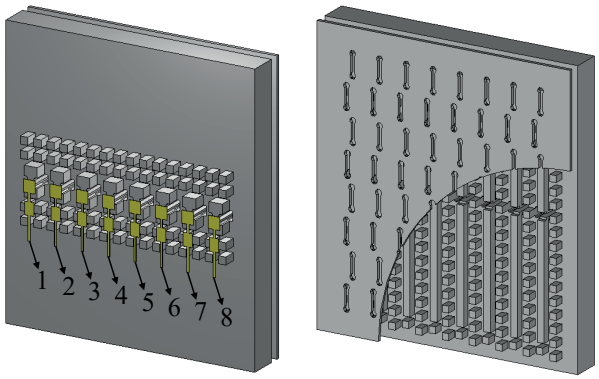


Figure 2.10: Integration of transition type 1 with a 5G antenna array based on gapwaveguide technology. A part of the slot layer is cut for viewing purposes. The number of ports for each microstrip line is shown in the left side picture.

other. Thus, sub-optimal performance is expected. The front and back views of the complete antenna and type 1 transition assembly are shown on the left and right sides of Fig. 2.10, respectively. The array comprises 8 center-fed

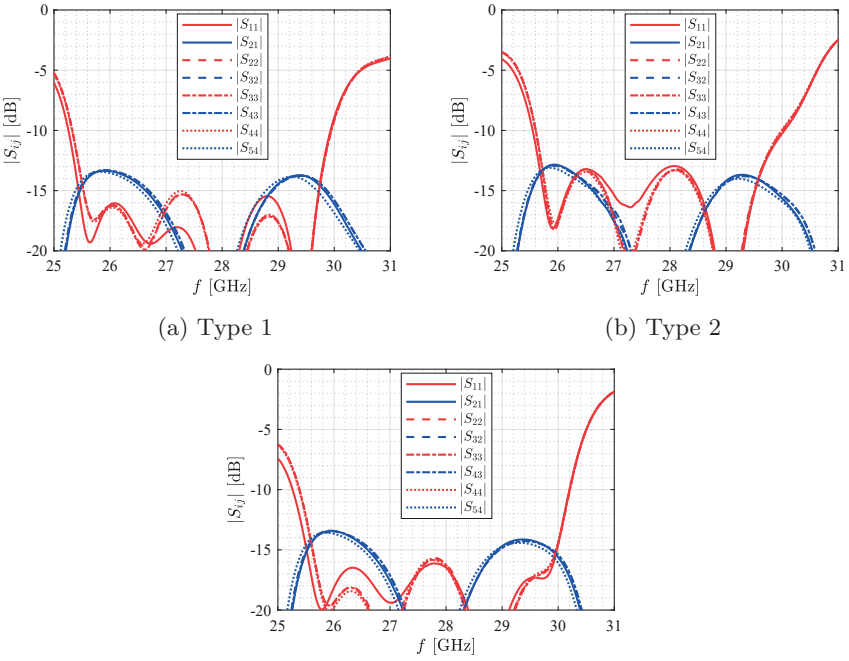


(a) Type 1

(b) Type 2

(c) Type 3

Figure 2.11: Reflection coefficient and coupling coefficients with neighbor ports in the array, when the transitions are used to excite the antenna.

subarrays of 8 longitudinal and horizontally polarized slots. The horizontal spacing between columns is 5.6 mm ($0.52\lambda_0$ at 29.5 GHz).

Fig. 2.11 shows the embedded scattering parameters of the array ports when the three types of transitions are used. Due to symmetry in the structure, simulation results for ports 5 to 8 are omitted. The antenna array integrated with every type of transition has scattering parameters below −10 dB, without retuning for the new transitions. The coupling coefficients for adjacent ports are better than −13 dB, with the non-contiguous being below −20 dB.

## 2.6 Dual 45°-slant Polarized Antenna Element

As well known, traditional technologies, such as planar transmission lines and hollow waveguides, lose their advantages at the mmWaves by incurring high losses and a complex manufacturing process, respectively [37,52,53]. Currently, research efforts have intensified to produce antenna technologies allowing for easy manufacturing, low loss, and high antenna efficiency. The gapwaveguide technology has emerged as a candidate for providing a fair trade-off between cost and manufacturing flexibility of electromagnetic components [39]. So far,

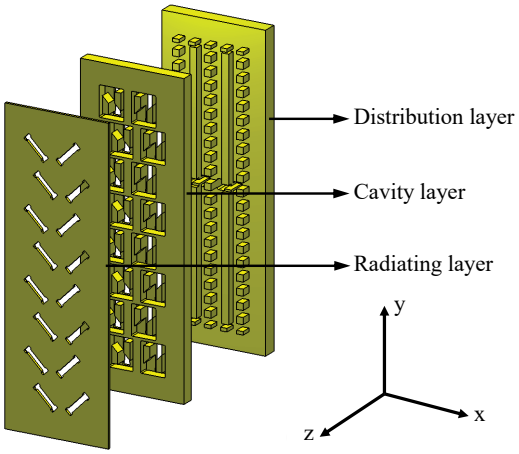


Figure 2.12: Exploded view of the antenna.

manufactured and reported antennas based on the gapwaveguide technology have mainly focused on linear polarization. The only dual-polarized antenna based on this technology is reported in [54]. It uses a circular aperture as the radiation element fed orthogonally by two cylindrical cavities. Given the resonant nature of the antenna, this leads to a limited bandwidth within $29.5-31$ GHz (5%).

Slant polarized antennas, i.e., producing $\pm 45^\circ$ linear polarization, offer lower side lobe levels compared to those with horizontal and/or vertical polarization [53]. $45^\circ$ linear polarized antennas are good candidates for collision avoidance automotive radar systems, due to minimizing interference from the radars with orthogonal polarization mounted in the cars coming from opposite direction [55, 56]. In this section, an antenna based on the gapwaveguide technology is designed to provide two orthogonal linear polarizations with similar radiation patterns for both polarizations over a wide frequency band. The frequency band of the antenna is $24.25-27.25$ GHz, which complies with the 5G mmWave frequency bands in EU [57].

The antenna consists of three layers, the distribution layer containing the ridge gapwaveguide (RGW) transmission lines, the cavity layer, and the radiating layer shown in Fig. 2.12. The distribution layer is fed from the middle (in $y$-axis direction) with two double ridge waveguides feeding two RGWs in the opposite direction. Three columns of pins are used to stop any leakage from the RGWs. The pins are designed so that their stop-band covers the operational frequency bandwidth of the antenna. The fields from the RGWs are coupled through 16 vertical slots to the cavity layer. The cavity layers slots are in two columns, and they are separated with $\lambda_g/2$ vertical distance ($y$-axis direction). The slots in each column have electric fields with the same phase, magnitude,

Table 2.4: Co-polarization and cross-polarization unit vectors for the waves generated by each port.

| Port | Co-polarization | Cross-polarization |
|---|---|---|
| P1 | $\frac{1}{\sqrt{2}}(\hat{x}+\hat{y})$ | $\frac{1}{\sqrt{2}}(\hat{x}-\hat{y})$ |
| P2 | $\frac{1}{\sqrt{2}}(\hat{x}-\hat{y})$ | $\frac{1}{\sqrt{2}}(\hat{x}+\hat{y})$ |

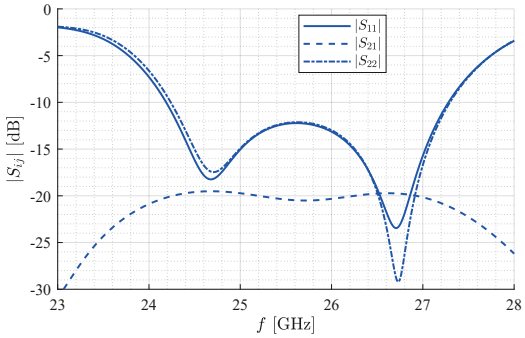


Figure 2.13: Magnitude of scattering parameters of the antenna.

and direction ($x$-axis direction).

Each column of cavities rotates electric fields in the vertical slots to create two orthogonal polarizations. There are two pins in each cavity to transform the field direction. The transformed fields excite the slots in the radiating layer. The fields in the radiating layer for each column of slots also have the same phase, magnitude, and direction and finally, they create two waves with orthogonal polarizations. The co-polarization and cross-polarization unit vectors of each port are shown in Table 2.4.

The designed antenna is simulated and optimized using the CST MWS software. Fig. 2.13 shows each port's return losses and their mutual coupling. The results show that the antenna covers the frequency band $24.25 - 27.25$ GHz (BW= 11.6%). In this band, the reflection coefficient for both ports and their mutual coupling is less than $-10$ dB and $-19$ dB, respectively. The total efficiency of the antenna is more than $-0.5$ dB for each polarization, which is depicted in Fig. 2.14. Co-polarization and cross-polarization radiation patterns of the antenna in the horizontal plane ($xz$-plane) are shown in Fig. 2.15, for three different frequencies. In the broadside direction ($\theta = 0$), each polarization has a 14.5 dBi gain with a maximum $-15$ dB cross-polarization level in the frequency band of interest.

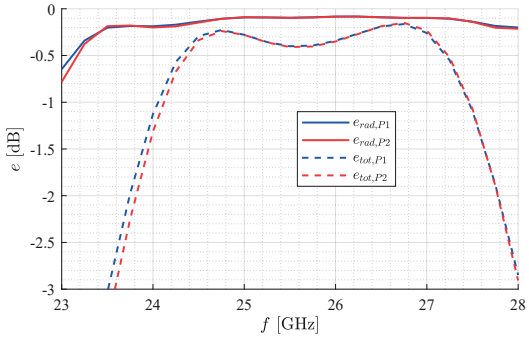


Figure 2.14: Radiation ($e_{rad,P1}$,$e_{rad,P2}$) and total ($e_{tot,P1}$,$e_{tot,P2}$) efficiencies of the antenna.

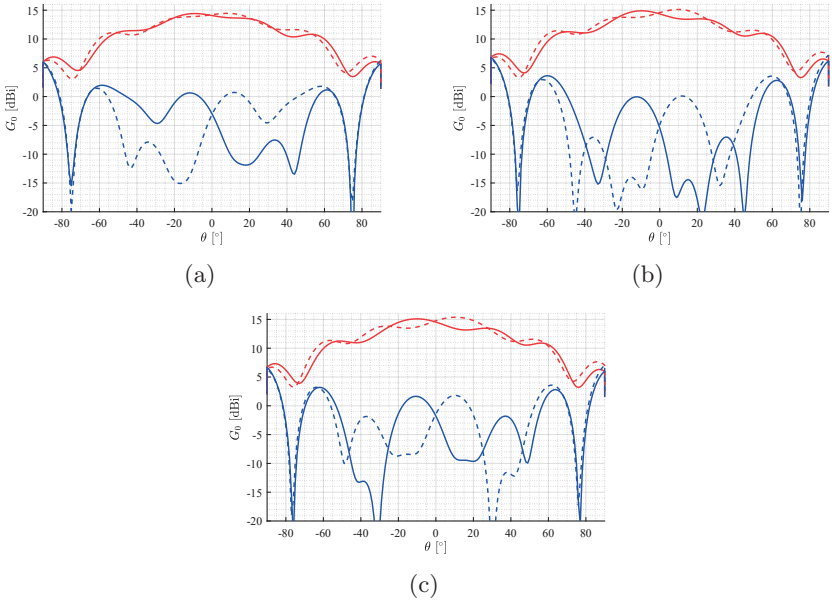


Figure 2.15: Co-polar and cross-polar radiation patterns of the antenna in the $xz$-plane for different frequencies: (a) 24.25 GHz, (b) 25.75 GHz and (c) 27.25 GHz. $G_0$ and $\theta$ stand for antenna gain and polar angle, respectively. (—— co-polar - P1, —— cross-polar - P1, - - - co-polar - P2 and - - - cross-polar - P2)

Table 2.5: 45°-slant polarized subarray structure key dimensions expressed in $\lambda_0$ at 28 GHz.

| *Parameter* | *Value* | *Parameter* | *Value* | *Parameter* | *Value* |
|---|---|---|---|---|---|
| $d$ | 0.56 | $sl_1$ | 0.61 | $sl_3$ | 0.51 |
| $b$ | 0.07 | $sw_1$ | 0.17 | $sw_3$ | 0.1 |
| $t$ | 0.15 | $sl_2$ | 0.07 | $sl_4$ | 0.07 |
| | | $sw_2$ | 0.1 | $sw_4$ | 0.18 |

## 2.7 45°-slant Polarized Antenna Element for Array Antenna

A design sketch of the structure of the antenna element is shown in Fig. 2.16(a), which is comprised of a $4 \times 1$ subarray of 45° slant-polarized slots. The corresponding main design parameters are listed in Table 2.5. In a phased array system with a fixed number of transmitting and receiving modules, subarraying increases the antenna element gain and provides a large area per antenna element for placing components on the PCB, which can reduce hardware complexity. Such an increase in antenna element gain, increases the EIRP and the signal-to-noise ratio (SNR) at the user equipment (UE) end, thus enhancing the cell-edge coverage. A disadvantage of this approach is, however, the reduced scanning range in at least one of the principal scanning planes, e.g., the elevation plane as in this chapter. In certain deployment scenarios of phased arrays, e.g., in low-rise urban, suburban, and rural environments the beam scanning coverage along the vertical axis can be reduced because the spread of users' positions in this direction is modest [58].

The 45° slant-polarized subarray is fed from the center with a ridge gap-waveguide line. The proposed antenna element in Fig. 2.16(a), offers its orthogonal polarization (−45° slant), merely by mirroring the slot layer with respect to $yz$-plane its center.

The slot layer structure includes slanted slots at the top and vertical slots at the bottom, which is similar to the implementations in [59], and Section 2.6. Vertical slots cut the transverse surface currents induced by the ridge gap-waveguide at locations where the currents are maximum. The vertical distance between the slots is $0.56\lambda_0$, however, they have in-phase electromagnetic fields. Between these two slots, there is a cavity facilitating the rotation of electric fields. As can be seen in Fig. 2.16(a), the centers of the vertical slot, cavity, and vertical slot are aligned along the $z$-axis. The layout of the slanted slots and their respective positions in the $xy$-plane are shown in Fig. 2.16(b). The 2D layouts of one vertical slot and one cavity are shown in Fig. 2.16(c) and Fig. 2.16(d), respectively.

Fig. 2.17 depicts the distribution of the electrical field (E-field) in the various areas of the slot layer. The vertical slot's horizontally polarized E-fields rotate in the cavity and become 45° slant-polarized in the slanted slot.

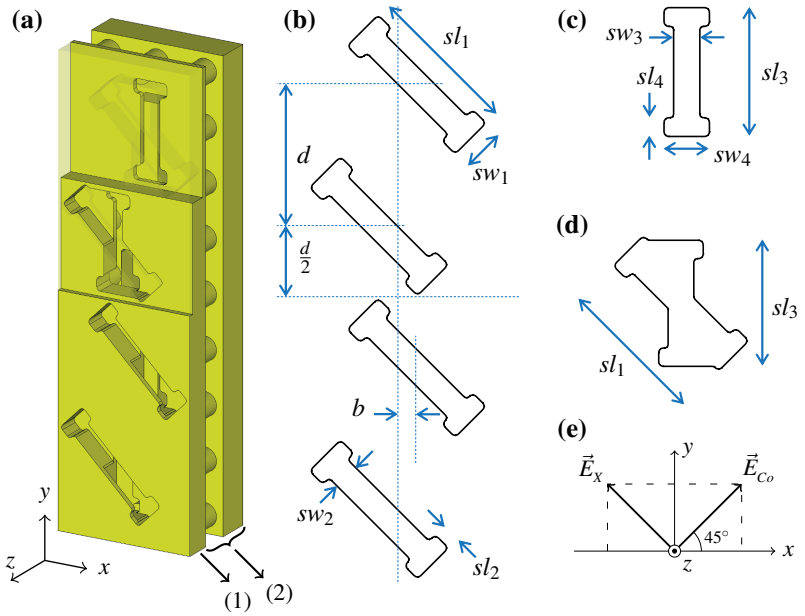


Figure 2.16: The design sketch of the subarray of four 45° slant-polarized slots. The whole subarray is shown in (a), comprising the slot layer (1) on top of the distribution layer (2). To visualize the cavity and vertical slot, some parts of the slot layer are shown transparently. (b) The layout of the slanted slots on top of the slot layer. (c) The layout of a vertical slot which is placed at the bottom of the slot layer. (d) The layout of a cavity between vertical and slanted slots. (e) The co-polar and cross-polar directions with respect to the slots and the cavity's orientation.

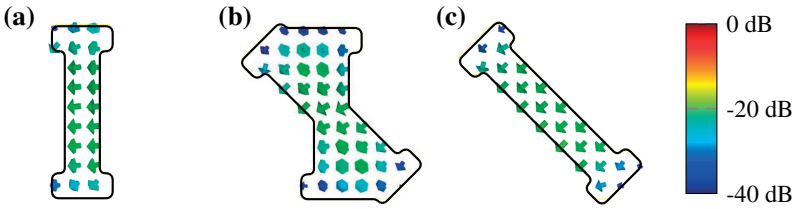


Figure 2.17: Simulated E-field distribution in the (a) vertical slot, (b) cavity, and (c) slanted slot of the slot layer. Simulation is performed at 28 GHz, and E-fields are normalized to the maximum value.

The cavity thickness is optimized to ensure maximum matching between the two slots, and it equals $0.09\lambda_0$.

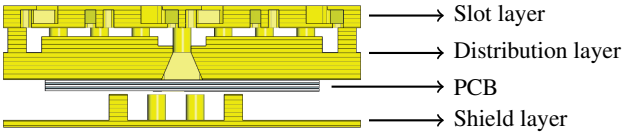


Figure 2.18: Cross section view of the subarray's stack-up. The stack-up shows the integration of through PCB transition with the subarray.

## 2.7.1 Integration with Through PCB Transition

### Unit Cell Antenna Element Model Performance

The subarray, comprising an antenna element and a transition, is simulated as a unit cell with periodic boundary conditions on each side (along the $x$- and $y$-directions in Fig. 2.18(a). CST Microwave Studio's time domain solver is used for the simulations. The subarray was excited by a waveguide port from the microstrip line. The simulated return loss ($|S_{11}|$), the azimuth pattern, and the elevation pattern at three frequencies (26.5, 28 and 29.5 GHz) are shown in Fig. 2.19(a), Fig. 2.20(a) and (b), respectively. It should be noted that the co-polarization (Co-pol) and cross-polarization (X-pol) directions are $(\hat{x}+\hat{y})/\sqrt{2}$ and $(-\hat{x}+\hat{y})/\sqrt{2}$, respectively, as shown in Fig. 2.18(e). The azimuth and elevation are defined on the $xz$- and $yz$-planes, respectively, and angles are measured from the $z-$axis. The subarray's impedance bandwidth defined at $|S_{11}| \leq -11$ dB is from $26.5-29.5$ GHz as required. Across the frequency range, the co-polar radiation pattern exhibits good angle coverage in azimuth and elevation planes. As subarraying is done in the vertical direction, the element pattern is narrower in the elevation plane compared to the azimuth plane. The X-pol level increases at angles far from the broadside in the azimuth plane due to the slanted slots' behavior.

### Embedded antenna element model performance

Another technique for simulating the antenna element combined with the transition is to integrate it into the phased array antenna. The radiation properties of an element are affected by its position in the array. The antenna elements are excited one at a time, while all the others are terminated, which is known as the embedded element antenna. For this simulation, an array consisting of $4 \times 16$ subarrays is simulated assuming the perfect matched layer (PML) boundary condition in every direction. The results are displayed in Fig. 2.19 and 2.20 for a subset of the elements. The results for the rest of the elements are omitted due to similarity. Fig. 2.19(b) shows the return loss for the elements at the array's corner, top edge, left edge, and center. All of the elements in the array's center work similarly. As shown from Fig. 2.19(b), the return loss of the antenna elements stays below $-12$ dB within the designated frequency range $26.5-29.5$ GHz. The mutual coupling between a set of selected array elements

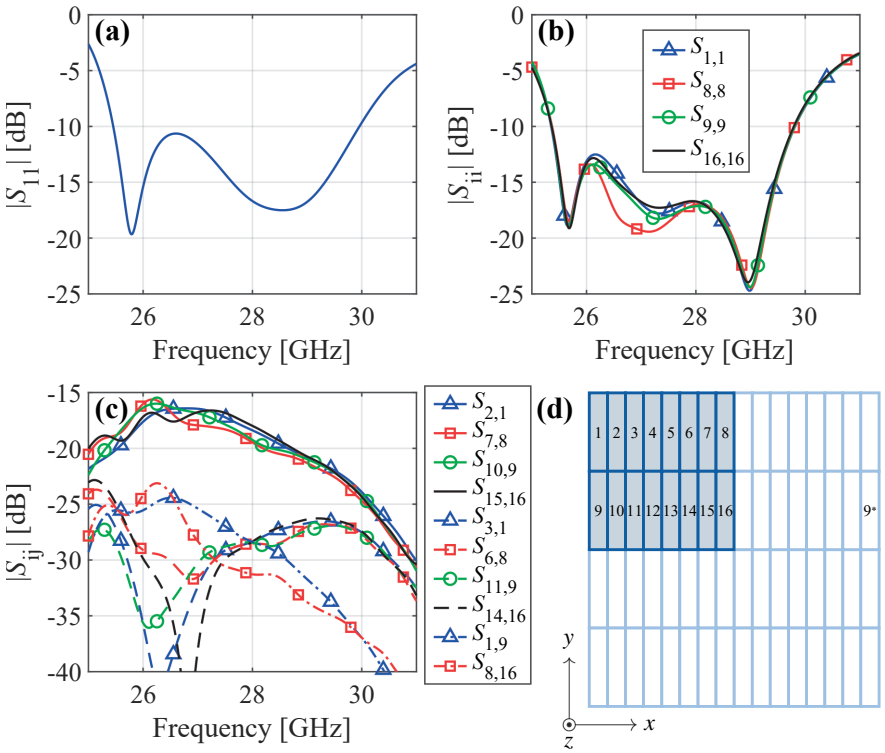


Figure 2.19: (a) Unit cell and (b) embedded return loss of the subarray. (c) The mutual coupling between different array elements. (d) The $4 \times 16$ layout of the array, which was used for embedded antenna element simulation.

is shown in Fig. 2.19(c). The coupling between neighboring elements is less than $-16.5$ and $-23$ dB in $x$- and $y$-directions respectively, for all elements over the whole frequency range. The higher level of $|S_{11}|$ in Fig. 2.19(a) is due to coupling from neighbor elements in the unit cell simulation, while they are terminated in embedded element simulation of $|S_{11}|$. The azimuth and elevation radiation patterns of these selected elements at 28 GHz are depicted in Fig. 2.19(c) and 2.19(d), respectively. The variable number of neighboring elements causes variation in antenna element performance, and this variation is the highest for edge elements in the array. A solution to make the performances more even is to add terminated dummy subarrays next to the array edges [60]. This method will increase the similarity of the elements' return loss and the mutual coupling.

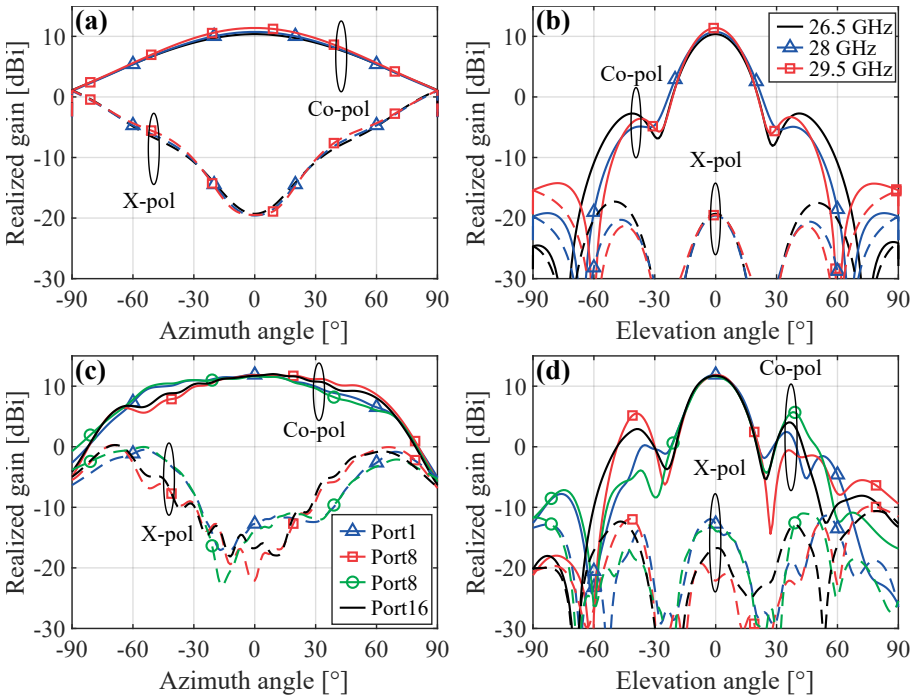


Figure 2.20: Unit cell radiation pattern of a subarray in (a) azimuth and (b) elevation planes at different frequencies. The embedded radiation pattern of a selected number of the array elements in (c) azimuth and (d) elevation planes at 28 GHz.

### Active reflection coefficient

The $4 \times 16$ array's active reflection coefficient is simulated with CST Microwave Studio's time domain solver following the subarray design. The structure has approximately $70,000,000$ meshes in a hexahedral shape. The smallest and the largest mesh sizes are $0.04\lambda_0$ and $0.54\lambda_0$, respectively. The small meshes are concentrated near critical areas, such as slots and waveguides, and they are employed to provide accurate electromagnetic field calculations in those areas. The simulation area's outer corners have larger meshes because they have weaker electromagnetic fields.

Active reflection coefficient for three specific scanning angles are shown in Fig. 2.21. Only the results of a row of elements in the middle of the phased array antenna are given here. Due to the similarity of results between the rows, the results from the other rows are omitted. The results for ports 9, 16, and 9*—which are located on the left edge, center, and right edge of the row, respectively—are highlighted in the figure. The active reflection coefficient varies depending on the scanning angle for each element since it is affected by

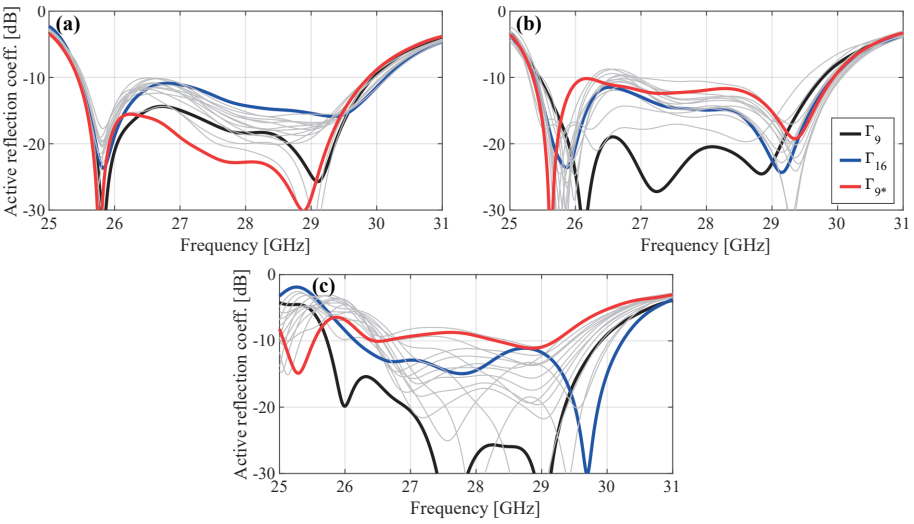


Figure 2.21: Active reflection coefficient of one row of elements when scanning to different azimuth plane angles. (a) Broadside, (b) Azimuth +30°, and (c) Azimuth +60°.

the element position and embedded pattern [61]. The antenna is matched for all scanning angles up to ±60° in the azimuth plane (lower than −10 dB), while at ±60°, the matching is better than −7 dB over the designated band. The active reflection coefficient in the elevation plane within the ±10° range is similar to the broadside radiation results. This is due to the low coupling between neighboring elements in the $y$-direction.

## 2.8 Summary and Conclusions

Three types of microstrip-to-ridge gapwaveguide are presented in this chapter. Their characteristics, including return loss, insertion loss, and isolation, are discussed. Transitions are vertical, compact, and contactless. They are designed for $26.5 - 29.5$ GHz, in which all types show insertion loss less than 0.6 dB, return loss less than −15 dB, and isolation better than 20 dB. Based on gapwaveguide technology, these features are ideal for 5G mmWave phased arrays. All transitions are designed for 28 GHz as the center frequency, and their performance is evaluated when integrated with a previously designed antenna array.

A wideband through PCB microstrip-to-waveguide transition was designed to provide optimal power transfer to a ridge gapwaveguide following the principles outlined in [50, 51].

A linear array antenna with 8 elements has been designed based on the gapwaveguide technology. Each element has 8 radiating slots and is fed from the

center. This antenna is suitable for 5G applications in the mmWave frequencies and can scan the E-plane in the $\pm 45^\circ$ range. The active reflection coefficient of the antenna in all scan angles and all frequencies is less than $-10$ dB and the gain is 23 dBi in broadside angle on average.

A slant dual-polarized antenna design based on the gapwaveguide technology is presented in this chapter. Two arrays of 8 radiating slots with slant polarization produce the two orthogonal polarizations. Each polarization has 14.5 dBi gain on average with a maximum $-15$ dB lower cross-polarization level in the operational frequency band of the antenna. The antenna covers the frequency band 24.25 to 27.25 GHz, which makes it suitable for 5G applications in mmWave frequencies.

A novel simple and low-profile $45^\circ$-polarized phased array antenna element is introduced. The main challenges in such design are (I) high inter-element isolation, (II) reducing the inter-element distance to $0.56\lambda_0$, and (III) large space for slots is required per element, as the rotating slots occupy more space than vertical slots. The solution proposed requires only two layers, whereas state-of-the-art uses three layers, and supports a full scanning range in azimuth. It significantly improves the feasibility of gapwaveguide-based phased arrays with slant polarization.

# Chapter 3

# Gapwaveguide-based Large High-EIRP Phased Array Antenna at 28 GHz

## 3.1 Introduction

To compensate for the high path loss and to maintain a practical link budget, phased array antennas with many antenna elements come in handy. They allow producing base stations with high output power while being able of tracking mobile users with high-resolution thanks to high directivity and the wide scanning ranges obtained with large array antennas.

The two main challenges in the design of antenna elements and last stage feed lines of a large phased array are: (i) the design complexity and (ii) the antenna bandwidth. Complexity leads to higher costs, while bandwidth is essential to provide a high data rate link to users in 5G and beyond wireless communications. At 28 and 38-GHz frequency bands, state-of-the-art phased array antennas commonly use substrate-based antenna elements [13, 14, 16, 17, 26, 33, 34, 62–64]. Antennas are typically integrated with other circuitry, such as mixers, feeding networks, and beamforming networks, e.g., beamformer integrated circuits (BFIC). Multiple layers of printed circuit boards (PCB) are required for BFICs to deliver the DC power and the control signals. When substrate-based antennas are combined with a PCB, the number of PCB layers rapidly increases, and therefore the losses too. This increase may also be necessary in order to increase antenna bandwidth [34, 35], or to accommodate the routing from the BFIC to the antenna port [23]. However, a high number of layers usually results in high complexity and therefore in high costs of the PCB design. Buried and blind vias can additionally complicate the manufacturing,

This chapter is a reprint material as it appears in [A], and [E]. The dissertation author was the primary investigator and author of these papers.

altogether increasing the cost of the active phased array antenna [16, 23].

In state-of-the-art phased array designs with a large number of antenna elements, a compromise is made regarding complexity, bandwidth, ohmic losses, dielectric losses, and mismatch. Feeding patch antennas directly with a via probe is a common way to achieve low-loss last-stage feeding in 28 GHz phased arrays. In [16], a phased array with 16 layers of PCB, including an air cavity, was proposed, where 10 layers were dedicated only to antenna elements and feed lines. The achieved antenna element gain was from $4-7$ dBi with about 2 GHz bandwidth at 30 GHz. In [14] and [13], losses of $<$1 dB and $0.8-1.3$ dB with a 12-layer PCB and bandwidth from $28-32$ GHz have been reported, respectively. In [31], a 7-layer of PCB stack with narrow band single-layer probe-fed patch antennas with 4 dBi gain was employed, which limited the bandwidth of the phased array. In all the mentioned cases, 6 layers of the PCB were dedicated to DC power, control signals distribution, and connection to BFIC's common port. The use of endfire antenna elements, such as the printed dipole and the Yagi-Uda can increase complexity and losses. In [17,64], multiple PCBs were implemented in a 2D array design; one PCB per antenna column, which can result in an alignment issue. The reported losses from the PA output to the antenna element port were 3.5 and 6 dB, respectively.

Gapwaveguide technology can be used to reduce the complexity of the PCB design while supporting a large bandwidth and minimizing feeding losses. It has been used widely to design high gain and low loss slot array antennas at mmWaves [36–38]. This technology has been proposed as a good candidate for providing a fair trade-off between manufacturing cost and manufacturing flexibility of electromagnetic components [19,39]. The main contributions presented in this chapter are listed below:

- A novel low-profile 45°-polarized phased array antenna element has been proposed and experimentally verified. The proposed solution requires only two layers and supports a full scanning range in azimuth. It significantly improves the feasibility of gapwaveguide-based phased arrays with slant polarization. The main design challenges that we have resolved are due to various competing mechanisms, (i) reducing the inter-element distance, e.g., to $0.56\lambda_0$ to avoid grating lobes, (ii) as inter-element spacing is reduced, mutual coupling must be reduced too because it impacts array performance, and (iii) on the other hand, large space is required for slot-elements because as a result of the rotation the slot- elements will occupy more space than vertical slots.

- A PCB with a low number of layers compared to common wideband 28 GHz phased arrays is utilized. Despite being a large $16 \times 16$ array, only 6 PCB layers are used, against 12 layers of a state-of-the-art 28 GHz phased array with a similar methodology. This is achieved by separating the radiating elements of the phased array from the PCB and maintaining the wideband properties of waveguide antennas.

- The proposed design is substantially larger in complexity and raw output

power, with a $16 \times 16$ configuration and 65 dBm EIRP, compared to the previous design in [19]. The increase in size and power brings important aspects of the complexity of the whole system, including PCB design and antenna manufacturing.

## 3.2 Phased Array Antenna Design

A large phased array antenna consisting of $16 \times 16$ radiating elements is developed and manufactured, allowing for high antenna gain and EIRP, making it suitable for high data rate communication. The phased array antenna consists of multiple layers with the stack-up depicted in Fig. 3.1. The layers are from top to bottom: the slot layer, the distribution layer (i.e., discussed in the last chapter), the PCB layer, and the shield layer.

Fig. 3.2 shows a block diagram of RF components on the PCB. The array makes use of four mmWave frequency highly-integrated silicon up/down converter ICs (UDC). Each UDC has a $\times 4$ local oscillator (LO) multiplier [65]. Each UDC supports a quarter of the array, and the structures of all quarters are comparable. UDCs are connected to separate transmit (TX) and receive (RX) connectors via 50 $\Omega$ striplines, allowing each UDC to function independently, whether in TX or RX modes. With this concept, four beams can be produced at the same time, meaning that hybrid beamforming can be achieved. The LO frequency is set to 5.6 and 5.975 GHz for the lower and upper-frequency bands, respectively, and the IF band (both for RX and TX) is set to $4.1 - 5.6$ GHz. This configuration allows covering the band from $5.6 \times 4 + 4.1 = 26.5$ GHz to $5.975 \times 4 + 5.6 = 29.5$ GHz. It should be pointed out that the PCB occupies the same surface area as the antenna layers do, including up/down conversion and beamforming.

As shown in Fig. 3.2, the phased array comprises 16 BFICs that are connected to 4 antenna elements each, i.e., in a $1\times4$ architecture. BFICs are produced with NXP's SiGe technology and have four bidirectional channels. All device functions are digitally controlled and monitored via a high-speed serial peripheral interface (SPI) interface [66]. Each channel has a TX and an RX chain, both of which contain a high-resolution phase shifter and a variable gain amplifier (VGA). The VGA gain control in the TX and RX chains is 25 dB and 30.5 dB, respectively. The transmit chain 1 dB output power compression point (P1dB) of each channel is 19 dBm. This BFIC is packaged by wafer-level chip-scale packaging (WLCSP) process with small dimensions of $4.39 \times 3.59 \times 0.5$ mm$^3$. The metallic shield layer, shown in Fig. 3.1, dissipates heat from the BFIC and aids in its temperature stability.

The PCB stack-up depicted in Fig. 3.3 contains six layers. RO4350B and RO4450F with the properties mentioned in the previous section are used as core and prepreg substrates, respectively. The UDCs, BFICs, Wilkinson power divider/combiners, and all 50 $\Omega$ microstrip routing lines are located on the top metal layer (M1). The main trace of striplines is on Layer M4. Layers M2 and M6 serve as grounding for IF and RF frequency signals. Each BFIC channel is

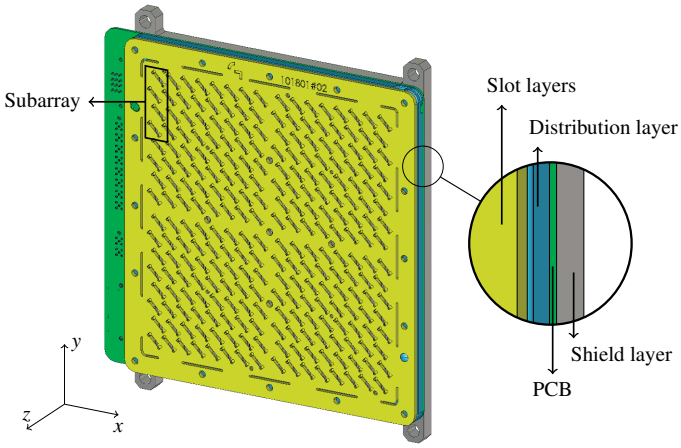


Figure 3.1: Stack-up of the array antenna system. Layers from top to bottom: slot layer, distribution layer, PCB, and shield layer.

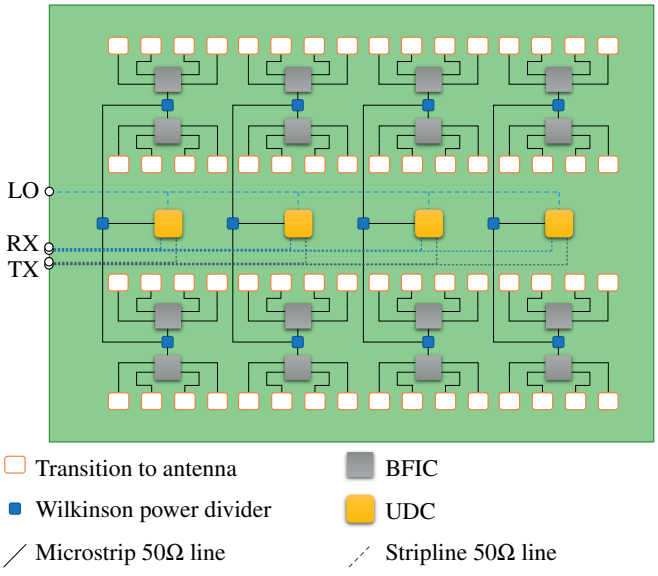


Figure 3.2: RF PCB block diagram.

linked to one antenna element array through the transition from microstrip to double ridge waveguide.

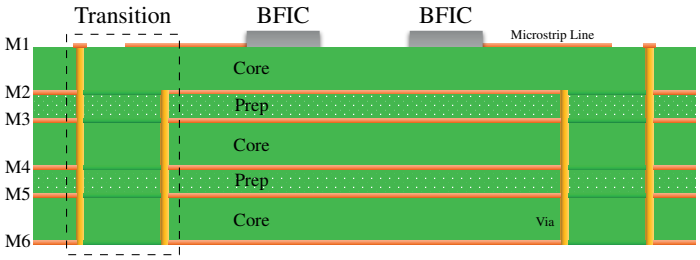


Figure 3.3: 6-layer RF PCB stack-up

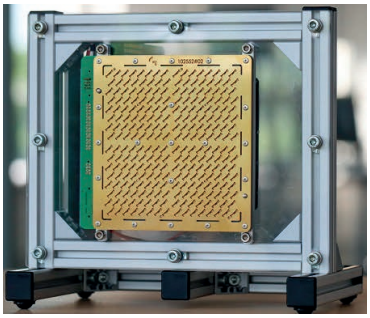

Figure 3.4: The phased array antenna prototype mounted on the fixture.

## 3.3 Phased Array Prototype Measurements

In this section, we present the measurement results performed on the manufactured prototype. Measurements are compared to simulations. In the first part, we present the calibration procedure prior to performance measurements.

Fig. 3.4 shows the assembled phased array mounted on a fixture. Although not shown, the fixture includes a 1 to 4 power dividing/combining network connected to the IF ports, and an SPI interface circuit providing communication to the ICs through a universal serial bus (USB) connector.

The slot layer is made with an aluminum etching process, while the distribution and shield layers are made with aluminum milling. These processes add a $\pm 20$ µm tolerance (equivalent to $\pm 0.002\lambda_0$) to the dimensions of the layers. The nominal tolerance for layer misalignment, when assembled on top of each other, is $\pm 10$ µm ($x$- and $y$-directions in Fig. 3.4). The simulation shows minor changes in the results within the manufacturing tolerances specified.

### 3.3.1 Calibration Measurements

Active phased arrays need to be calibrated in order to achieve high performance by removing undesired non-idealities. Indeed, although the design presented

is identical in all parts, there will be unavoidable differences between channels due to edge effects, manufacturing, assembly, and the differences between the components, especially the BFICs. If the phase and gain difference between channels is large, the phased array may not perform as desired. For example, the resulting far-field pattern may display high side lobe levels, the main lobe pointing direction might deviate and the corresponding gain might be lower. Fig. 3.5(a) shows the normalized co-polar radiation pattern of the phased array without calibration, where for the sake of comparison, the corresponding ideal radiation pattern obtained from simulations is also included.

Numerical simulations were performed in order to gain further insight into the impact of non-idealities, e.g., variations of the phases and the amplitudes of the excitation of the antenna elements on the radiation pattern. The variations are assumed to follow the Gaussian probability distribution, which are added to the ideal (simulated) phases and amplitudes of each antenna element. They are independent and have zero means with standard deviations of 1 dB and 9° for amplitude and phase of excitation, respectively [13].

The resulting simulated performance deviation, e.g., in terms of the side lobe level (SLL) and antenna gain errors, arising from the random element excitation variation in phase and amplitude is shown in Fig. 3.5(b)-(d). As can be seen from the simulation results, when only excitation phase variation is applied (Fig. 3.5(b)), on average a −0.1 dB antenna gain and a 0.4 dB SLL degradation are observed. But when only amplitude excitation variation is applied (Fig. 3.5(c)), the average antenna gain error is −0.05 dB and the SLL error is negligible. Finally, combining both amplitude excitation and phase variations (Fig. 3.5(d)) will result in −0.16 dB and 0.5 dB average antenna gain and SLL errors, respectively, where Fig. 3.5(b) and (c) suggest it is mainly due to phase variation.

In this work, only channel phase calibration has been performed while no channel gain calibration is considered. This is because the measured channel gain variation is in the ±1 dB range. However, due to unequal lengths in the IF-feed network from the RX/TX connector on the PCB to the UDCs, a calibration of the UDC-gain levels was performed prior to the main calibration. In this way, an even gain distribution to the common ports of BFICs is achieved.

The phased array antenna prototype was fully calibrated and characterized in far-field ($> 2D^2/\lambda_0$) using a vector network analyzer (VNA) and a standard gain horn antenna. The calibration routine follows the method presented in Appendix I of [67]. During the calibration procedure, the phase of one element is shifted from 0 to 360°, while measuring the array's received/transmitted power with the VNA. The element's phase can then be calculated after that. The process is then repeated to obtain the phase of the next element.

### 3.3.2 Radiation Pattern Measurements

The normalized radiation pattern was measured in a fixed configuration that included all TX/RX, scanning angles, and azimuth/elevation. This helps to

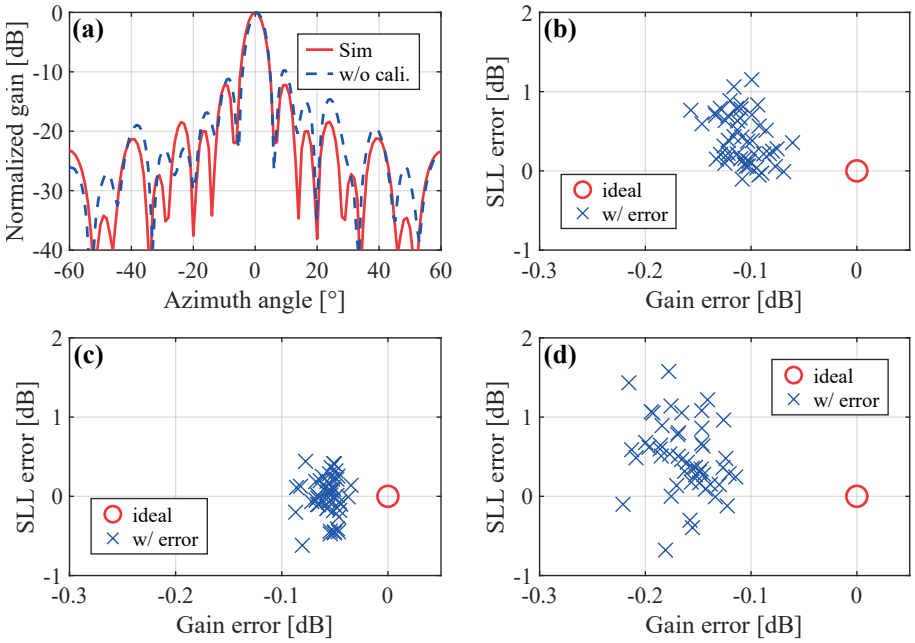


Figure 3.5: (a) Measured radiation performance of the array antenna at broadside without calibration compared with simulation at 28 GHz. SLL and antenna gain error (b) with random excitation phase only (Gaussian distribution with zero-mean and 9° standard deviation), (c) with random excitation amplitude only (Gaussian distribution with zero mean and 1 dB standard deviation), and (d) with random excitation phase and amplitude at the same time but independently, at 28 GHz broadside.

compare all of the measurement cases fairly. Although all the aspects for reducing the systematic error were considered, the measurement results are estimated to have a ±0.5 dB uncertainty. This uncertainty is caused by angular misalignment of the antennas, temperature drift of ICs, and measurement equipment added noise.

Fig. 3.6 shows the measured co- and cross-polar farfield patterns after full calibration. Fig. 3.6(a) shows the co- and cross-polar azimuth patterns for the broadside scanning angle, while Fig. 3.6(b) shows results for the −40° scanning together with their corresponding simulation results. The measurement results are in good agreement with simulations in terms of SLL, nulls, and beamwidth. The deviation of the scanning angle (squint) over the target frequency band is shown inset of the respective figure for each case. This deviation is not more than 1°, demonstrating the beams' stable pointing over frequency.

In order to evaluate the radiation pattern performance at different frequencies and at different scanning angles the gain roll-off for the main lobe and the corresponding SLL were computed from both simulations and measurements.

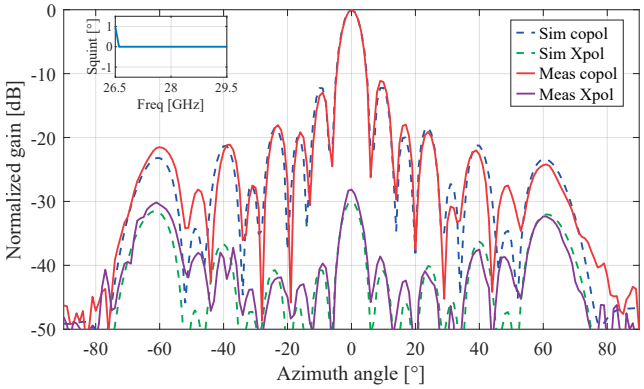


(a) Broadside

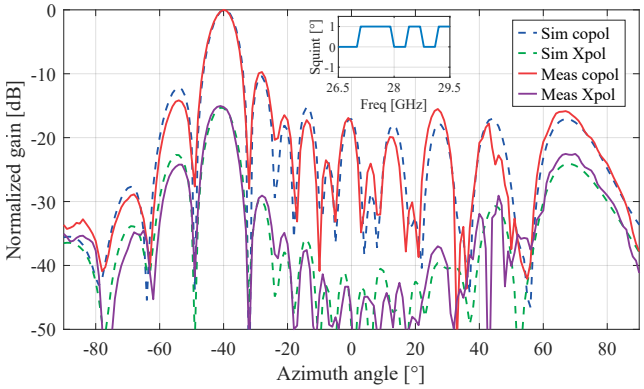


(b) Azimuth −40°

Figure 3.6: Radiation pattern of the antenna for two scanning angles at 28 GHz in TX mode. For each case, the squint in the azimuth plane over frequency is shown inset of the figure.

The gain roll-off is defined here as the difference in dB between the gain in the main lobe at a scanning angle and the gain in the broadside direction at a given frequency. The results are summarized in Fig. 3.7 and presented over the whole scanning range in both azimuth and elevation and within the working bandwidth of the antenna for both the RX and the TX modes of the array antenna.

As can be seen from Fig. 3.7c and e, the gain roll-off in both TX and RX modes obtained from measurements are in good agreement with the simulations in Fig. 3.7a. The error stays within ±1 dB for all scanning angles over the frequency band of operation. Also, by comparing Fig. 3.7d and Fig. 3.7f it can be noted that the measured SLL in the azimuth plane is less than −9 dB for the majority of scanning angles from −50° to +50°. Furthermore, high side lobes are seen from Fig. 3.7b, d and f, for scanning angles smaller than

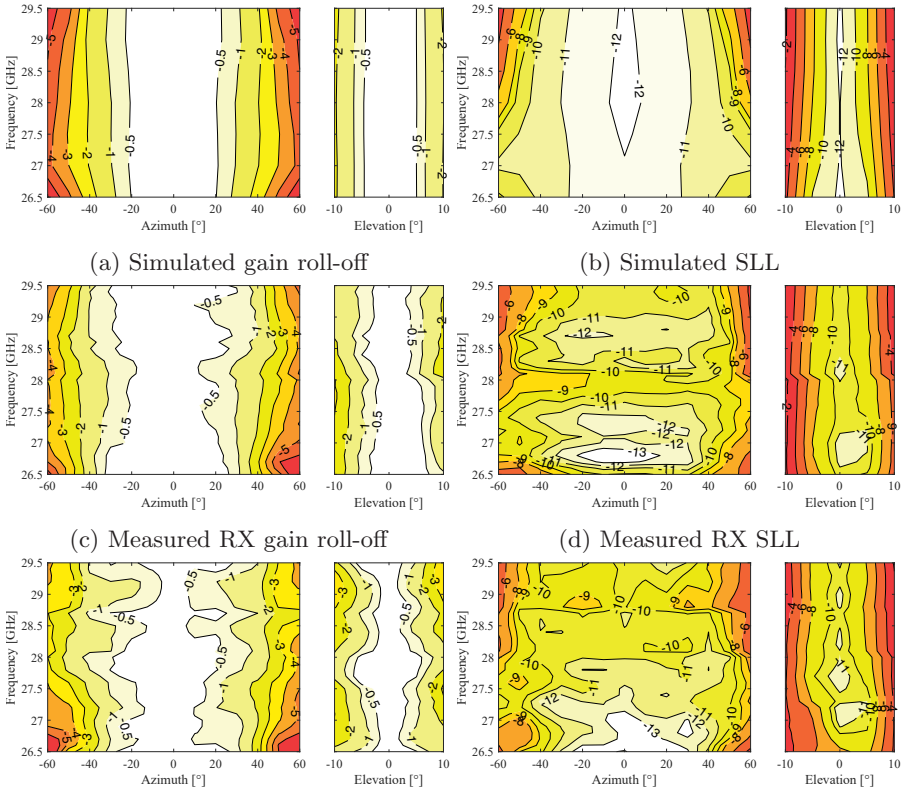


(a) Simulated gain roll-off (b) Simulated SLL

(c) Measured RX gain roll-off (d) Measured RX SLL

(e) Measured TX gain roll-off (f) Measured TX SLL

Figure 3.7: Radiation performance of array antenna in simulation, RX and TX modes.

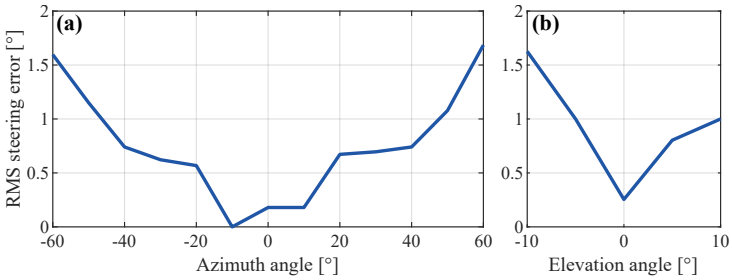


Figure 3.8: RMS steering angle error over all RX mode measured frequency samples in (a) azimuth and (b) elevation planes.

−50° and larger than +50° in the azimuth plane, and for frequencies above 28 GHz. A further comparison between measurements and simulations shows

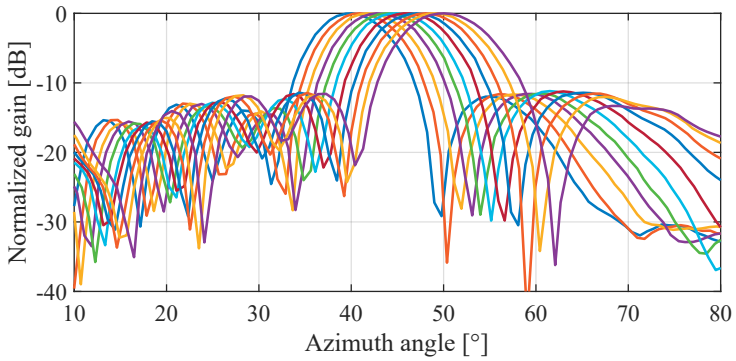


Figure 3.9: Fine scanning resolution with 1° step at 28 GHz in RX mode.

good agreement for SLLs in the elevation plane as shown in Fig. 3.7b, d and f. However, in this plane, grating lobes appear for scanning angles smaller than $-5°$ and larger than $+5°$ due to the large separation distance between elements.

The root mean square (RMS) steering angle error of RX mode is shown in Fig. 3.8. At each angle, the error is calculated over all measured frequency samples in the $26.5 - 29.5$ GHz band. The accuracy of the calibrated steering angle is 1.6° or less. The error is caused by different factors, such as beam squint over frequency, pattern shape, and phase quantization error of phase shifters. The beam squint has no effect on the broadside, but it gets worse in the angles with larger absolute values. Due to lower gain and wider beamwidth in angles further from the broadside, the pattern shape has a similar impact to the beam squint. The phase quantization error results in an error that is constant across all angles. It is worthwhile to note that it is the only factor that causes the error for angles near the broadside. Given the little RMS steering error at those angles, phase quantization's impact appears to be minimal. Fig. 3.9 shows the measured radiation pattern of multiple beams in the azimuth plane with 1° steps. Due to the use of 8-bit phase shifters in BFIC, achieving a 1° resolution is expected [68]. Hence by considering this resolution and measured SLLs in Fig. 3.7, the proposed phased array antenna shows a high scanning resolution capability without degrading SLLs, which is essential to achieving high SNR for 5G transceivers [17].

### 3.3.3 EIRP Measurements

The phased array's EIRP is characterized in TX mode. It was determined by calibrating the entire setup with a standard horn antenna. Considering that the horn antenna's gain was known, the entire loss of free space, all cables, and the reception antenna were all measured. The standard horn antenna was replaced with the phased array in TX mode. To maintain the same loss of free space, the aperture positions of both antennas were the same.

The measured EIRP at the broadside scanning angle of the antenna versus

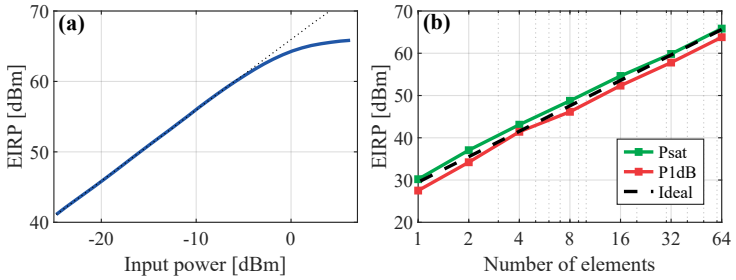


Figure 3.10: EIRP measurement at broadside angle and 28.5 GHz versus (a) input power and (b) number of elements.

the input power is shown in Fig. 3.10(a). The EIRP achieves the 1 dB compression point (P1dB) at 63.4 dBm and saturates at 65.5 dBm (Psat). The power consumption per channel in TX mode at a 9 dB back-off from P1dB and in RX mode are 225 and 155 mW, respectively. These values are achieved in the whole IF to RF chain including the up/downconverter integrated circuits (UDCs) and the $1 \times 4$ transceiver beamformer integrated circuits (BFICs). This agrees well with the design assumptions

$$EIRP_{\mathrm{P1dB}} = OP1dB_{\mathrm{BFIC}} + G_{\mathrm{subarray}} + 20\log_{10}(N), \tag{3.1}$$

where $EIRP_{\mathrm{P1dB}} = 65.5$ dBm is the phased array EIRP at P1dB, $OP1dB_{\mathrm{BFIC}} = 19$ dBm is the BFIC output power at P1dB, $G_{\mathrm{subarray}} = 10.5$ is the subarray antenna gain including feed, ohmic and mismatch losses, and $N = 64$ is the total number of subarrays. The difference between the measured and expected value of $EIRP_{\mathrm{P1dB}}$ can be due to a variation of the output power of BFICs which will result in power amplifiers going into compression at lower input power and higher loss in the antenna elements.

Fig. 3.10(b) shows the measured EIRP versus the number of active elements at Psat and P1dB. Ideally, halving the number of active elements should result in a 6 dB drop in EIRP. This is depicted by the ideal straight line in the figure. The EIRP at Psat and the ideal straight line intersect at 64 elements. As the number of elements decreases, a deviation from the ideal line appears, which can be explained by the variation in radiated power among the single antenna elements of the array.

### 3.3.4 Comparison with the State-of-Art

A comparison with the state-of-art phased array antennas at 28 GHz band is presented in Table 3.1. The comparison criteria comprise the PCB complexity, antenna subarrays/elements characteristics, and active array performance parameters, e.g. array size, coverage, and EIRP. Comparing the phased arrays in terms of front-end losses, it can be seen that the proposed design has similar loss levels as the other very low loss designs in [13,14] while demonstrat-

ing a much lower PCB design complexity. The proposed phased array design achieves EIRP as high as in [33], while it has a lower number of RF chains, and consequently lower power dissipation density and consumption due to the implementation of subarrays,

Table 3.1: Summary and comparison with the state-of-art 28 GHz phased arrays

| | | This work | UCSD '20 [14] | UCSD '18 [13] | Tokyo Tech '20 [31] | IBM '17 [26, 32] | UCSD '20 [33] | Tokyo Tech '19 [17] |
|---|---|---|---|---|---|---|---|---|
| **Frequency [GHz]** | | $26.5-29.5$ | $28-32$ | $28-32$ | 28* | $27.2-28.8$ | $24-29.5$ | $26.5-29.5$ |
| **Antenna technology** | | Gap-waveguide | Dual-pol stacked patch | Stacked patch | Dual-pol patch | Dual-pol stacked patch | Stacked patch | Printed dipole array |
| **PCB complexity** | | 6 layers w/ 3 metal plates | 12 layers | 12 layers w/ buried vias | 7 Layers | 16 layers w/ buried vias and air cavity | 12 layers | Separate boards per subarray column |
| **front-end losses [dB]** | **Feed line** | 0.3 | $< 1$ | $0.8-1.3$ | - | - | - | 6.04# |
| | **Antenna's ohmic loss** | 0.55 | | | - | - | - | - |
| | **Mismatch** | 0.45 | 0.45 | 0.45 | - | - | - | - |
| **Subarray/ element** | **size** $[\lambda_0^2]^\diamond$ | $2.24 \times 0.52$ | $0.62 \times 0.5$ | $0.63 \times 0.5$ | $- \times 0.56$ | $0.59 \times 0.59$ | $0.48 \times 0.51$ | 0.54 |
| | **antenna gain [dBi]** | 10.5 | 4.5 | 4.5 | 4 | 3-4 | 4 | 11.9 |
| **TX P1dB/channel [dBm]** | | 19 | 11-12 | 11-12 | 11.3 | 13.5 | 11.5-12 | 15.7 |
| **Array size** | | $4 \times 16$ | $8 \times 8$ | $8 \times 8$ | $2 \times 16$ | $8 \times 8$ | $16 \times 16$ | $1 \times 8$ |
| **Polarization** | | Single | Dual | Single | Dual | Dual | Single | Single |
| **Scanning performance** | **Az/El angular range [°]**† | $\pm 10 / \pm 60$ | $\pm 25 / \pm 50$ | $\pm 25 / \pm 50$ | $- / \pm 50$ | $\pm 50 / \pm 50$ | $\pm 50 / \pm 60$ | $- / \pm 50$ |
| | **Max. scan loss [dB]** | 6 | 3.9 | 5 | 6 | 5 | - | 5 |
| **EIRP @ P1dB [dBm]** | | 63.4 | 50-51 | 50 | - | - | 63.5 | 36.5 |
| **EIRP @ Psat [dBm]** | | 65.5 | 52 | 51-52 | 45.6 | 54 | 65.5 | 39.8 |

* Narrow bandwidth antenna design at 28 GHz center frequency.
# It includes SMPM connector and bond wire.
$^\diamond$ Sizes are in terms of free space wavelength of the respective center of frequency bands.
† It is defined as the ability to scan in respective planes with uniform excitation amplitude, and without grating lobes.

## 3.4 EVM Verifications

The high data rate performance of a phased array is primarily determined by the linearity and signal-to-noise (SNR) performance of the chipsets used in the design of the phased array antenna system, the performance of which is beyond our scope. On the other hand, the Error Vector Magnitude (EVM) is a measure of the difference between the ideal transmit symbols and the measured symbols after the equalization. Modulation quality is defined by the difference between the measured carrier signal and a reference signal. Hence, data transmission quality can be expressed in terms of the EVM [69]. The EIRP of a beam produced by a phased array depends on the realized array gain times the input power delivered by the power amplifiers to an antenna element (can be a sub-array, i.e., smaller array) divided by the feeding losses.

In this section, (non-standardized) over-the-air (OTA) measurements over a short indoor link showing radiation patterns, EIRP, and EVM versus scan angle are presented. It is shown that the design of a low profile, low structure complexity, phased array antenna system with high EIRP, up to 60.5 dBm, and low EVM, i.e., less than 2 % is feasible at the mmWave frequencies for the considered scenario.

### 3.4.1 Measurement Setup

The capability of the proposed phased array to sustain a high data rate link was verified by performing over-the-air (OTA) measurements in the transmit (TX) mode. The complex modulation performance of the phased array was evaluated using the measurement setup shown in Fig.3.11. An Agilent Arbitrary Waveform Generator (AWG) model M8190A is used to generate a complex modulated signal at the intermediate frequency (IF) of 2.62 GHz. The AWG generates QAM-modulated waveforms with different symbol rates and with a pulse-shaping filter (root-raised cosine filter) of $\alpha = 0.35$. A Keysight PNA-X Network Analyzer model N5247B was connected to the receive (RX) standard horn antenna. The transmit (TX) radio frequency (RF) signal was a single frequency within the operation band of the phased array from $26.5 - 29.5$ GHz. The RX signal is demodulated and compared with the TX signal, which is done with a MATLAB program. The horn antenna has a gain of 25 dBi and is placed at a 3 m distance in the line of sight path with respect to the phased array's main beam. The PNA-X also functions as a local oscillator at 6.595 GHz and is connected to the phased array's LO port.

### 3.4.2 Results and Analysis

Various combinations of the parameters of the system were used to study the EVM and EIRP interrelationship. Four azimuth scanning angles were considered, i.e., 0° (broadside direction, no scanning), 20°, 40°, and 60°. Four quadrature amplitude modulation (QAM) constellation orders were considered, namely, 16−QAM, 64−QAM, 128−QAM, and 256−QAM. In order to study

Figure 3.11: Schematic representation of the non-standardized over-the-air (OTA) measurement setup in an indoor environment.

Table 3.2: EIRP values of the phased array at 28 GHz.

| AWG (mVpp) | 200 | 400 | 600 | 800 |
|---|---|---|---|---|
| AWG (dBm) | -10 | -4 | -0,5 | 2 |
| Pin (dBm) | -17 | -11 | -7,5 | -5 |
| EIRP* (dBm) @ 0° | 49 | 55 | 58,5 | 60,5 |
| EIRP (dBm) @ 20° | 48,6 | 54,6 | 58,1 | 60,1 |
| EIRP (dBm) @ 40° | 47,2 | 53,2 | 56,7 | 58,7 |
| EIRP (dBm) @ 60° | 45 | 51 | 54,5 | 56,5 |

*The relation between input power and EIRP @ 0° is provided in Fig. 3.10.

the impact of the noise three different IF (AWG) bandwidths of the modulated signals were used: 100, 250, and 500 MS/s. The input signal voltage of AWG was varied at four levels: 200, 400, 600, and 800 mVpp (mVpp = millivolts peak to peak). The signal is fed to the phased array through a coaxial cable with 7 dB insertion loss at 28 GHz. The EIRP associated with AWG levels is provided in Table 3.2. All combinations of the above cases have been measured.

First, we consider the case when the phased array radiates at the broadside angle (i.e., no scanning with azimuth and elevation angles). The signal's data rate is 3 Gb/s computed for a transmission of 64−QAM modulated signals at a symbol rate of 500 MS/s, and the signal bandwidth is 675 MHz. The EIRP values are 19, 55, and 60.5 dBm (the first one has been achieved with 30 dB attenuating the AWG's 200 mVpp signal, and the latter one corresponds to a 5 dB back-off from saturated EIRP). The corresponding measured error vector magnitude (EVM) values are 3.1, 1.2, and 2.6 %, respectively.

Fig. 3.12 shows the constellations of the 64−QAM modulated signals with the EIRP and EVM values mentioned above. As shown in Fig. 3.12, signal distortion in the link is very low, as measured by the EVM. The relatively higher EVM value, i.e., more distortion at low EIRP, is due to the dominance

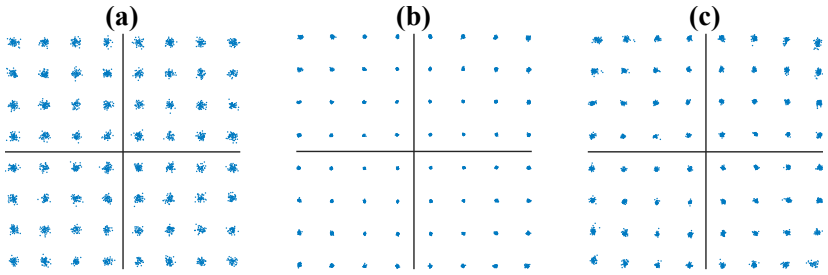


Figure 3.12: Measured constellation errors for a 64−QAM modulated transmission at 500 MS/s (equivalent to 3 Gbps transmission rate) (a) EVM=3.1 % and EIRP=18 dBm, (b) EVM=1.2 % and EIRP=55 dBm, and (c) EVM=2.6 % and EIRP=60.5 dBm (at 5 dB back-off from saturation). See Fig. 3.11 for OTA measurement.

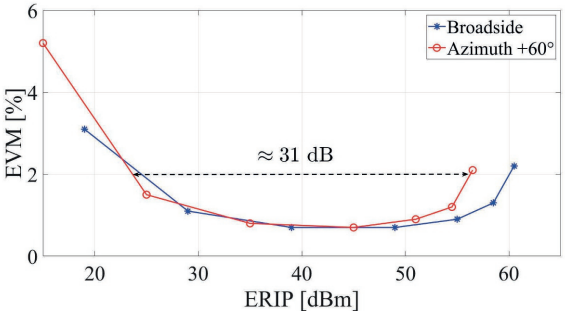


Figure 3.13: TX EVM vs. EIRP measured over-the-air at a 3 m TX-RX separation for a 64−QAM modulated transmission at 250 MS/s (equivalent to 1.5 *G*bps transmission rate) at the indoor measurement setup shown in Fig. 3.11.

of noise in the system. Meanwhile, at high EIRP non-linearity of amplifiers in the phased array distorts the signal.

Next, we consider the measured EVM while scanning the beam. Fig. 3.13 shows the EVM as a function of EIRP based on measurements employing a 64−QAM modulated signal with 250 MS/s, centered at 28 GHz. The measurements were performed at broadside, i.e., 0° in azimuth and elevation and an azimuth scanning angle at 60°. The latter is the largest steering angle of the devised phased array antenna. It should be noted that additional measurements were performed employing attenuators to obtain lower EIRP values than those generated using the AWG.

As can be seen from Fig. 3.13, at high EIRP, the linearity of the active beamforming power amplifier is the limiting factor as the EVM increases at peak transmit powers. The EVM rise at the 60° azimuth steering angle occurs

at lower EIRP than the broadside radiation because of antenna gain scan loss. This difference in EIRP is 4 dB, which is the measured gain difference between broadside and azimuth 60° steering angles (see Table 3.2). It is worth noting that when the phased array transmits at low EIRP, the SNR at the receiver limits the link performance. So we can see a good performance at both scanning angles. Hence, the EIRP dynamic range of the phased array is approximately 31 dB and 35 dB for 60° scan angle and broadside radiation, respectively, at EVM equal to 2 %. If a higher EVM is allowed, the EIRP dynamic range increases but is limited by the maximum EIRP and the beamforming antenna gain scan loss.

Fig. 3.14 shows the EVM as a function of the scan angle for all possible combinations of measurements (except the ones employing attenuators) obtained by considering different QAM modulation orders, different IF (AWG) bandwidths of the modulated signals, and input signal voltage of the AWG as listed above. Each subplot represents the EVM as a function of the scan angle for the three IF (AWG) bandwidths, fixed modulation order, and input signal voltage of the AWG. For example, Fig. 3.14(a) shows the results for the 16−QAM and input voltage of 200 mVpp. In Fig. 3.14, the modulation order increases from the left to the right columns, while the input voltage increases from the upper to the lower rows. Trends are maintained throughout all the measurements with a couple of exceptions due to corrupted data (see Fig. 3.14(i) and (m)). As expected, increasing the bandwidth of the modulated signals increases the EVM because more noise power is contained in the generated communications link signals, as seen from each subplot (Fig. 3.14. Also, increasing the input signal voltage of the AWG, which is effectively increasing the EIRP, increases the EVM as can be seen, e.g., from Figs. 3.14(c), (g), (k) and (o) showing the EVM as a function of the scan angle for the 128−QAM modulation. Another observation is that at lower (but still high) EIRP, or as presented here, at lower input signal voltage of the AWG, the EVM does not vary too much with the scan angle. On the other hand, the EIRP increases the EVM at broadside radiation, and the maximum scan angle is higher than at intermediate scan angles; compare Figs. 3.14(c) and (o). This is explained by the fact that stable performance is expected at the linear range of the power amplifiers while, as the EIRP increases, it enters the non-linear region. Notably, the corresponding EIRP values in all the plots in Fig. 3.14 vary between 45 and 60.5 dBm, which is rather high. Finally, a stable EVM performance is observed as the modulation order increases for a fixed input voltage. Compare, e.g., Figs. 3.14(e), (f), (g), and (h) as the modulation order increases from 16−QAM to 256−QAM for a fixed input voltage of 200 mVpp.

## 3.5 Summary and Conclusions

This chapter has demonstrated the high performance of a $16 \times 16$ elements phased array at 28 GHz band for 5G applications. Both design simulations and measurement results of a manufactured prototype are presented. The fab-

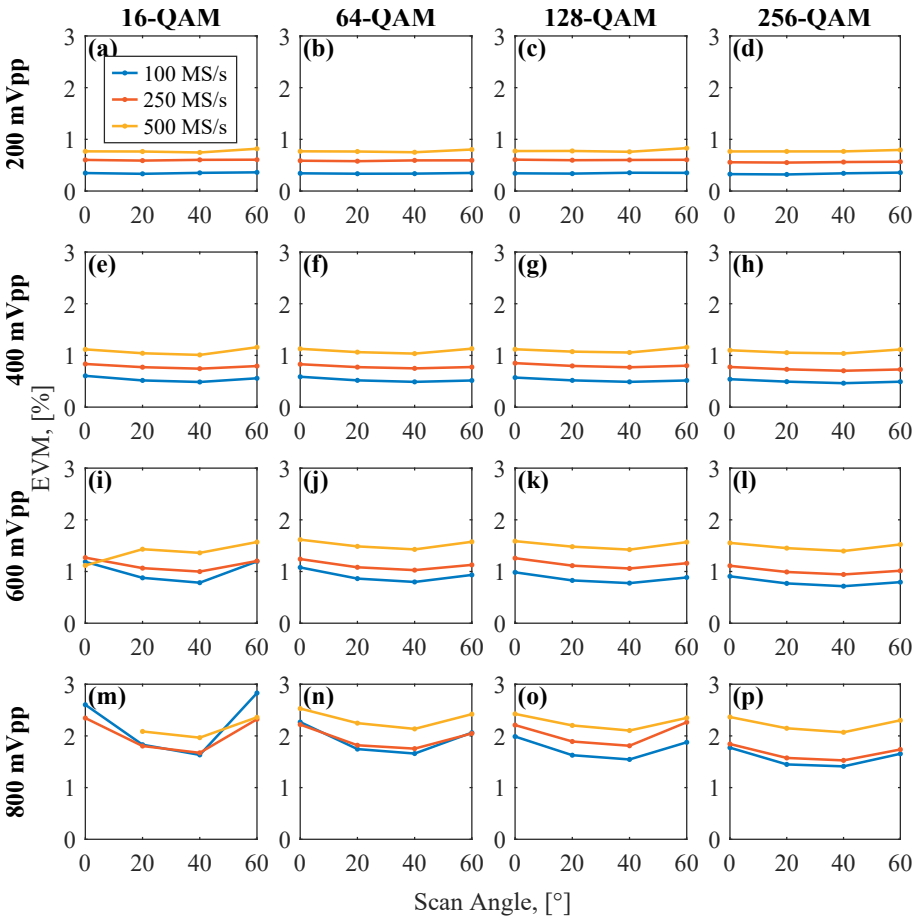


Figure 3.14: TX EVM vs. scan angle measured over-the-air at a 3 m TX-RX separation for various modulated transmissions (increasing order from left to right) and various input signal voltages of the AWG (increasing order from the top down) at three transmission rates, i.e., 100, 250, 500 MS/s.

ricated prototype fulfills the performance of the required system. The array is a complete system including up/downconverters and 1×4 TRX beamformer ICs and can steer its main beam in the range of ±60° in azimuth and ±10° in elevation. The phased array can deliver a maximum EIRP of 65.5 dBm at saturation with a 3 dB bandwidth of $26.5 - 29.5$ GHz. The proposed structure employs gapwaveguide-based antenna elements to simplify the design and reduce losses in the array front-end. Hence, the proposed phased array system design is a good candidate for a compact deployment in practical 5G systems requiring beamforming with high output power while reducing manufacturing complexity.

Based on the presented measurements and analysis we have demonstrated the excellent transmit EVM performance of a slant-polarized 28 GHz gapwaveguide-based phased array at 28 GHz. Results are based on non-standardized OTA link performance measurements for transmitting signals with various QAM modulation orders, symbol rates, and input powers. A 2.6% EVM was measured when transmitting modulated signals over a 3 Gbps link at 60.5 dB EIRP. The results show that the phased array can transmit a high data rate at a high EIRP.

The phased array is made cost-effective by using a printed circuit board (PCB) with fewer layers. The proposed design only makes use of 6 PCB layers, as opposed to the typical wideband phased arrays that have 12 layers. By separating the radiating components of the phased array from the PCB, a significant reduction in the number of layers is made possible. By using this method, the large $16 \times 16$ array configuration is supported while maintaining the wideband properties of waveguide antennas.

# Chapter 4

# Gapwaveguide-based High Power Phased Array Antenna at 28 GHz

## 4.1 Introduction

To date, several phased arrays have been proposed for 28 GHz 5G applications [13, 23, 26, 62], as mentioned before. They have been mainly implemented on CMOS and SiGe BiCMOS technologies. These solutions offer great integration flexibility of all circuit functionality, e.g., including phase shifters, variable gain amplifiers (VGA), power amplifiers (PA), and low noise amplifiers (LNA) on a chip [22]. However, the PAs based on these technologies typically deliver an output power at the 1 dB compression point (P1dB) in the range of 9.5 to 16 dBm [13, 17, 23, 25, 26, 62, 70]. This limits the maximum EIRP and therefore array antennas of 256 elements or more are needed to produce a 60 dBm EIRP [27, 33, 71], which is the required EIRP at the base stations for mobile communication systems [2].

The Gallium nitride (GaN) transistor technology can overcome output power limitations. GaN is a wide-bandgap semiconductor technology with a high inherent operating voltage. Hence, it can be used to devise PAs able to deliver high output power. The integration of GaN-based PAs and LNAs with phased array antennas has been investigated broadly [27, 72]. The P1dB output powers at the mmWave frequencies have been demonstrated to be above 25 dBm. Furthermore, GaN-based LNAs are capable of lower noise figures too, e.g., from $3-4$ dB. Therefore, GaN technology is a good semiconductor technology candidate for mmWaves phased arrays in order to achieve the required high EIRP while keeping the size of the phased array antenna smaller [19].

This chapter, in full, is a reprint material as it appears in [F]. The dissertation author was the primary investigator and author of this paper.

During conversion, a significant amount of DC power is lost as dissipated heat. Therefore, in addition to the output power, another important figure of merit for PAs is the power added efficiency (PAE), which is defined as the ratio between the output and input RF power difference to the DC power. Despite having a higher PAE than other technologies, GaN transistors only achieve about 20% [27]. Indeed, short wavelengths and the more compact antenna element spacing in mmWave pose challenges regarding the thermal management of high-power GaN PAs too. Hence, the PAE needs to be thoroughly considered at the design stage of phased arrays [71]. This has been demonstrated for a phased array with digital beamforming capabilities [71]. Heat pipes were used there to efficiently dissipate the high-density heat produced by the PAs for a large antenna comprising $15 \times 24$ radiating elements.

To the authors' best knowledge, high-EIRP phased arrays with compact form factors for 28 GHz 5G applications have not been published elsewhere. The size of the phased array is the key factor determining its total cost. Therefore, we focus on addressing the challenges of such a compact design in terms of antenna element design, beamforming, and handling the heat dissipation of the system integrated with radio frequency front-end (RFFE) transceivers based on the GaN technology.

The main contributions of this chapter are: (i) It is experimentally shown that a GaN-based analog beamforming phased array with low cost is feasible, (ii) we outline a system-performance-based design approach of compact phased arrays with analog beamforming capabilities combining various semiconductor technologies. The approach is based on power budget computations and size estimates resulting in a GaN-based high-EIRP cost-efficient phased array antenna, and (iii) we demonstrate a detailed and complete design of the optimized array antenna components including integration with transitions. Also, the experimental evaluation of the manufactured prototype of an $8 \times 8$ high-EIRP, heat-transfer-efficient, and highly compact phased array antenna system delivering 61 dBm maximum measured EIRP while consuming 42 W DC power is presented. Beam steering within $\pm 60°$ in the $E$-plane is demonstrated.

## 4.2 Phased Array Design

### 4.2.1 Power Budget Considerations

The trade-off among various parameters must be considered to design a cost-effective high-EIRP phased array at 28 GHz. In this section, we present our approach for determining the number and performance of various devices integrated into phased arrays, as well as their impact on the final design. The goals are threefold: (i) high EIRP, (ii) efficient heat dissipation, and (iii) low cost. The latter is proportional to the total number of antenna elements, the number of associated RFFEs, and the semiconductor die size [27]. The low number of components simplifies manufacturing of the phased array system, lowering overall production costs. Semiconductor chipsets are the most expen-

sive component of phased array systems, and their cost is proportional to the total die size. PAs are one of the most important RF chipsets in phased arrays, which, in addition to delivering high power, require efficient heat dissipation to ensure stable operation and avoid failure.

Hence, the power budgets for various semiconductor technologies and their potential mix thereof must be compared. Table 4.1 shows a summary of various parameter designs of active components currently available for mmWave phased array antennas. Here, we estimate the output power and size of a phased array using several PA technologies to achieve a maximum EIRP of 60 dBm considering the following power budget

$$\text{EIRP} = G_A + OP_{Tot} - L_F, \tag{4.1}$$

where

$$G_A = G_{SA} + 10\log N_{FE}, \tag{4.2}$$

is the total antenna gain in dBi, and

$$OP_{Tot} = OP_{PA} + 10\log N_{FE}, \tag{4.3}$$

is the total conductive power given in dBm, $L_F$ is the feeding loss in dB, $G_{SA}$ is the subarray antenna gain, and $OP_{PA}$ is the PA output power. $N_{FE}$ denotes the number of subarrays or RFFEs. In this work, a "subarray" is defined as a group of antenna units with a linear inter-element spacing of $0.56\lambda$, where $\lambda$ is the free space wavelength at 29.5 GHz. The subarray antenna gain in dBi is given by

$$G_{SA} = G_p + 10\log N_p, \tag{4.4}$$

where $N_p$ is the subarray size, and $G_p = 6$ dBi is the gain of the antenna unit. In linear scale the antenna gain is computed by the well-known formula $G_p\,[linear] = 4\pi A_e/\lambda^2$, which is directly proportional to the effective aperture size $A_e = (0.56\lambda)^2$ of the antenna element. The array spacing ensures a $\pm 60°$ beam scanning without grating lobes [73]. The EIRP and the PA output power are computed for the PA's P1dB and 9 dB backoff (9 dB BO) from P1dB points. The mmWave wireless communication links use modulation schemes with a large dynamic range, such as high-order QAMs and OFDM. This BO ensures that the PA amplifies signals in its linear range without distorting the modulated signal [74].

The radiated power depends on the output power of the PA, which in turn is a function of the DC power consumption and the PAE. Both are important design factors for the phased array's heat dissipation mechanism. Assuming that the PA has a sufficiently high gain, the DC power consumed can be computed in Watts (W) as follows

$$P_{DC} = \left(OP_{PA} - IP_{PA}\right)/PAE \simeq OP_{PA}/PAE, \tag{4.5}$$

where $OP_{PA}$ and $IP_{PA}$ are the PA output and input power, respectively.

Table 4.1: 60 dBm EIRP solution comparison

| | Case | | 1 | 2 | 3 | 4 | 5 |
|---|---|---|---|---|---|---|---|
| | PA technology | | CMOS | SiGe | SiGe | GaN | GaN |
| Antenna array | $N_p$ | | 1 | 1 | 4 | 4 | 8 |
| | Az. Scan [°] | | ±60 | ±60 | ±60 | ±60 | ±60 |
| | El. Scan [°] | | ±60 | ±60 | ±10 | ±10 | - |
| | $G_{SA}$ [dBi] | | 6 | 6 | 12 | 12 | 15 |
| | $G_A$ [dBi] | | 28.8 | 25.8 | 28.8 | 22.8 | 24.1 |
| | $L_F$ [dB] | | 1 | 1 | 1 | 1 | 1 |
| RF Power | $OP_{PA}$* [dBm] | P1dB | 9.5 | 16 | 16 | 28 | 28 |
| | | 9 dB BO | 0.5 | 7 | 7 | 19 | 19 |
| | $OP_{Tot}$ [dBm] | P1dB | 32.3 | 35.8 | 32.8 | 38.8 | 37 |
| | | 9 dB BO | 23.3 | 26.8 | 23.8 | 29.8 | 28 |
| | EIRP [dBm] | P1dB | 60.1 | 60.6 | 60.6 | 60.6 | 60.1 |
| | | 9 dB BO | 51.1 | 51.6 | 51.6 | 51.6 | 51.1 |
| Size | $N_{FE}$ | | 192 | 96 | 48 | 12 | 8 |
| | Total die size* [mm$^2$] | | 173 | 271 | 136 | 229† | 153† |
| | Array size $A_{array}$[cm$^2$] | | 69 | 35 | 69 | 17.3 | 23 |
| DC Power | PA PAE* (9 dB BO) | | 3% | 3% | 3% | 7% | 7% |
| | $P_{DC}$ / PA (9 dB BO) [W] | | 0.04 | 0.17 | 0.17 | $1.13 + 0.17$† | $1.13 + 0.17$† |
| | Total $P_{DC}$ (9 dB BO) [W] | | 7.2 | 16 | 8 | 15.6 | 10.4 |
| | Power density $\eta_{\text{diss}}$ [W/cm$^2$] | | 0.1 | 0.46 | 0.12 | 0.9 | 0.45 |

* Values are taken from [23, 70, 75]

† In these cases, each RF chain is assumed to have both SiGe and GaN PAs.

In order to relate the consumed power to the size of the array antenna, let's define the power density as

$$\eta_{\text{diss}} = OP_{Tot}/A_{\text{array}}, \tag{4.6}$$

where the approximate array area can be computed as $A_{\text{array}} \approx N_p N_{FE}(0.56\lambda)^2$, with parameters defined above. $\eta_{\text{diss}}$ is measured in Watts per squared centimeters (W/cm$^2$). Hence, the power density may be used to evaluate the efficiency of the heat handling mechanism for systems with the same EIRP.

Next, we perform a comparative analysis by computing the aforementioned parameters for different potential design configurations employing different semiconductor technologies and their mix. We consider five different cases whose results are summarized in Table 4.1. Cases 1, 2, and 3 consider CMOS and SiGe PAs because they offer great flexibility. Here, we put emphasis on achieving maximum beam scanning range, low $P_{DC}$, or both. However, the use of GaN PAs, considered in Cases 4 and 5, results in compact phased arrays employing fewer RFFEs. The primary use of the GaN technology for mmWaves phased array antennas is in the realization of PAs and LNAs. Meanwhile, other functional blocks such as phase shifters and variable gain amplifiers can be equally realized on CMOS and SiGe BiCMOS technologies. Therefore, a hybrid module combining CMOS or SiGe beamformers and GaN-based RFFEs is an excellent solution for meeting both the high output power and the low-cost requirements in the design of 5G phased array antennas, which is considered in cases 4 and 5.

Cases 1 and 2 in Table 4.1 illustrate the power budget of phased arrays with subarray size $N_p = 1$, employing CMOS and SiGe PAs, respectively. Given $G_{SA}$, $OP_{PA}$ and $L_F$, the number of front-ends $N_{FE}$ is computed from (4.1) in order to achieve EIRPs equal to 60 dBm and 51 dBm, at P1dB and at 9 dB BO, respectively. The computed EIRP has been slightly increased to obtain realistic array sizes. It is worthwhile to note that due to subarray size $N_p = 1$, both cases 1 and 2 are able to cover the full $\pm 60°$ scanning range in both azimuth and elevation planes. The total $P_{DC}$ of each case is the sum of the consumed DC power of all PAs. Therefore, cases 1 and 2 with about 3% PAE at 9 dB BO will consume 7.2 and 16 W, respectively. The average power densities $\eta_{\text{diss}}$ for Cases 1 and 2 are 0.1 and 0.46 W/cm$^2$, respectively. Hence, by considering equal PAE for both cases, SiGe will produce more heat. Meanwhile, $N_{FE}$ is reduced by half for Case 2 resulting in fewer RF components needed.

Case 3 shows the power budget of a phased array employing a SiGe-based PA with a subarray size of $N_p = 4$ elements in the azimuth direction. Comparing cases 2 and 3 can give an indication of the advantages and disadvantages of subarrays. While DC power consumption $OP_{Tot}$ and the number of subarrays $N_{FE}$ is decreased to half due to subarray, the total size of the array is doubled. In other words, for a fixed EIRP, the subarray increases the array gain $G_A$, while decreasing $OP_{Tot}$. Therefore, the power density is decreased in Case 3, which requires a simpler heat dissipation solution. It is worthwhile

to note that employing a subarray size of 4 elements in the vertical direction, the elevation scanning range becomes limited to $\pm 10^{\circ}$, as the closest spacing of the subarray elements is at least $2.2\lambda$. Although, in this case, subarraying reduces the steering capability, some deployment scenarios, e.g., indoor, low-rise urban, suburban, and rural environments, have limited user spread in the vertical direction, therefore a reduced scanning range is still acceptable [58].

Cases 4 and 5 represent GaN-based solutions with a high OP1dB PA power output and subarray sizes with 4 and 8 elements, in the elevation direction. The PA's high output power aids in shrinking the array's size, even when radiating elements are subarrays. $N_{FE}$ is decreased significantly in both cases. Currently, there are no off-the-shelf GaN-based beamformer integrated circuits (BFICs). Hence, a SiGe-based BFIC is added to the beamforming power budget calculation. To maintain the steering capability of $\pm 60^{\circ}$ in one plane, subarraying is required in the other plane because the spacing between RFFEs in the steering plane should not exceed the limit $0.56\lambda$. Although the elevation plane scanning range in Case 5 is negligible due to the larger subarray size, the DC power density is half that of Case 4. Case 5 uses 153 $mm^2$ total die area size to produce 37 dBm $OP_{Tot}$ at P1dB.

Research on GaN PAs at the mmWaves has been mostly restricted to developing their functional characteristics, such as gain, output power, efficiency, etc. This research examines their application to deliver high power in the context of analog beamforming phased array antennas. The remainder of this section will be devoted to the design of a phased array satisfying the requirements of the power budget computations listed in Case 5.

### 4.2.2 Front-end Design

Fig. 4.1 shows that four dual-channel commercialized RFFEs and two commercialized BFICs are used in the PCB design. The RFFEs are based on 150 nm GaN on the SiC process from Qorvo. This device operates from $26 - 30$ GHz and contains an LNA, a transmit/receive switch and a PA. The receive path including the LNA plus switch provides 17 dB of gain and a typical noise figure of 3.5 dB. The transmit path including the PA plus switch, provides 27 dB of small-signal gain with high linearity at $OP_{PA} = 22$ dBm average output power while supporting peak power of 31 dBm and P1dB of 28 dBm [76]. Each BFIC has four bidirectional channels and each channel has a transmit and a receive chain. These contain a high-resolution phase shifter and VGA to perform analog beamforming. The VGA gain control in the TX and RX chains supporting a maximum of 25 dB and 30.5 dB, respectively [66]. Each transmitter channel chain P1dB is 19 dBm. The use of two stages of amplifiers helps to have high output power in receive mode and a good margin for the input signal level in transmit mode.

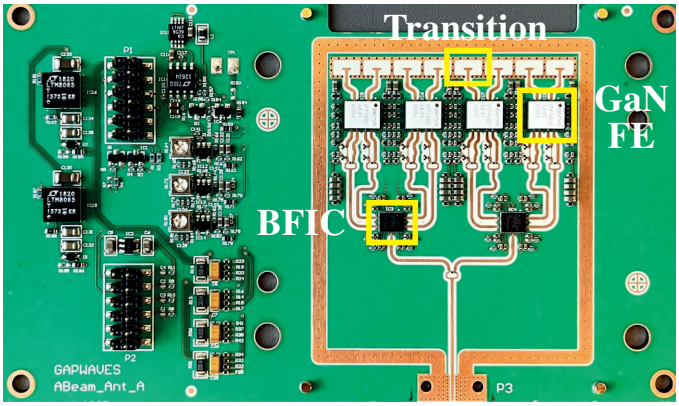


Figure 4.1: Photograph of PCB employing four dual-channel GaN RFFEs, which are connected to 8 antenna feeds.

### 4.2.3 Antenna Element and Transition Design

Gapwaveguide (GW) technology is a low-loss waveguide and packaging technology at mmWaves that also offers good thermal conductivity performance [77,78] and can be fully metallic. Therefore, GW technology is a good candidate for phased arrays with high power dissipation and compact size [19]. A center-fed vertical subarray of 8 vertical slots is used as the antenna element, as shown in Fig. 4.2(a). The design parameters are provided in Table 4.2 expressed in $\lambda_0$, i.e., the free space wavelength at 28 GHz. To excite the slots, two symmetric ridge GW lines are used; a sketch of the lines unit cell is shown in Fig. 4.2(b). The ridge and pin sizes are designed to cover the target frequency band, following the design rules in [77]. The slot array is fed by the GW lines from the center of the subarray. The slots are identical in design, and Fig. 4.2(c) depicts the layout of the two slots and their relative positions. The relative vertical distance between all slots and the horizontal offset from the middle of the subarray are identical. The width and height of the subarray are $0.52\lambda_0$ and $4.7\lambda_0$, respectively. A ridge GW line connects the transition to the feeding point of the subarray at its center. As illustrated in Fig. 4.2(d), a dual ridge waveguide connects this ridge GW line to the two GW lines used to feed the slots.

In order to maximize the power transfer to the radiating element from the GaN-based RFFE, a through-substrate probe transition from microstrip to ridge GW has been used. The vertical, compact, and contactless transition is a practical solution for phased arrays as it leaves space below the antenna for PCB routing and active components, as pointed out in Section 2.3. The layout of the microstrip probe is shown in Fig. 4.2(e). Fig. 4.2(f) depicts a cross-section of the transition. To provide a back short, a pin bed is placed over the microstrip probe. The designed transition simulation and measurement

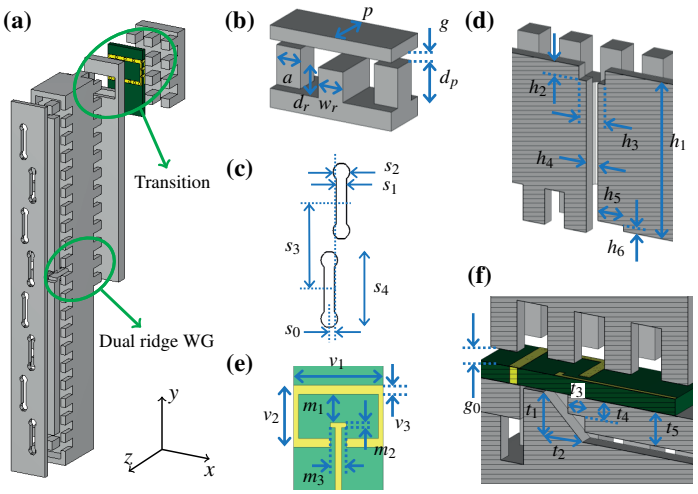


Figure 4.2: (a) Exploded view of the design sketch of subarray integrated with the transition. (b) Ridge GW unit cell, where a ridge is embedded within a pin texture. (c) The layout of two slots of slot layer. The rest of the slots are similar. (d) $yz$-plane cross-section sketch of the dual ridge waveguide. (e) The layout of the microstrip probe is used in the transition. (f) $yz$-plane cross-section of microstrip line to ridge GW line transition.

Table 4.2: Antenna structure key dimensions expressed in $\lambda_0$ at 28 GHz

| *Par.* | *Val.* | *Par.* | *Val.* | *Par.* | *Val.* | *Par.* | *Val.* | *Par.* | *Val.* |
|---|---|---|---|---|---|---|---|---|---|
| $a$ | 0.13 | $s_0$ | 0.04 | $v_1$ | 0.52 | $h_1$ | 0.84 | $t_1$ | 0.19 |
| $p$ | 0.25 | $s_1$ | 0.07 | $v_2$ | 0.35 | $h_2$ | 0.07 | $t_2$ | 0.19 |
| $g$ | 0.005 | $s_2$ | 0.11 | $v_3$ | 0.05 | $h_3$ | 0.15 | $t_3$ | 0.08 |
| $d_r$ | 0.15 | $s_3$ | 0.6 | $m_1$ | 0.16 | $h_4$ | 0.06 | $t_4$ | 0.08 |
| $w_r$ | 0.13 | $s_4$ | 0.5 | $m_2$ | 0.03 | $h_5$ | 0.15 | $t_5$ | 0.15 |
| $d_p$ | 0.2 | | | $m_3$ | 0.09 | $h_6$ | 0.03 | $g_0$ | 0.06 |

results with a two-layer, 10-mil Rogers RO4350 substrate are reported in [19]. The presented results show a 0.2 dB insertion loss and $-20$ dB input matching ($|S_{11}|$) from $26.5 - 29.5$ GHz.

The subarray integrated with the transition is simulated with CST Microwave Studio's time domain solver. The embedded input matching of half of the elements is shown in Fig. 4.3(a); the bandwidth at $|S_{11}| < -10$ dB is from $26.5 - 29.5$ GHz. The embedded mutual coupling between adjacent and every other element is under $-16$ dB as shown in Fig. 4.3(b). The embedded radiation pattern of the center subarray is shown in Fig. 4.4. The average of the embedded realized gains, computed over all subarrays, increases from 13.8

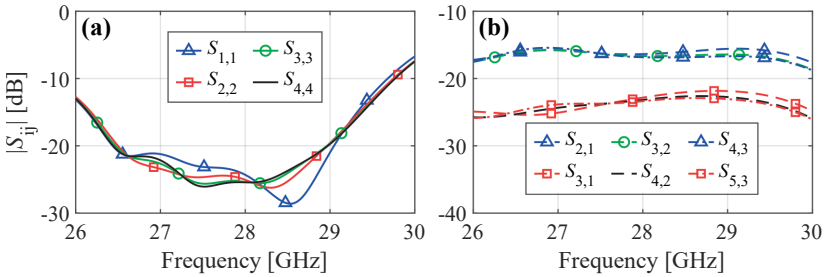


Figure 4.3: Embedded element simulation results for (a) reflection coefficient and (b) mutual coupling.

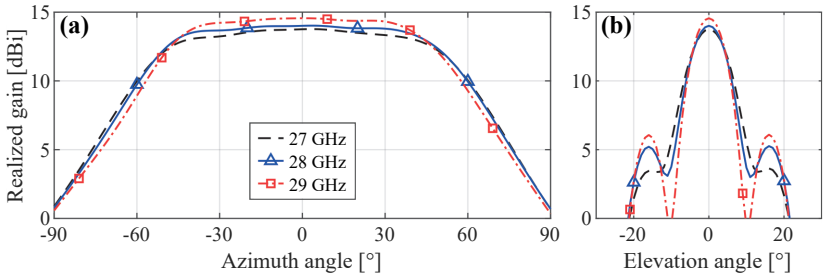


Figure 4.4: Embedded radiation pattern of the central subarray in (a) azimuth ($E$-plane) and (b) elevation ($H$-plane).

to 15 dBi across the operating frequencies. This is expected because the size of the aperture in terms of wavelength increases with frequency. This is in line with the design goal set in Table 4.1, where the subarray gain and the feeding loss were considered to be equal to 15 and 1 dB, respectively. The radiation pattern is narrow in the elevation plane (H-plane) due to subarraying, while a wide beamwidth in azimuth (E-plane) is achieved. The realized gain variation within $\pm 60°$ has a minimum and maximum of 3.5 and 6 dB, respectively. The gain variation is the largest at 29.5 GHz. This can be attributed to a slight directivity increase at higher frequencies. The cross-polarization ratio is lower than $-35$ dB in the azimuth plane.

## 4.3 Calibration and Measurements

Fig. 4.5 shows the manufactured prototype of the designed phased array antenna. The structure consists of five layers, where all the metal layers have been manufactured by aluminum milling. The PCB is placed between the shield layer and the cooling layer, which is an efficient way to stabilize the temperature of RF active components on the PCB. This solution was proposed in [19, 20]. In this arrangement, the GaN components dissipate heat directly

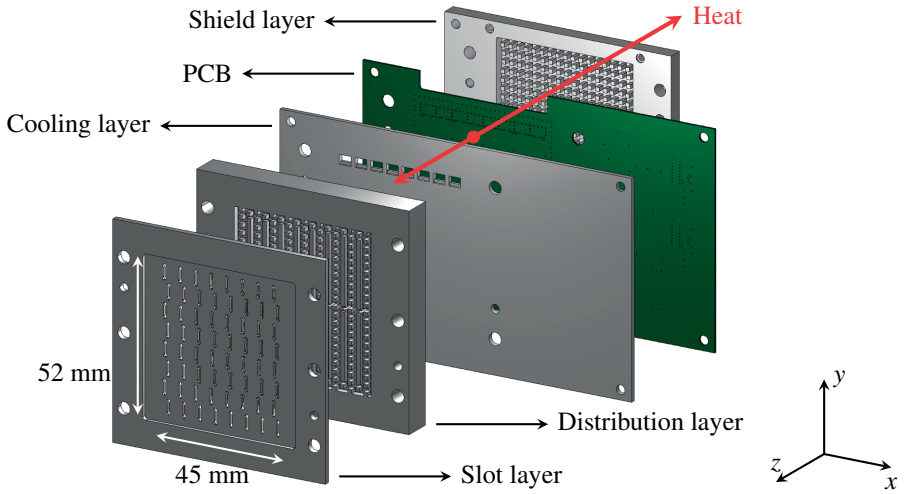


Figure 4.5: Exploded view of the phased array antenna's stack-up.

into the shield layer, and through PCB to the cooling layer. The shield layer has a bed of pins used for transition back-short, and also to suppress unwanted cavity modes. The cooling layer contains the openings for microstrip transition, and also acts as a conductive plane over the ridge gapwaveguide.

The phased array is characterized and calibrated in transmit mode. All measurements were performed in the farfield using a vector network analyzer and a standard gain horn antenna. To achieve the intended performance, the active phased arrays were calibrated by adjusting the relative phase between channels. Although the design is symmetrical in all parts, there will be an unavoidable difference between channels due to, e.g., edge effects, manufacturing, assembly, and component differences, particularly due to varying BFICs' performance. Inconsistency in the phases of a phased array channels results in beams with lower gain and higher side lobe levels [A]. The channel phase calibration follows the method in [67]; details are omitted here for the sake of compactness. This process offers the minimum requirement for the hardware, has a simple process, and best suits arrays with a small number of elements [79]. The symmetry in the design and low $N_{FE}$ allowed a simplification of the calibration procedure and reduced calibration measurement time. The calibration was performed only at the broadside at 28 GHz and applied to all frequencies and steering angles. The results presented in the following are calibrated. Radiation pattern measurements were calibrated under similar conditions to ensure comparison consistency. Despite considering all the systematic error sources into account, the measurement results are predicted to have uncertainties. This may result from antenna angular misalignment, IC temperature drift, and measurement equipment noise. GaN IC's transmit path gain can change by 5 dB in the range from $25 - 95°$C [75].

Fig. 4.6 shows the measured normalized radiation pattern in the azimuth plane at 28 GHz only (center frequency of the band). The main beam was measured at steering angles $-30°$, $0°$, and $30°$ as shown in Fig. 4.6 (a), (b), and (c), respectively. The measured side lobe levels are $< -10$ dB for all radiation patterns, and the 3-dB beamwidth equals $12°$ and $14°$ in the broadside and the $\pm 30°$ directions, respectively. As can be seen from Fig. 4.6, the measurement results agree well with the simulations. The calibrated measurement EIRP beam patterns at three different frequencies are shown in Fig. 4.7. The phased array beams span a field-of-view within the $\pm 60°$ range in the azimuth plane ($E$-plane). This is in line with the value specified in Table 4.1. As can be seen from Fig. 4.7, the EIRP increases with frequency, because the antenna gain of the sub-array element increases with frequency. Meanwhile, the PA's gain decreases slightly with frequency, but the antenna gain increase dominates. The maximum EIRP of far steering angles is lower than in the broadside because the effective aperture area is reduced when the phased array scans away from the broadside, as expected. See, e.g., the embedded radiation pattern of the center subarray, Fig. 4.4(a).

The EIRP and the total transmit gain (defined as the ratio between EIRP and input RF power) in the broadside direction v.s. input RF power, are both shown at three frequencies in Fig. 4.8. The EIRP at P1dB is equal to 57, 57.5 and 60 dBm at 27, 28, and 29 GHz, respectively. The maximum measured EIRP at these frequencies is 59.5, 61, and 62.5 dBm, respectively. In comparison to the values provided in Case 5 of Table 4.1, the design achieves its EIRP goal at 29 GHz. This difference can have multiple sources, e.g., the differences between the PAs' performance, the PAs going into compression at lower input power, and higher loss in the feeding lines, transitions, and antenna elements. The directions of maximum EIRP of the scanned beams in the $E$-plane are shown in Fig. 4.9. The 21 beams were measured over the whole operating frequency band employing the phased array calibration at the broadside at 28 GHz. The beams cover $\pm 60°$ angular range at 28 GHz. However, the range is larger at lower frequencies and smaller at higher frequencies because of the beam squint effect while steering the beams over a wide frequency band [73].

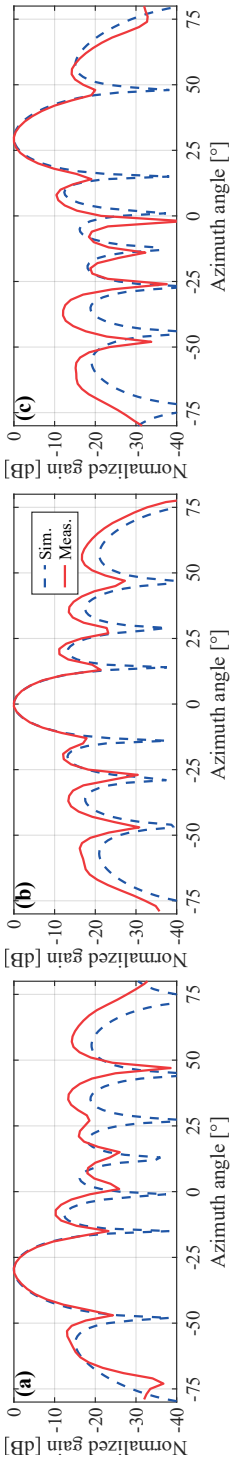


Figure 4.6: Measured patterns in azimuth plane ($E$-plane) at (a) $-30°$, (b) $0°$, and (c) $30°$. All patterns are normalized to their maximum value.

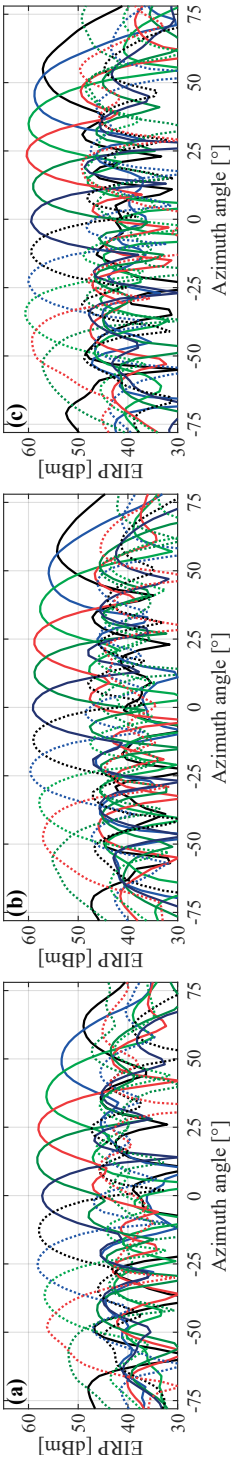


Figure 4.7: Measured beams in terms of EIRP with $-3$ dBm input power, in azimuth plane at (a) 27, (b) 28, and (c) 29 GHz.

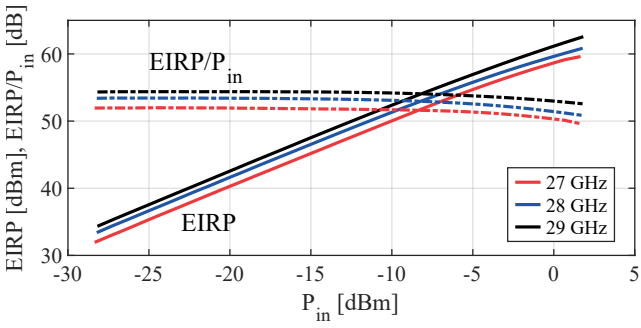


Figure 4.8: Measurements of EIRP and total transmit gain ($EIRP/P_{in}$) at broadside angle beam vs. RF input power at three frequencies.

The measured temperatures of BFIC and the case of the antenna versus RF input power are shown in Fig. 4.10(a). In the proposed structure, the all-metal antenna assembly also functions as a double-sided heat sink, dissipating heat from components on both the top and bottom, as shown in Fig. 4.5 by the red arrow. The shield layer is equipped with a fan and a heat sink, which is intended to provide additional temperature stability during all the measurements. The steady-state case temperature was read both in front and back of the phased array, as shown in Fig. 4.10(b). The GaN-based RFFE and SiGe-based BFIC have a maximum operating temperature of about 110°C. The figure shows that the phased array can support high power while having a temperature that all circuitry can handle. The BFIC only reaches a maximum temperature of 92°C at the highest power performance. Maximum temperature changes for the case are 8°C and for the BFICs are 13°C (from 79 to 92°C). Therefore for the proposed design, the traditional heat dissipation mechanism is enough, compared to the design described in [71], in which heat pipes with very high thermal conductivity are used for heat transmission. Because GaN-based RFFE has no integrated thermometer, its temperature cannot be measured directly. Fig. 4.10(a) also displays the phased array's total DC power consumption. It represents the total power consumed by the PA and other components. The system as a whole consumes approximately 42 W of DC power at P1dB and 30 W at 9 dB BO. According to the estimates presented in Table 4.1, the PAs deliver 10.4 W at 9 dB BO. The differences between measurements and estimations have mainly two sources. Firstly, measurements comprise the whole phased array system, including PAs. Secondly, the practical PAE might be lower than what has been assumed in Table 4.1.

Table 4.3 summarizes the performance of the phased array antenna system presented here and compares it with state-of-the-art high EIRP phased arrays at 28 GHz. Compared with published $8 \times 8$ arrays, the proposed design shows higher EIRP while using fewer active components. Achieving higher EIRP is equivalent to higher power consumption.

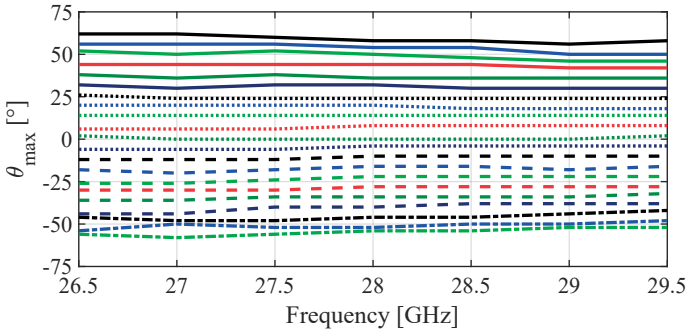


Figure 4.9: Measured direction of maximum EIRP ($\theta_{\max}$) of the beams in $E$-plane.

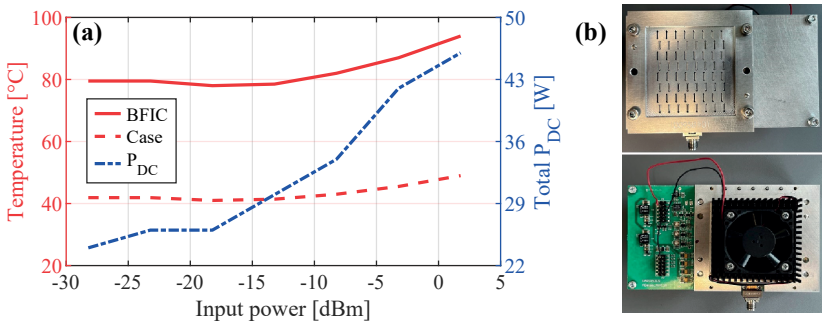


Figure 4.10: (a) Temperature readout of the BFIC and the phased array's case, and total DC power consumption versus RF input power in TX mode. (b) Front and back view of the manufactured phased array prototype.

## 4.4 Summary and Conclusions

The design and experimental verification of the performance of a compact high-EIRP phased array based on GaN high-power amplifiers and gapwaveguide antenna technology are demonstrated. The horizontal-polarized phased array antenna can deliver 60.5 dBm EIRP at the saturation regime. It covers a scanning range of $\pm 60°$ in the azimuth plane and supports the frequency range from $26.5 - 29.5$ GHz. The use of a fully metallic antenna structure helps stabilize the antenna temperature due to an efficient heat power dissipation mechanism while delivering high EIRP with a relatively small array size of $8 \times 8$ elements compared to previous designs. A potential application of the proposed design is as a highly efficient and low-cost base station antenna system for 5G wireless communications.

Table 4.3: Comparison with state-of-the-art phased arrays at 28 GHz

| Ref. | **This work** | [80] | [19] | [71] |
|---|---|---|---|---|
| PA Tech. | **150nm GaN** | SiGe BiCMOS | SiGe BiCMOS | 150nm GaN |
| Ant. Tech. | **Gapwaveguide** | Stacked patch | Gapwaveguide | n/a |
| $OP_{PA}$ $P_{sat}$ [dBm] | **31** | - | 17 | 33 |
| $OP_{PA}$ P1dB [dBm] | **28** | 16 | - | - |
| Beamfoming Architecture | **Analog** | Analog | Analog | Digital |
| Array Size | $\mathbf{8 \times 8}$ | $8 \times 8$ | $8 \times 8$ | $15 \times 24$ |
| Subarray Size | **8** | 1 | 4 | 15 |
| $N_{FE}$ | **8** | 64 | 16 | 24 |
| EIRP [dBm] | **58*** | 55* | 51** | 75 |
| Scan Range (Az./El.) [°] | $\pm\mathbf{60}/-$ | $\pm 50/\pm 40$ | $\pm 45/\pm 10$ | $\pm 60/-$ |
| Tx Total $P_{DC}$ [W] | **42*** | 21.8* | 13*** | n/a |
| Tx Total $P_{DC}$ / $N_{FE}$ [W] | **5.25*** | 0.34* | 0.812*** | n/a |

*At P1dB. **At Psat. ***At 8 dB BO.

# Chapter 5

# Performance Analysis of mmWave 5G Analog Beamforming Phased Array Antennas in Indoor Environments - Collocated vs. Distributed Deployment

## 5.1 Introduction

5G millimeter-wave (mmWave) technology is gaining significant interest, not only from researchers in academia but also from the telecom industry [81, 82]. The mmWave 5G services are ideal for supporting outdoor hotspots in cities as well as indoors or anywhere more capacity is required [83]. The massive multiple-input multiple-output (MIMO) technology is a key enabler of 5G wireless systems. It employs array antennas with a large number of antenna elements at the base station, which serve many users simultaneously. Massive MIMO employs beamforming and spatial division multiplexing techniques to achieve high signal-to-interference-plus-noise ratio (SINR) and throughput. Moreover, multi-user beamforming allows for high user signal amplification and high spatial resolution, increasing the spectral efficiency by an order of magnitude [84, 85].

In order to achieve very high data rates in the mmWave frequencies with massive MIMO, blockage and propagation path loss that are more severe in

This chapter, in full, is a reprint material as it appears in [G]. The dissertation author was the primary investigator and author of this paper.

comparison with sub-6 GHz bands need to be overcome [86]. For example, many objects, including the human body, may entirely block the transmitted signal. This renders the communication link between the base station and the user unreliable [87]. For collocated array antennas, the communications link can be improved by exploiting the reflections of the transmitted signals by means of beamforming. Another strategy to overcome the blockage is to deploy antennas distributed over the desired coverage area, known as "distributed massive MIMO" [88]. While it may increase the cost of the system in the short term, it provides a more reliable link between a set of base station antennas and users, covers wider areas, improves spectral and energy efficiency, and increases average cell throughput [89–91].

Cooperative distributed antenna systems have drawn attention in order to increase the throughput of mobile communication systems [92]. The conceptual design of cooperative cellular distributed antenna systems is presented in [93], which relies on independently distributed fading channels that are more likely to be generated than with collocated antenna systems. Closed-form formulas for available data rate and multiplexing gain of mmWave massive MIMO with the distributed structure were derived in [94]. [95] extensively studies various configurations of distributing antennas for downlink mmWave transmission in Rician channels. At mmWaves, the comparison between collocated and distributed deployment has merely been made using generic channel models and ideal omnidirectional or theoretical antenna elements in the considered array antenna systems, while multiple experiments have been reported at a variety of sub-6 GHz bands [96–99]. The results suggest that distributed antenna systems improve spectral efficiency and coverage in indoor offices and industrial environments.

Research on distributed massive MIMO, including wireless power transfer, faces challenges such as frequency synchronization, channel and hardware impairments, and optimizing access point placement [100–102]. These challenges involve ensuring coherent power transfer, mitigating hardware limitations, and reducing transmit power through strategic access point positioning. Overcoming these hurdles is crucial to fully exploit the potential of distributed massive MIMO in wireless power transfer applications [103].

In addition to the examination of the advantages of collocated vs. distributed massive MIMO indoor deployment, another question of high relevance is the complexity of the massive MIMO transceivers. On the one hand, conventional fully digital high-performance beamforming networks use a full-digital chain from baseband up to the RF front end per antenna element. This renders them costly and, hence, impractical for the time being. On the other hand, hybrid beamforming combines baseband digital beamforming with analog phased array antennas (PAAs), which have a network of phase shifters in the RF domain. The deployment of PAAs and their characteristics have a considerable impact on system performance and need to be studied. To the best of the authors' knowledge, there is currently no published research work that has investigated the use of realistic PAA systems in collocated and distributed

deployment at mmWaves for various indoor environments.

Therefore, we aim to narrow the aforementioned gaps in this chapter. The main contributions are listed below.

- We thoroughly investigate the downlink performance of collocated vs. distributed mmWave indoor communication systems employing various state-of-the-art mmWave PAAs, presented in Chapters 3 and 4, with the help of various realistic indoor propagation channel models. The channel models are generated using the QuaDRiGa (QUAsi Deterministic RadIo channel GenerAtor) software [104, 105], where the indoor office channel models are based upon the 3GPP 38.901 technical report [106].

- We show that the distributed antenna system has superior performance compared to the collocated one in almost all cases. This advantage is true for all types of propagation channels, precoding schemes, and PAA beam arrangements.

## 5.2 System Model and Figures of Merit

In this section, we describe the system model and several relevant figures of merit that we aim to apply to evaluate the performance of two state-of-the-art antenna systems. Here we focus on the SINR, the gain of the RF power amplifier (PA), which is denoted by $G_{RF}$, and the achievable sum rate capacity, denoted by SR.

### 5.2.1 System Model

In order to evaluate the performance of the PAA systems, we consider the downlink of a single-cell narrowband hybrid multi-user MIMO (MU-MIMO) system shown in Fig. 5.1. We assume that each base station equipped with $M$ analog beamforming PAA is serving $K \leq M$ users, each equipped with a single antenna, which we denote as user equipment (UE). An analog beamforming network, a PA, a mixer, and a digital-to-analog converter (DAC) are the main components of a PAA. Fig. 5.1 shows a schematic of $M$ analog beamforming networks, each of which consists of a planar array antenna with $N_{az} \times N_{el}$ elements and a total antenna gain of $G_A$ in the broadside (BS) direction. The main beam is directed using phase shifters, which are connected to each antenna element in the array. Each PAA selects one beam at a time to transmit information. All of the PAAs are connected to a centralized processing unit that handles the precoding scheme and selects the beams of the PAAs according to a beam selection algorithm (see Section 5.3.3). We further assume perfect channel state information (CSI) both at the transmitter and receiver.

Based on Fig. 5.1, we define the input-output relationship to be given by

$$\mathbf{y} = \mathbf{H}\mathbf{s} + \mathbf{n}, \tag{5.1}$$

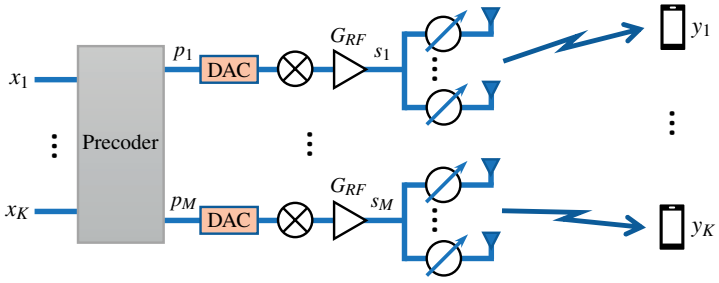


Figure 5.1: System model for hybrid MU-MIMO communication. The precoder functions as a digital beamformer at the baseband and the RF chain together with phase shifters acts as an analog beamformer at the mmWave band.

where $\mathbf{y} \in \mathbb{C}^{K\times 1}$ is a vector comprising the received signal at each UE receiver, $\mathbf{H} \in \mathbb{C}^{K\times M}$ is the downlink MU-MIMO channel matrix, $\mathbf{s} \in \mathbb{C}^{M\times 1}$ is the transmit signal vector after passing the PAs, and $\mathbf{n} \in \mathbb{C}^{K\times 1}$ is the Additive White Gaussian Noise (AWGN) vector at each UE receiver with zero means and $\sigma_n$ standard deviation.

Let $\mathbf{x} \in \mathbb{C}^{K\times 1}$ be the transmit signal vector intended for the $K$ UEs. The transmit signals are uncorrelated $\mathrm{E}\{x_k x_{k'}^*\} = 0$, for $k \neq k'$, and satisfy the power normalization $\mathrm{E}\left\{|x_k|^2\right\} = 1$. The operation $\mathrm{E}\{x\}$ denotes mathematical expectation of $x$, and $x^*$ is the complex conjugate of $x$. Hence, we can further express Eq. (5.1) as

$$\begin{aligned} \mathbf{y} &= \mathbf{H}\sqrt{G_{RF}}\mathbf{p} + \mathbf{n} && (5.2)\\ &= \mathbf{H}\sqrt{G_{RF}}\mathbf{W}\mathbf{x} + \mathbf{n}, && (5.3) \end{aligned}$$

where $\mathbf{p} \in \mathbb{C}^{M\times 1}$ is the linearly precoded transmit signal vector such that $\mathbf{p} = \mathbf{W}\mathbf{x}$. $\mathbf{W} \in \mathbb{C}^{M\times K}$ is the precoding matrix with instantaneous power normalization, $\mathrm{trace}\left(\mathbf{W}\mathbf{W}^H\right) = 1$ [107, 108] . The proportionality constant $G_{RF} \geq 0$ represents the gain of the amplifier in RF chains. We assume that $G_{RF}$ is constant across all RF chains.

Two linear precoding schemes are considered in this study: the matched-filtering (MF) precoding and the zero-forcing (ZF) precoding. The precoding matrices are given by

$$\mathbf{W} = \begin{cases} \dfrac{\mathbf{H}^\dagger}{\left\|\mathbf{H}^\dagger\right\|_F} & \text{for MF} \\ \dfrac{\mathbf{H}^\dagger\left(\mathbf{H}\mathbf{H}^\dagger\right)^{-1}}{\left\|\mathbf{H}^\dagger\left(\mathbf{H}\mathbf{H}^\dagger\right)^{-1}\right\|_F} & \text{for ZF} \end{cases}, \qquad (5.4)$$

where we have made use of the instantaneous normalization of the precoding matrix mentioned above. $\mathbf{H}^\dagger$ denotes the hermitian (complex-conjugate)

transpose operation on matrix $\mathbf{H}$, and $\|\mathbf{H}\|_F$ is the Frobenius norm of the complex matrix $\mathbf{H}$. The Frobenius norm is defined as $\|\mathbf{H}\|_F = \sqrt{\text{trace}\left(\mathbf{H}\mathbf{H}^H\right)} = \sqrt{\sum_{k=1}^{K}\sum_{m=1}^{M}|H_{k,m}|^2}$. It is worthwhile to recall that MF precoding is used to maximize the received signal power at the UE, while the ZF eliminates the interference at the UE. [108] shows that $\mathbf{W}$ is independent of $G_{RF}$.

### 5.2.2 Figures of Merit

#### Signal-to-Interference-plus-Noise Ratio – SINR

The SINR measures the desired signal quality. It is computed in terms of the received power ratios of the desired signal to the sum of interference and noise power levels. It is used to evaluate the capacity of a wireless system.

The SINR of the $k$-th UE in the downlink, which defines the $k$-th-bitstream, i.e., the $k$-th UE throughput can be computed as (see Appendix A.1 for the derivation)

$$\text{SINR}_k = \frac{S_k}{I_k + N_k}. \tag{5.5}$$

where

$$S_k = G_{RF}\left|\mathbf{H}_{k:}\mathbf{W}_{:k}\right|^2, \tag{5.6}$$

is the power of the desired received signal, where $\mathbf{H}_{k:}$ denotes the $k$-th row of the channel matrix and $\mathbf{W}_{:k}$ denotes the $k$-th column of the precoding matrix.

$$I_k = G_{RF}\sum_{k'\neq k}^{K}\left|\mathbf{H}_{k:}\mathbf{W}_{:k'}\right|^2 \tag{5.7}$$

is the power of the interfering signals, where $\mathbf{W}_{:k'}$ is the $k'-$th column of the precoding matrix, and

$$N_k = \sigma_n^2, \tag{5.8}$$

denotes the noise power at each UE receiver, which has been defined above and is assumed to be the same for all UEs. In our analysis further below, we evaluate the SINR as well as the power levels of the desired and the interference signals for a given noise power level as well as maximum transmit power limitations by an array antenna. It is worthwhile to note that the SINR depends both on the deployed antenna systems as well as on the propagation channel.

#### RF Amplifier Gains – $G_{RF}$

As mentioned above, the power amplification required in a PAA system is of great practical relevance. Therefore, we are also interested in evaluating the output power of the PAs, or more specifically, the RF amplifier gains ($G_{RF}$) (see Fig. 5.1 above and Eq. (A.6) in Appendix A.2).

Appendix A.3 shows that $\text{SINR}_k$ is an increasing function of $G_{RF}$, therefore the maximum value for $G_{RF}$ is chosen. It is chosen such that the RF chain

with the highest power of the linearly precoded transmit signal is amplified to the maximum conductive power of the PAA, i.e.

$$G_{RF} = \frac{P_{c,max}}{\max\limits_{m=1,\ldots,M} \|\mathbf{W}_{m:}\|^2}, \tag{5.9}$$

where $P_{c,max}$ is the maximum conductive power of the PAA, and $\|\mathbf{W}_{m:}\|$ is the norm of the complex vector $\mathbf{W}_{m:}$ representing the $m$-th row of the precoding matrix. Hence, $\|\mathbf{W}_{m:}\|^2$ represents the power of the linearly precoded transmit signal $p_m$, which is an element of vector $\mathbf{p}$ in Eq. (5.2) (see also Fig. 5.2).

#### Achievable Sum Rate − SR

To evaluate the expected system throughput that different PAAs can achieve in different propagation environments, the achievable sum rate capacity of the $M \times K$ MIMO can be computed [109]

$$\mathrm{SR} = \sum_{k=1}^{K} \log_2 \left(1 + \mathrm{SINR}_k\right), \tag{5.10}$$

where $\mathrm{SINR}_k$ is the SINR of the $k$-th UE computed above.

## 5.3 Propagation Channel Models and Simulation Scenarios

### 5.3.1 Channel Models

The propagation channel model is essential to system performance evaluation because the latter will depend on multiple propagation channel characteristics. As mentioned above, this chapter focuses on indoor systems. In our evaluation, we make use of well-established, standardized channel models so that the obtained results are relevant to the wireless community and can be easier to understand and compare to future works. Therefore, we consider the statistical 3GPP 38.901 channel model to emulate indoor office propagation channels for frequencies from $0.5 - 100$ GHz [106]. For the sake of completeness, we provide some of the main characteristics of this channel model below.

The path gain in line-of-sight (LOS) is

$$PG_{LOS}[\mathrm{dB}] = -32.4 - 17.3 \log_{10}(d_{3D}) - 20 \log_{10}(f_c), \tag{5.11}$$

where $d_{3D}$ is the 3D distance in meters, and $f_c$ is the frequency in Hz. The path gain model in non-line-of-sight (NLOS) is given by

$$PG_{NLOS}[\mathrm{dB}] = \min\left(PG_{LOS}[\mathrm{dB}], PG'_{NLOS}[\mathrm{dB}]\right), \tag{5.12}$$

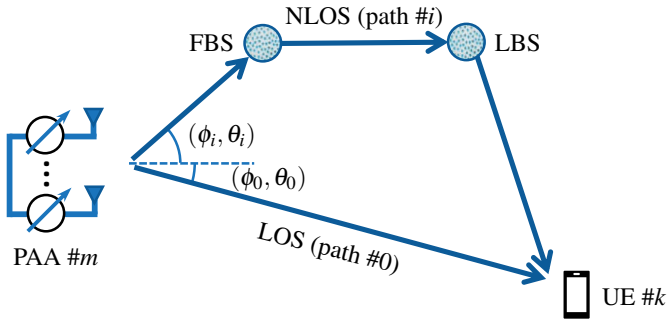


Figure 5.2: Illustration of multipath between PAA $\#m$ and UE $\#k$. FBS: first bounce scatterer. LBS: last bounce scatterer.

where

$$PG'_{NLOS}[\text{dB}] = -17.3 - 38.3\log_{10}(d_{3D}) - 24.9\log_{10}(f_c). \tag{5.13}$$

Also, the main parameters for LOS and NLOS propagation conditions at 28 GHz are presented in Table 5.1. The parameters in the table include path loss exponent (PLE), shadow fading, delay spread, the azimuth angle of arrival (AoA) spread, the elevation angle of arrival (EoA) spread, the azimuth angle of departure (AoD) spread, the elevation angle of departure (EoD) spread, K-factor, cross-polarization ratio (XPR), and the number of paths (see Fig. 5.2). In the table, $\mu$ and $\sigma$ stand for mean and standard deviation, respectively.

Fig. 5.3(a) shows the computed path gain in both LOS and NLOS propagation conditions, along with a comparison to the free space path gain. In LOS conditions according to Eq. (5.11), the PLE = 1.73 is lower than the corresponding value of PLE = 2.0 for the idealized free space propagation. On the other hand, in NLOS conditions, the path gain becomes more severe with PLE = 3.83 (Eq. (5.13)). It is expected that propagation channel characteristics will impact the performance of the evaluated antenna systems.

In order to approach our analysis in a specialized and systematic way, we consider office environments that are subdivided into two main types:

- Indoor mixed office.
- Indoor open office.

These two environments are defined in [106]. They use the 3GPP 38.901 indoor LOS and the 3GPP 38.901 indoor NLOS channels and return a LOS probability based on the 2D distance between the transmitter and the receiver. As shown in Fig. 5.3(b), in the open office, the chance of LOS propagation is higher than in the mixed office, for any given distance between the transmitter and the receiver.

Table 5.1: 3GPP 38.901 channel model parameters for indoor office at 28 GHz.

| Propagation Channel Condition | | LOS | NLOS |
|---|---|---|---|
| PLE | | 1.73 | 3.83 |
| Shadow Fading [dB] | $\sigma_{SF}$ | 3 | 8.03 |
| Delay Spread [$\log_{10}$[s]] | $\mu_{DS}$ | -7.7 | -7.6 |
| | $\sigma_{DS}$ | 0.18 | 0.2 |
| AoA Spread [$\log_{10}[^\circ]$] | $\mu_{AAS}$ | 1.6 | 1.62 |
| | $\sigma_{AAS}$ | 0.18 | 0.25 |
| EoA Spread [$\log_{10}[^\circ]$] | $\mu_{EAS}$ | 1.5 | 1.7 |
| | $\sigma_{EAS}$ | 0.3 | 0.23 |
| AoD Spread [$\log_{10}[^\circ]$] | $\mu_{ADS}$ | 0.14 | 0.11 |
| | $\sigma_{ADS}$ | 0.49 | 0.36 |
| EoD Spread [$\log_{10}[^\circ]$] | $\mu_{EDS}$ | 1.06 | 0.17 |
| | $\sigma_{EDS}$ | 0.2 | 0.61 |
| K-factor [dB] | $\mu_{KF}$ | 7 | 0 |
| | $\sigma_{KF}$ | 4 | 0 |
| XPR [dB] | $\mu_{XPR}$ | 11 | 10 |
| | $\sigma_{XPR}$ | 4 | 4 |
| Number of Paths, $I$ | | 15 | 19 |

### 5.3.2 Channel Emulation in QuaDRiGa

A structured and useful implementation of the above-mentioned channel models is available in the QuaDRiGa simulation package. QuaDRiGa can be regarded as a 3GPP 38.901 channel model reference implementation [105]. It incorporates full 3D propagation, including antenna modeling and scattering clusters as well as spherical wave propagation and spatially correlated large and small-scale fading at both the transmitter and receiver sides of the communications link, i.e., in our case, the base station and the UE, respectively.

Fig. 5.2 shows a sketch of the channel modeling approach in QuaDRiGa between a PAA and a UE. Given $M$ PAAs and $K$ UEs, the channel matrix $\widetilde{\mathbf{H}} \in \mathbb{C}^{K\times(Q_{az}\times Q_{el})\times M}$ represents the channel responses between all PAAs beams and UEs. Each PAA has $Q_{az} \times Q_{el}$ beams within its scanning range, where $Q_{az}$ and $Q_{el}$ are the number of beams in the azimuth and elevation planes, respectively. One beam per PAA will be chosen based on its ability to maximize SR (see Section 5.3.3 for the beam selection algorithm), and $\mathbf{H}$ will be generated from these beams using the details described below. The $(k, q, m)$ entry of $\widetilde{\mathbf{H}}$ representing the multipath channel impulse response between the $q$-th beam of

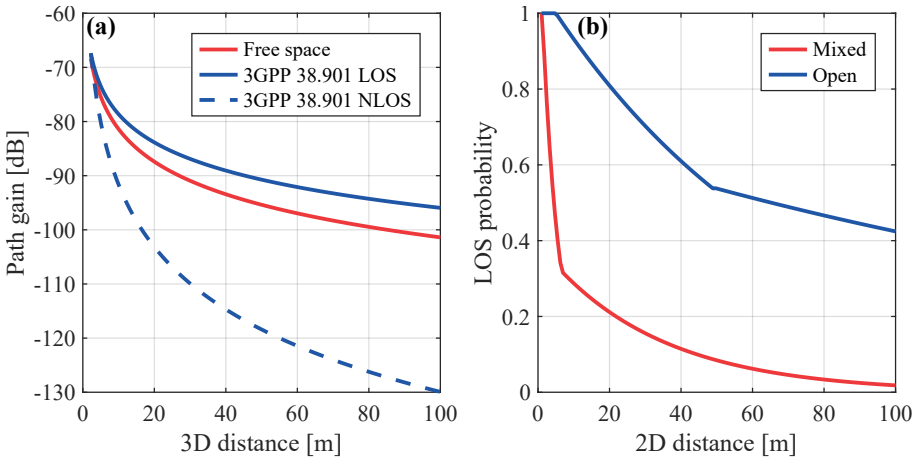


Figure 5.3: (a) Path gain in indoor environment at 28 GHz. (b) Distance-dependent LOS probability of indoor open and mixed office environments.

the $m$-th PAA and the $k$-th UE is computed as

$$\widetilde{h}_{k,q,m}(t) = \sum_{i=0}^{I} h'_{i,k,q,m}\delta(t-\tau_i), \tag{5.14}$$

where $h'_{i,k,q,m}$ is the impulse-response corresponding to the $i$-th path between the $m$-th PAA when it is beam-steered towards the $q$-th direction, $q \in \{1,\ldots,Q_{az}\times Q_{el}\}$ and the $k$-th UE, and $\tau_i$ is the time delay in the $i$-th path. $I+1$ is the number of channel paths: at most one LOS if it exists and $I$ NLOS. When there is no LOS path between $m$-th PAA and $k$-th UE, $h'_{0,k,q,m}$ is zero. The parameters outlined in Table 5.1 are utilized to determine the angles and delays associated with the $i$-th NLOS path. Consequently, it is possible to compute the precise locations of both the first bounce scatterer (FBS) and the last bounce scatterer (LBS), referring to the initial and final reflections along the path, respectively. It is worthwhile to note that both the radiation pattern of the PAAs and the UEs are taken into account in the computation of Eq. (5.14). For the sake of simplicity, the UE antenna radiation pattern is considered isotropic, thus it has no effect on the channel. Finally, $\widetilde{h}_{k,q,m}(t)$ is converted to the frequency domain to obtain $\widetilde{H}_{k,q,m}(f)$, the $(k,q,m)$ entry of the spatial channel transfer matrix $\widetilde{\mathbf{H}}$.

### 5.3.3 Beam Selection for Channel Matrix Building

The final channel matrix $\mathbf{H}$ is generated using the spatial channel transfer matrix $\widetilde{\mathbf{H}}$ in conjunction with a beam selection algorithm. In our algorithm, we choose beams that maximize the MU-MIMO achievable sum rate capacity

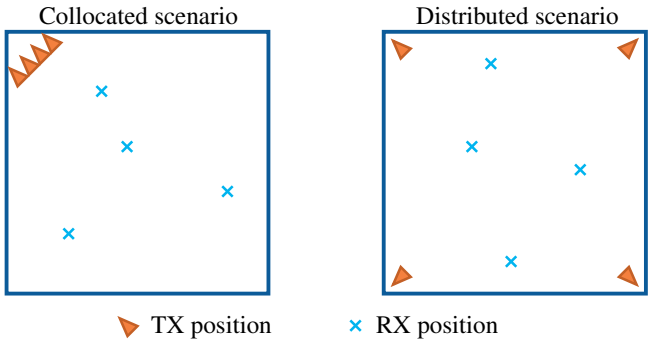


Figure 5.4: Horizontal layout of the simulated indoor office.

because it is a fundamental figure of merit for a wireless system. The approach assumes an exhaustive search scheme, as suggested in [110]. It evaluates all the possible combinations of the beams and chooses the optimal selection. It is assumed that all channels from the PAAs' individual beams to the UEs are known. Each of $M$ PAAs produces $Q_{az} \times Q_{el}$ beams, resulting in a total of $(Q_{az} \times Q_{el})^M$ beam combinations. After evaluating the achievable sum rate capacity of each combination using Eq. (5.10), the optimum combination can be selected,

$$(i_1, \ldots, i_M) = \underset{i_1,\ldots,i_M=1,\ldots,Q_{az}Q_{el}}{\operatorname{argmax}} \mathrm{SR}. \tag{5.15}$$

This approach optimizes the performance but it is a time-consuming solution and requires further investigation.

## 5.4 Simulation Scenarios and Simulation Steps

### 5.4.1 Collocated vs. Distributed Antenna Systems

As discussed above, we aim to investigate the performance of various PAA systems in two essentially different deployment scenarios:

- Collocated PAAs.
- Distributed PAAs.

Fig. 5.4 depicts an aerial view of the two scenarios. In the collocated scenario, all PAAs are placed next to each other in one corner of the room, while in the distributed scenario, PAAs are placed in all four corners of the room.

We specialize our results to the indoor environment comprising a room of $80 \times 80 \times 3$ m$^3$ in size. The placement heights of the PAAs and the UE antennas are 3 m and 1 m, respectively. The positions of the UEs in the room are random in the horizontal plane with a uniform distribution. The room parameters are

Table 5.2: Properties of simulation cases

| Case | 1 | | 2 | | 3 |
|---|---|---|---|---|---|
| No. of UEs, $K$ | 4 | | 4 | | 4 |
| No. of PAAs, $M$ | 4 | | 4 | | 4 |
| No. Az. beams, $Q_{az}$ | 16 | 8 | 16 | 8 | 16 |
| No. El. beams, $Q_{el}$ | 1 | 2 | 1 | 2 | 1 |
| Az. angular step [°] | 7.5 | 15 | 7.5 | 15 | 7.5 |
| El. angular step [°] | - | 5 | - | 5 | - |
| $G_A$ @ BS [dBi] | 29.4 | | 23.4 | | 23.1 |
| Max cond. power, $P_{c,max}$ [dBm] | 28 | | 22 | | 28 |
| Max EIRP @ BS [dBm] | 57.4 | | 45.4 | | 51.1 |
| Az. HPBW @ BS [°] | 5.7 | | 24.3 | | 12.2 |
| El. HPBW @ BS [°] | 5.4 | | 5.4 | | 11.6 |
| Array size, $N_{az} \times N_{el}$ | $16 \times 4$ | | $4 \times 4$ | | $8 \times 1$ |
| Polarization of PAA | 45°-slant | | 45°-slant | | horizontal |
| Polarization of UE | 45°-slant | | 45°-slant | | horizontal |

defined according to Table 7.2-2 in [106], where a detailed scenario description is provided for channel model calibration. The center-to-center distance between neighboring PAAs in collocated scenarios is considered 20 cm, and they are aligned to have the BS direction towards the center of the room.

For each scenario and propagation environment mentioned above, three simulation cases are considered, the details of which are given in Table 5.2. Hereafter, the number of UEs and PAAs in all simulations is $K = M = 4$. Cases 1 and 2 make use of the PAA presented in Chapter 3, which is capable of analog beamforming within an angular range of $\pm 60°$ and $\pm 10°$ in the azimuth and elevation planes, respectively. A useful feature of this PAA is that it is modular with four identical and independent subarrays. Therefore, the PAA is able to function in two ways: first, all subarrays form one large PAA, which corresponds to Case 1, and second, each subarray works as an independent PAA, as in Case 2. Case 1 has a high antenna gain of 29.4 dBi in the BS direction. Case 2 has a lower antenna gain of 23.4 dBi in the BS direction. As a result of the high antenna gain and larger aperture in Case 1, its half-power beamwidth (HPBW) is smaller than that of Case 2. Case 3 uses a PAA with a 23.1 dBi antenna gain in the BS direction, which is presented in Chapter 4. This PAA is capable of beamforming in the azimuth plane only within an angular range of $\pm 60°$. The beam coverage of the PAAs is shown in Fig. 5.5, where the antenna gain by the PAAs in the main beams at each angle $[Q_{az}, Q_{el}]$ is shown.

Another important property of PAAs is effective isotropic radiated power (EIRP), which is defined as EIRP $= P_c G_A$, where $P_c$ is the conductive power and $G_A$ is the total array antenna gain. The maximum EIRP values for the

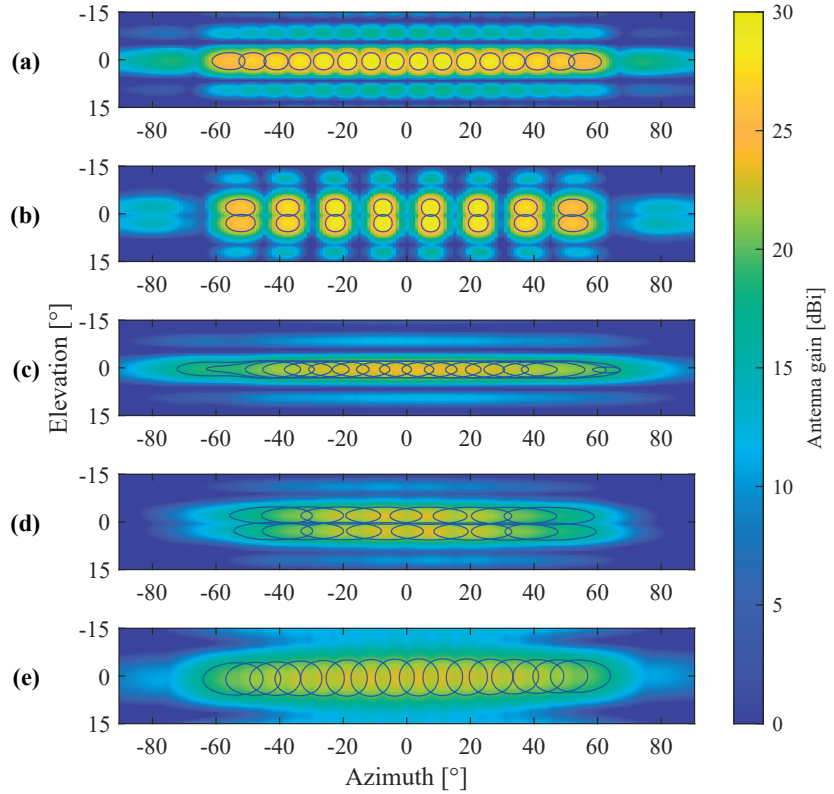


Figure 5.5: The beam coverage of PAAs, when all the possible beams are combined. (a) Case 1 with $[Q_{az}, Q_{el}] = [16, 1]$, (b) Case 1 with $[Q_{az}, Q_{el}] = [8, 2]$, (c) Case 2 with $[Q_{az}, Q_{el}] = [16, 1]$, (d) Case 2 with $[Q_{az}, Q_{el}] = [8, 2]$, and (e) Case 3, where $[Q_{az}, Q_{el}] = [16, 1]$. Overlaid are the 3 dB contours of the beams.

PAAs considered here are 9 dB backed off from their saturation points in order to preserve signal linearity. These EIRP values are used in conjunction with the conductive powers $P_c$ in the simulations. The maximum conductive power $P_{c,max}$ is chosen to meet the maximum total radiated power (TRP) for local area base stations of 33 dBm [69].

### 5.4.2 Simulation Steps

A concise flow chart of the main simulation steps is shown in Fig. 5.6. The structure follows the modeling approach outlined above, including the computation of the figures of merit of interest.

The simulation study focuses on the comparison of the deployment of two different PAAs, realized in fundamentally two different spatial configurations

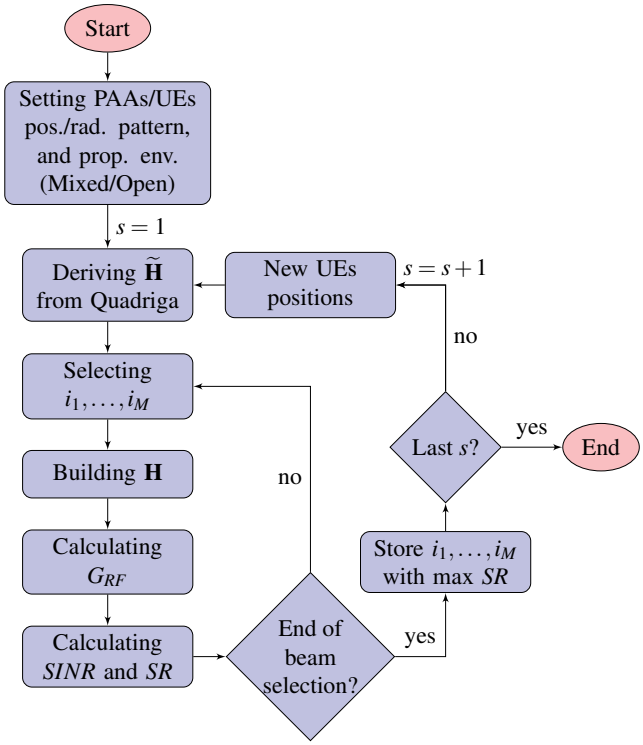


Figure 5.6: Flow chart of the simulation steps.

of the PAAs in two different indoor propagation environments, and evaluated for two different beamforming algorithms.

The operational frequency chosen for the simulations is 28 GHz. The noise power and interference level play important roles in the quality of the received signal. Here and for the rest of the chapter, we assume the noise power at the UEs is $\sigma_n^2 = N_0 B = -99$ dBm, where $N_0 = -174$ dBm/Hz is the thermal noise power in a one-hertz bandwidth at room temperature and $B = 30$ MHz is the signal bandwidth assumed throughout all simulations. The total number of samples for a single simulation is 500, hence, $s = 1, \ldots, 500$. All computed parameters are shown as empirical cumulative distribution functions (CDFs). Corresponding mean values and standard deviations are also computed. For $G_{RF}$, the received signal, interference, and SINR, mean and standard deviation values are computed in the logarithmic domain. This is due to the log-normal distribution of these parameters in downlink cellular networks [111].

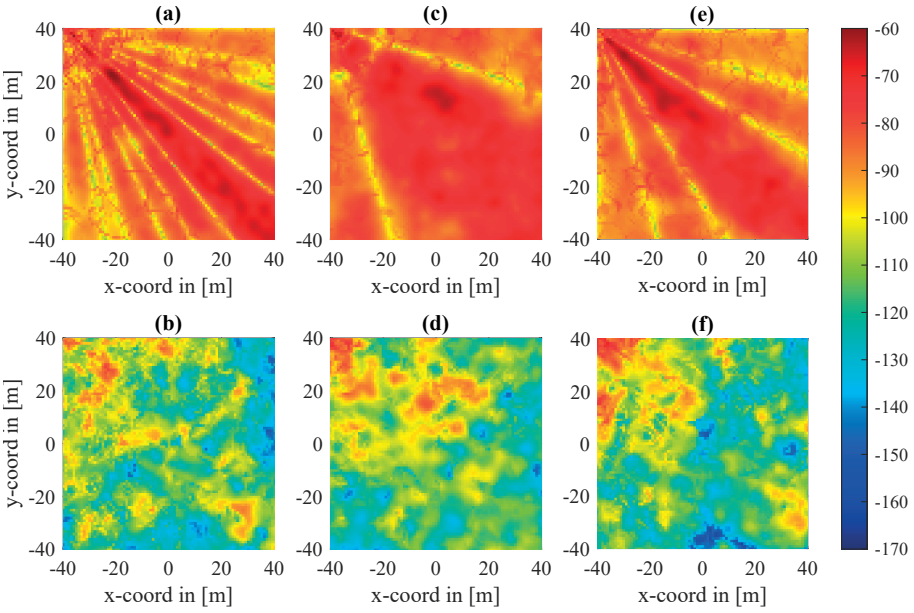


Figure 5.7: The distribution of the path gain plus antenna gain (in dB) in two propagation conditions and three PAA cases. (a) Case 1 in the 3GPP 38.901 indoor LOS channel, (b) case 1 in the 3GPP 38.901 indoor NLOS channel, (c) case 2 in the 3GPP 38.901 indoor LOS channel, (d) case 2 in the 3GPP 38.901 indoor NLOS channel, (e) case 3 in the 3GPP 38.901 indoor LOS channel, and (f) case 3 in the 3GPP 38.901 indoor NLOS channel.

## 5.5 Simulation Results and Analysis

### 5.5.1 Path Gain

To illustrate the impact of the propagation channels on the received signals when beamforming is employed, we compute the received signal at several positions evenly distributed over the simulated room for two different propagation channels. Fig. 5.7 shows the distribution of the link path gain plus antenna gain (in dB) for the PAAs in all cases. Results are shown when the arrays transmit in the BS direction. Two propagation channels are considered:

- The 3GPP 38.901 indoor LOS channel.
- The 3GPP 38.901 indoor NLOS channel.

The path gains in these cases are spatially correlated. The effects of the main lobe, side lobes, and also nulls of the antenna's radiation pattern are visible in Fig. 5.7(a), (c), and (e). Multipath propagation has changed the path gain distribution considerably. As a result, at some positions, more visibly in

the direction of pattern nulls specifically, the gain has increased. The distribution of the received signal has become more even. In Fig. 5.7(b), (d), and (f), there is no effect of the radiation pattern visible anymore, and the path gain plus antenna gain has dropped significantly. Computing the average of the path gain (in linear scale) over all the simulated positions of the room is $-75.5$, $-100.6$, $-75.2$, $-96.7$, $-75.6$ and $-94.4$ dB when converted to dB scale. These values correspond to Fig. 5.7(a) through (f). These average values are well correlated with the respective PLEs. As can be seen from the above results, the propagation channel will have a non-negligible impact on the system performance as evaluated next.

### 5.5.2 RF PA Gains

The CDFs of RF PA Gain $G_{RF}$ Eq. (5.9) of all PAAs or equivalently total RF transmit power (see Appendix A.2) for the three considered cases are shown in Fig. 5.8, 5.9, and 5.10. The mean and standard deviation corresponding to these CDFs are presented in Tables 5.3 and 5.4. The following observations can be made from the aforementioned figures and tables. The distributed scenario (Dist) requires less RF transmit power than the collocated scenario (Coll) in all cases. The required power is on the order of $\approx 1.7$ dB lower on average, which is about 50% less transmit power. The choice of precoding scheme affects the total RF transmit power too. Indeed, ZF requires a higher transmit power than MF, which is expected because MF is well-known to optimize the link power while ZF minimizes interference. In fact, the MF requires $\approx 1$ dB (25%) less power than the ZF. However, it depends on the environment and the antenna distribution too, as explained above. Case 1 and 3, having the same $P_{c,max}$, are using an equal amount of RF power. Case 2 transmits roughly 6 dB (300%) less than the other cases, where it has 6 dB less $P_{c,max}$ as well. On the other hand, the spatial beam arrangement of each individual PAA ($[Q_{az}, Q_{el}]$) shows no significant change in the total RF transmit power.

### 5.5.3 Received Signal, Interference and SINR

Tables 5.5 and 5.6 show the mean and standard deviation of the received signal power in the UE locations in all cases. The reception by UEs also shows improved performances when the PAAs are distributed in all cases. This is due to the higher path gain in the distributed scenario. Besides, the standard deviation of the received signal power decreases when PAAs are distributed. In the open environment, the LOS probability is higher, therefore the received signal level is also increased generally. Almost always in the distributed scenario of the open environment, the UEs are within LOS distance of at least one PAA, but in the collocated scenario, there is a large probability that the UEs do not see any PAA in their LOS. The mean of the received signal level in the distributed deployment of the open environment is $\approx 20$ dB higher than the mixed environment.

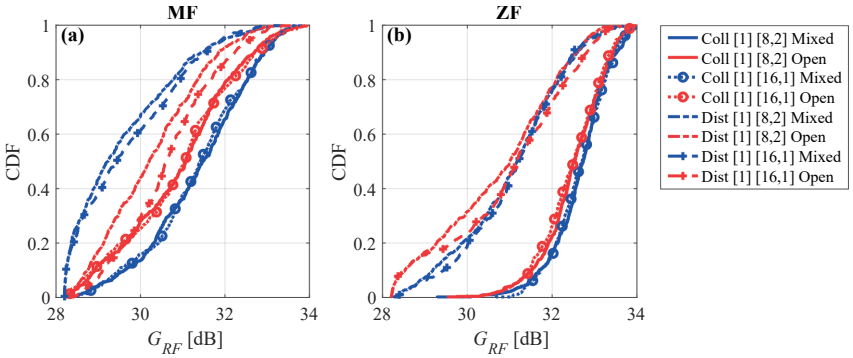


Figure 5.8: The CDFs of $G_{RF}$ in case 1: (a) MF, and (b) ZF.

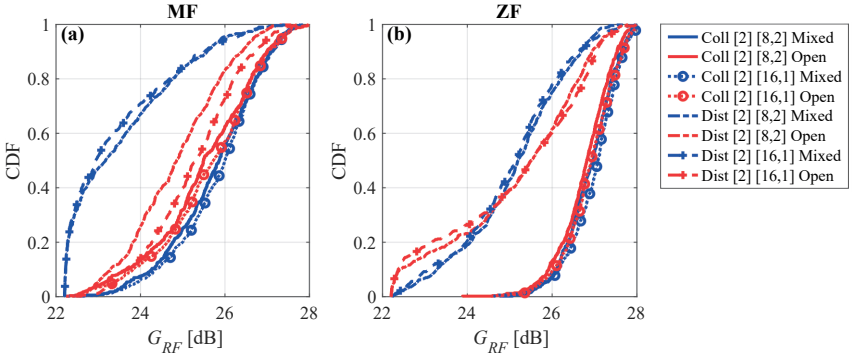


Figure 5.9: The CDFs of $G_{RF}$ in case 2: (a) MF, and (b) ZF.

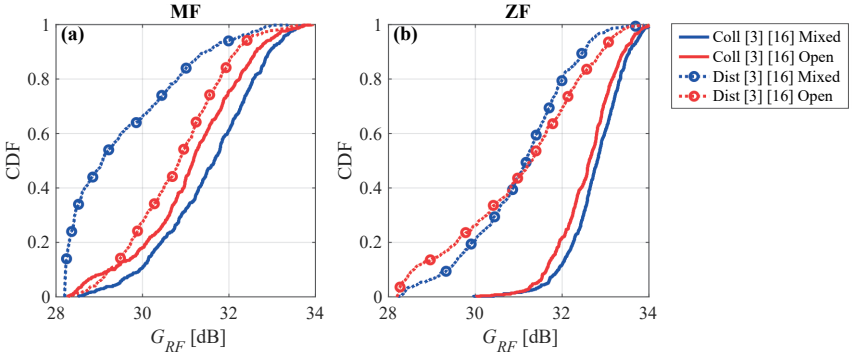


Figure 5.10: The CDFs of $G_{RF}$ in case 3: (a) MF, and (b) ZF.

The mean and standard deviation of interference signal power at the position of each UE are shown in Tables 5.7 and 5.8. In these tables, only results for MF precoding are presented. The interference level is almost zero in ZF

Table 5.3: Mean of $G_{RF}$ [dB], comparing collocated and distributed scenarios.

| | $[Q_{az}, Q_{el}]$ | Mixed | | | | Open | | | |
|---|---|---|---|---|---|---|---|---|---|
| | | MF | | ZF | | MF | | ZF | |
| | | Coll | Dist | Coll | Dist | Coll | Dist | Coll | Dist |
| Case 1 | [16, 1] | 31.3 | 29.7 | 32.7 | 31.1 | 30.9 | 30.7 | 32.4 | 31.0 |
| | [8, 2] | 31.4 | 29.6 | 32.7 | 31.0 | 30.9 | 30.3 | 32.5 | 30.8 |
| Case 2 | [16, 1] | 25.8 | 23.4 | 27.0 | 25.0 | 25.6 | 25.3 | 26.9 | 25.2 |
| | [8, 2] | 25.7 | 23.5 | 26.9 | 25.1 | 25.5 | 24.8 | 26.8 | 25.2 |
| Case 3 | [16, 1] | 31.5 | 29.5 | 32.8 | 31.0 | 31.1 | 30.8 | 32.6 | 31.0 |

Table 5.4: Standard deviation of $G_{RF}$ [dB], comparing collocated and distributed scenarios.

| | $[Q_{az}, Q_{el}]$ | Mixed | | | | Open | | | |
|---|---|---|---|---|---|---|---|---|---|
| | | MF | | ZF | | MF | | ZF | |
| | | Coll | Dist | Coll | Dist | Coll | Dist | Coll | Dist |
| Case 1 | [16, 1] | 1.2 | 1.3 | 0.7 | 1.2 | 1.4 | 1.1 | 0.8 | 1.5 |
| | [8, 2] | 1.2 | 1.3 | 0.7 | 1.2 | 1.3 | 1.2 | 0.8 | 1.4 |
| Case 2 | [16, 1] | 1.0 | 1.3 | 0.6 | 1.3 | 1.2 | 1.1 | 0.6 | 1.7 |
| | [8, 2] | 1.1 | 1.3 | 0.6 | 1.2 | 1.2 | 1.1 | 0.6 | 1.6 |
| Case 3 | [16, 1] | 1.2 | 1.3 | 0.7 | 1.2 | 1.2 | 1.1 | 0.7 | 1.5 |

precoding, as it was shown earlier. In the distributed scenario, the level of interference also increases, similar to the received signal level, but the intensity of the increment is less.

Finally, the SINRs at the UE locations are computed using Eq. (5.5) and shown in Figs. 5.11, 5.12, and 5.13 for all three cases. The mean and standard deviation of these CDFs are presented in Tables 5.9 and 5.10. The improvement of the distributed deployment over the collocated deployment can be seen across all the results. It should be noted here that ZF precoding results in an SINR distribution with a smaller standard deviation. This gives the benefit of a more reliable link between PAAs and UEs.

### 5.5.4 Achievable Sum Rate

Figs. 5.14, 5.15, and 5.16 show the CDF of the achievable sum rate computed by Eq. (5.10), where all the curves have been obtained from 500 simulated data points. It can be immediately seen that the distributed scenario always leads to higher SR levels, as expected because of the similar behavior of the SINR. For instance, in the mixed environment, where all the antennas have 16 beams in azimuth planes and the MF precoding scheme is used, the mean of the SR is increased in all cases, by 4, 3, and 3 bps/Hz, respectively. This is due to the fact that the likelihood of a UE being closer to a PAA increases in the

Table 5.5: Mean of received signal power [dBm], comparing collocated and distributed scenarios.

| | $[Q_{az}, Q_{el}]$ | Mixed | | | | Open | | | |
|---|---|---|---|---|---|---|---|---|---|
| | | MF | | ZF | | MF | | ZF | |
| | | Coll | Dist | Coll | Dist | Coll | Dist | Coll | Dist |
| Case 1 | [16, 1] | −88 | −77 | −82 | −74 | −87 | −54 | −78 | −53 |
| | [8, 2] | −90 | −78 | −84 | −75 | −89 | −57 | −80 | −56 |
| Case 2 | [16, 1] | −94 | −85 | −91 | −85 | −91 | −59 | −87 | −63 |
| | [8, 2] | −93 | −84 | −90 | −83 | −92 | −59 | −86 | −61 |
| Case 3 | [16, 1] | −89 | −79 | −84 | −77 | −87 | −55 | −80 | −56 |

Table 5.6: Standard deviation of received signal power [dBm], comparing collocated and distributed scenarios.

| | $[Q_{az}, Q_{el}]$ | Mixed | | | | Open | | | |
|---|---|---|---|---|---|---|---|---|---|
| | | MF | | ZF | | MF | | ZF | |
| | | Coll | Dist | Coll | Dist | Coll | Dist | Coll | Dist |
| Case 1 | [16, 1] | 25 | 23 | 5 | 4 | 43 | 21 | 8 | 12 |
| | [8, 2] | 26 | 23 | 6 | 4 | 42 | 20 | 8 | 11 |
| Case 2 | [16, 1] | 23 | 22 | 5 | 4 | 39 | 16 | 8 | 12 |
| | [8, 2] | 24 | 22 | 5 | 4 | 41 | 17 | 8 | 12 |
| Case 3 | [16, 1] | 24 | 24 | 5 | 4 | 41 | 19 | 8 | 12 |

distributed scenario.

ZF precoding scheme shows a larger improvement in the distributed over collocated scenario as compared to the MF precoding. It is mainly because ZF removes the interference at UE positions. The effect of the environment on the system performance can be inferred from the figures too. In Case 1, for example, when all 16 beams are in azimuth planes ($[Q_{az}, Q_{el}] = [16, 1]$), the mean SR increases from 23 to 33 bps/Hz in the indoor mixed environment and from 28 to 61 bps/Hz in the open environment. It can be seen that there is a significant increase in the SR in the open environment, and that is because of the higher LOS probability. The distribution of PAAs increases the chance for UEs to make a LOS link with at least one PAA in the open environment. Similar behavior can be observed in other cases and precoding schemes as well.

The SR increases slightly in both scenarios of Case 1 when $[Q_{az}, Q_{el}] = [16, 1]$ in comparison with $[Q_{az}, Q_{el}] = [8, 2]$. Since the vertical spread of the UE locations in the indoor environment is limited, it is advantageous that all of the beams are in the same plane when the HPBW is small. With $[Q_{az}, Q_{el}] = [16, 1]$ all the beams cover the azimuth plane within their HPBW (look at Fig. 5.5(a) and (b)). Meanwhile, the opposite effect can be seen in both scenarios of case 2, where beams with larger HPBW are employed. When $[Q_{az}, Q_{el}] = [8, 2]$ is used, it causes an increase in SR in both collocated and distributed scenarios.

Table 5.7: Mean of interference power [dBm], comparing collocated and distributed scenarios.

| | $[Q_{az}, Q_{el}]$ | Mixed | | | | Open | | | |
|---|---|---|---|---|---|---|---|---|---|
| | | MF | | ZF | | MF | | ZF | |
| | | Coll | Dist | Coll | Dist | Coll | Dist | Coll | Dist |
| Case 1 | [16, 1] | −93 | −87 | – | – | −86 | −68 | – | – |
| | [8, 2] | −94 | −86 | – | – | −87 | −69 | – | – |
| Case 2 | [16, 1] | −97 | −90 | – | – | −90 | −68 | – | – |
| | [8, 2] | −97 | −90 | – | – | −89 | −69 | – | – |
| Case 3 | [16, 1] | −93 | −85 | – | – | −86 | −66 | – | – |

Table 5.8: Standard deviation of interference power [dBm], comparing collocated and distributed scenarios.

| | $[Q_{az}, Q_{el}]$ | Mixed | | | | Open | | | |
|---|---|---|---|---|---|---|---|---|---|
| | | MF | | ZF | | MF | | ZF | |
| | | Coll | Dist | Coll | Dist | Coll | Dist | Coll | Dist |
| Case 1 | [16, 1] | 7 | 8 | – | – | 12 | 9 | – | – |
| | [8, 2] | 7 | 8 | – | – | 12 | 10 | – | – |
| Case 2 | [16, 1] | 7 | 8 | – | – | 12 | 9 | – | – |
| | [8, 2] | 7 | 8 | – | – | 13 | 10 | – | – |
| Case 3 | [16, 1] | 7 | 9 | – | – | 13 | 9 | – | – |

Fig. 5.5(c) and (d) show the beam coverage by the antenna of case 2. Tables 5.11 and 5.12 summarize the mean and standard deviation of all the simulations.

Table 5.13 and 5.14 provide an overview of the top four simulation conditions, ranked according to the SR mean in the indoor mixed and indoor open environments, respectively. The table also presents the SR values when CDF is equal to 0.05 ($F_{\mathrm{SR}} = 0.05$). Distributed scenarios will always achieve better performance than collocated scenarios. In addition to this, in comparison to MF, the ZF precoding scheme offers a higher average achievable sum rate capacity. A high SR can also be expected from the open office propagation environment due to the higher probability of the LOS condition.

## 5.6 Summary and Conclusions

In this chapter, we presented the performance of three state-of-the-art 28-GHz PAAs in indoor environment channel models as specified by 3GPP 38.901. These PAAs, the designs of which were introduced in earlier chapters of the thesis, were proposed for high-data-rate communication. Therefore their capability to satisfy this goal in mmWave 5G is investigated in different settings of the indoor environment, namely, the placement of PAAs, analog beam config-

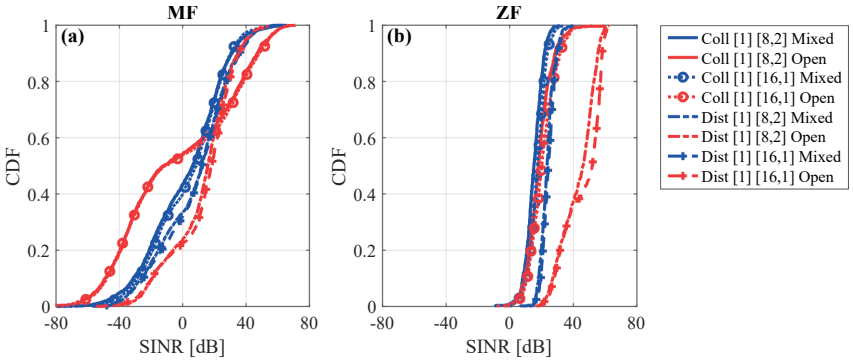


Figure 5.11: The CDFs of SINR at the UE locations in case 1: (a) MF, and (b) ZF.

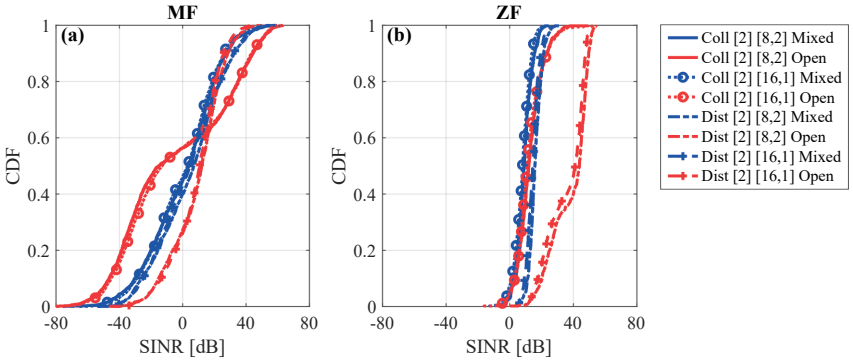


Figure 5.12: The CDFs of SINR at the UE locations in case 2: (a) MF, and (b) ZF.

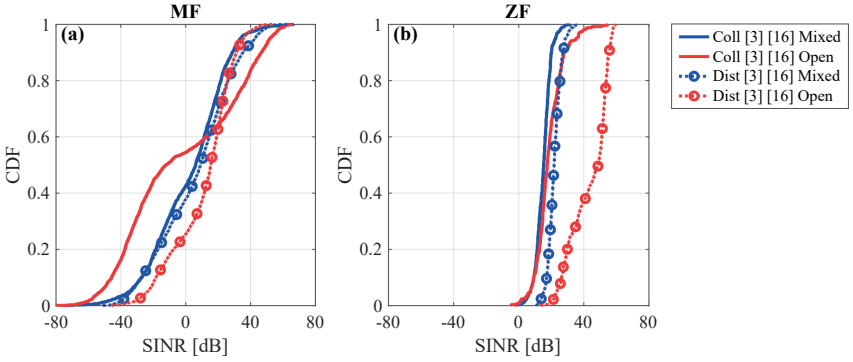


Figure 5.13: The CDFs of SINR at the UE locations in case 3: (a) MF, and (b) ZF.

Table 5.9: Mean of SINR [dB], comparing collocated and distributed scenarios.

| | $[Q_{az}, Q_{el}]$ | Mixed | | | | Open | | | |
|---|---|---|---|---|---|---|---|---|---|
| | | MF | | ZF | | MF | | ZF | |
| | | Coll | Dist | Coll | Dist | Coll | Dist | Coll | Dist |
| Case 1 | [16, 1] | 3 | 9 | 17 | 25 | −3 | 13 | 21 | 46 |
| | [8, 2] | 2 | 8 | 15 | 24 | −3 | 12 | 19 | 43 |
| Case 2 | [16, 1] | 0 | 4 | 8 | 14 | −4 | 8 | 12 | 36 |
| | [8, 2] | 1 | 5 | 9 | 16 | −5 | 9 | 13 | 38 |
| Case 3 | [16, 1] | 2 | 6 | 15 | 22 | −3 | 11 | 19 | 43 |

Table 5.10: Standard deviation of SINR [dB], comparing collocated and distributed scenarios.

| | $[Q_{az}, Q_{el}]$ | Mixed | | | | Open | | | |
|---|---|---|---|---|---|---|---|---|---|
| | | MF | | ZF | | MF | | ZF | |
| | | Coll | Dist | Coll | Dist | Coll | Dist | Coll | Dist |
| Case 1 | [16, 1] | 23 | 23 | 5 | 4 | 38 | 20 | 8 | 12 |
| | [8, 2] | 24 | 23 | 6 | 4 | 37 | 20 | 8 | 11 |
| Case 2 | [16, 1] | 21 | 21 | 5 | 4 | 35 | 15 | 8 | 12 |
| | [8, 2] | 22 | 21 | 5 | 4 | 36 | 17 | 8 | 12 |
| Case 3 | [16, 1] | 22 | 23 | 5 | 4 | 36 | 18 | 8 | 12 |

uration, digital precoding scheme, and the environmental condition.

The findings demonstrate that the distributed deployment of PAAs consistently yields a higher achievable sum rate capacity compared to the scenario where all PAAs are collocated. The configuration of analog beams of the PAAs can also increase the capacity if selected according to the antenna array's characteristics. When having narrow beams (HPBW = 5.7°) with high directivity (Case 1), better performance is achieved with all 16 beams in the azimuth plane. But with wider beams of Case 2, a higher sum rate capacity is obtained with the [8, 2] beam configuration which has lower overlap between the beams compared to the [16, 1] one. Employing ZF precoding shows usually a great advantage in the phased array with high power, however, it requires a more complicated implementation compared to MF.

The choice of PAA for indoor environment wireless communication involves multiple parameters. Although PAAs with high EIRP are necessary for this purpose, many more conditions need to be set to achieve high-data-rate communication.

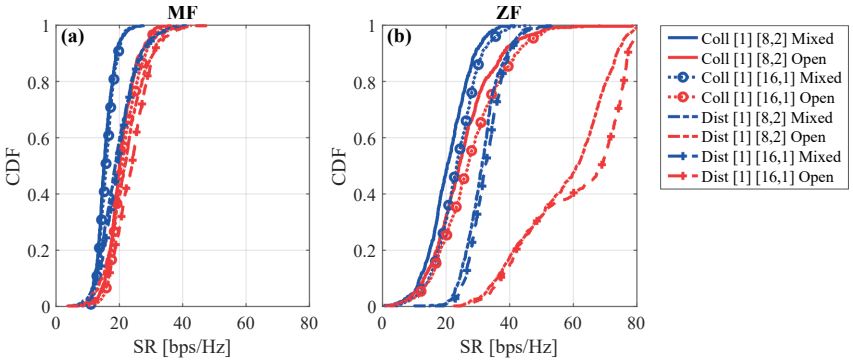


Figure 5.14: The CDFs of achievable sum rate capacity in case 1: (a) MF, and (b) ZF.

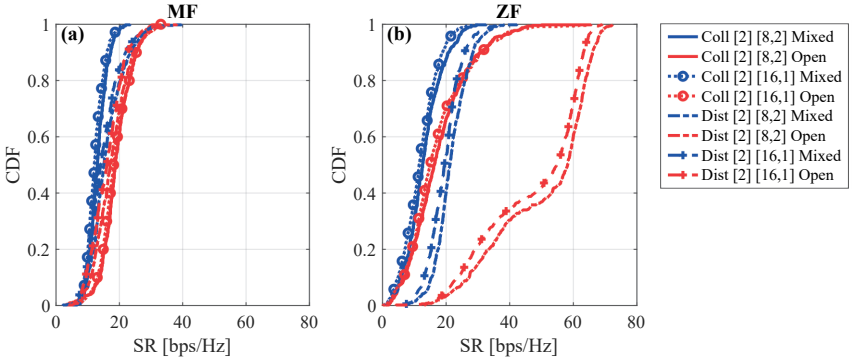


Figure 5.15: The CDFs of achievable sum rate capacity in case 2: (a) MF, and (b) ZF.

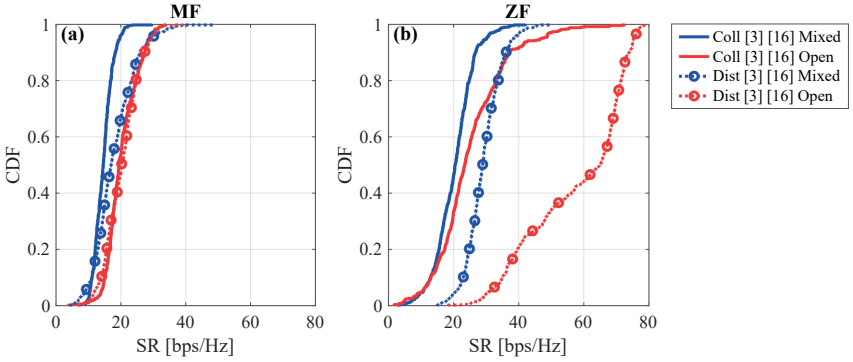


Figure 5.16: The CDFs of achievable sum rate capacity in case 3: (a) MF, and (b) ZF.

Table 5.11: Mean of SR [bps/Hz], comparing collocated and distributed scenarios.

| | $[Q_{az}, Q_{el}]$ | Mixed | | | | Open | | | |
|---|---|---|---|---|---|---|---|---|---|
| | | MF | | ZF | | MF | | ZF | |
| | | Coll | Dist | Coll | Dist | Coll | Dist | Coll | Dist |
| Case 1 | [16, 1] | 16 | 20 | 23 | 33 | 22 | 24 | 28 | 61 |
| | [8, 2] | 16 | 19 | 21 | 31 | 21 | 22 | 25 | 57 |
| Case 2 | [16, 1] | 12 | 15 | 12 | 20 | 19 | 16 | 17 | 47 |
| | [8, 2] | 13 | 16 | 13 | 22 | 19 | 18 | 18 | 51 |
| Case 3 | [16, 1] | 15 | 18 | 20 | 29 | 20 | 20 | 25 | 58 |

Table 5.12: Standard deviation of SR [bps/Hz], comparing collocated and distributed scenarios.

| | $[Q_{az}, Q_{el}]$ | Mixed | | | | Open | | | |
|---|---|---|---|---|---|---|---|---|---|
| | | MF | | ZF | | MF | | ZF | |
| | | Coll | Dist | Coll | Dist | Coll | Dist | Coll | Dist |
| Case 1 | [16, 1] | 2.7 | 5.8 | 6.9 | 5.7 | 4.7 | 6.1 | 10.8 | 16.1 |
| | [8, 2] | 2.8 | 5.9 | 6.8 | 5.9 | 4.5 | 6.2 | 10.3 | 14.4 |
| Case 2 | [16, 1] | 2.8 | 5.2 | 5.4 | 5.2 | 4.8 | 5.2 | 10.2 | 15.7 |
| | [8, 2] | 2.9 | 5.4 | 5.7 | 5.3 | 4.8 | 5.6 | 9.6 | 15.5 |
| Case 3 | [16, 1] | 2.8 | 6.3 | 5.9 | 5.4 | 4.8 | 5.3 | 10.8 | 15.4 |

Table 5.13: The scenarios with the best performance are sorted by mean of SR in the mixed environment.

| PAA case | Beam config. | Precod. scheme | Scenario | SR [bps/Hz] | |
|---|---|---|---|---|---|
| | | | | Mean | $F_{\mathrm{SR}} = 0.05$ |
| 1 | [16,1] | ZF | Dist. | 33 | 24 |
| 1 | [8,2] | ZF | Dist. | 31 | 23 |
| 3 | [16,1] | ZF | Dist. | 29 | 21 |
| 2 | [8,2] | ZF | Dist. | 22 | 14 |

Table 5.14: The scenarios with the best performance are sorted by mean of SR in the open environment.

| PAA case | Beam config. | Precod. scheme | Scenario | SR [bps/Hz] | |
|---|---|---|---|---|---|
| | | | | Mean | $F_{\mathrm{SR}} = 0.05$ |
| 1 | [16,1] | ZF | Dist. | 61 | 34 |
| 3 | [16,1] | ZF | Dist. | 58 | 31 |
| 1 | [8,2] | ZF | Dist. | 57 | 33 |
| 2 | [8,2] | ZF | Dist. | 51 | 22 |

# Chapter 6

# Conclusions and Directions for Further Research

The thesis has addressed several critical aspects of mmWave phased array systems, i.e., challenges in terms of low-loss antenna elements, high-power front-ends, and efficient integration to achieve high EIRP in a wide-angle beam scanning range over a large bandwidth, compact form factor, and cost-effectiveness. Gapwaveguides have emerged as a viable solution, bridging the gap between dielectric substrate-based planar transmission lines and non-planar rectangular and circular waveguides. They offer a feasible, low-cost, and low-loss transmission line for mmWave frequencies, overcoming many challenges associated with traditional waveguide structures, such as high-loss, power handling, bandwidth, and complexity.

Hybrid beamforming, which combines analog and digital beamforming techniques, has proven to be the primary choice for achieving beamforming capabilities in mmWave systems. Moreover, designing phased arrays compatible with hybrid beamforming has been the focus of researchers in the last few years. Two phased arrays based on gapwaveguide technology are designed and verified for this purpose. In order to integrate the antenna elements with the active RF circuitry, different transition topologies are designed and proposed.

Additionally, the thesis emphasizes the significance of high-power phased arrays in developing mmWave 5G applications. High-power phased arrays are crucial in achieving the desired coverage and data rates in mmWave communication. The thesis contributes to developing efficient and powerful phased array systems suitable for mmWave 5G applications by leveraging the advancements in gapwaveguide technology and integrating high-power front-ends.

Last but not least, the focus is on evaluating the downlink performance of the proposed phased arrays in indoor environments as densely populated areas. mmWave 5G aims to provide high-data-rate coverage in areas with high user density, such as indoor environments. This aligns with the primary objective of mmWave 5G deployment. Considering specific challenges posed

by indoor environments, such as higher NLOS probability and blockage, the thesis addresses the performance analysis of the designed phased arrays in such scenarios.

## 6.1 Conclusions

The main contributions of this thesis can be summarized as follows:

- The thesis presents two major types of microstrip to ridge gapwaveguide transitions: top PCB and through PCB. Depending on the assembly design of the system's antenna element and the active RF circuitry components, different PCB designs are needed. Three types of top PCB microstrip to ridge gapwaveguide transitions are designed for the frequency range of $26.5-29.5$ GHz. A wideband through PCB microstrip to waveguide transition is designed as well. The performance of these transitions is evaluated when integrated with a previously designed antenna array. Through PCB transitions offer wider bandwidth and more robustness to tolerances but with more insertion loss. Top PCB transitions are independent of the PCB stack-up but they occupy a relatively larger space on the PCB.

- In this thesis, gapwaveguide technology is employed to design antenna element components. It offers wide bandwidth and low loss, and is used to simplify the phased array structure and to handle a high power. In order to comply with the antenna array spacing requirement, only one row of pins was placed between elements. This provided an isolation of $< -17$ dB over the band. The gapwaveguide technology does not have the capability to deliver dual-polarized antenna elements with a small form factor yet. Therefore this technology is a great candidate for designing phased arrays with a single polarization. Gapwaveguide-based antennas, similar to the other waveguide-based antennas, need to be used in subarray form in the design of phased arrays, which limits the scanning range in one plane.

- A linear array antenna with eight antenna elements is designed using gapwaveguide technology. Each element features eight radiating slots and is fed from the center. Combining radiating elements and feeding them together, i.e. subarraying, offers a higher antenna gain per channel, and maintaining the element width close to $0.5\lambda_0$ makes the antenna element suitable to be employed in an array configuration with wide beam scanning. Designing antennas in gapwaveguide technology provides the advantage of integration with active components that dissipate a large amount of heat. This antenna is specifically tailored for 5G applications at mmWave frequencies, which can scan the E-plane within a range of $\pm 45°$. The antenna demonstrates excellent performance characteristics, including an active reflection coefficient of less than $-10$ dB across all scan

angles and frequencies and an average gain of 23 dBi at the broadside. Hence, Gapwaveguide-based phased array antennas can achieve high gain over a wide range of scanning angles and bandwidth.

- A two-port antenna with ±45°-slant polarizations based on gapwaveguide technology is presented. Slant polarizations offer lower side lobe levels in the principal planes compared to those with horizontal and/or vertical polarization. Designing an antenna with two ±45°-slant polarizations is significantly easier than designing a horizontal-vertical one. This is due to the structural symmetry in the structure of the ±45°-slant antennas. The antenna consists of two arrays, each with eight radiating slots and slant polarization. Operating within the frequency band of 24.25 to 27.25 GHz, this antenna is suitable for 5G applications at mmWave frequencies. The two orthogonal linear polarizations show similar radiation patterns for both polarizations over a wide frequency band, due to their geometrical symmetry. Both polarizations achieve an average gain of 14.5 dBi, with a maximum cross-polarization level lower than −15 dB within the operational frequency band. Gapwaveguide-based phased array antennas can be used to exploit the polarization diversity of the propagation channel due to radiated field orthogonality, while at the same time potentially reducing the interference footprint due to reduced side lobe levels.

- A novel, simple, and low-profile 45°-polarized phased array antenna element is introduced. This innovative solution, requiring only two layers, enables a full scanning range in azimuth. The proposed design addresses the challenges of achieving high inter-element isolation, reducing the inter-element distance to $0.56\lambda_0$, and accommodating larger space requirements for rotating slots than vertical slots, which was helpful in achieving better antenna element-to-element isolation. This design advancement contributes to the feasibility of gapwaveguide-based phased arrays with slant polarization.

- The thesis presents a $16 \times 16$ elements phased array operating at the 28 GHz band for high-power high-data-rate 5G applications. A printed circuit board (PCB) with a reduced layer count is employed for the phased array to make it cost-efficient. In contrast to typical wideband phased arrays with 12 PCB layers, the proposed design utilizes only 6 layers. This significant reduction in layer count is achieved by separating the radiating elements of the phased array from the PCB. By adopting this approach, the wideband characteristics of waveguide antennas are maintained while accommodating the large $16 \times 16$ array configuration. Furthermore, the phased array incorporates up/down converters, 1×4 TRX beamformer ICs, and gapwaveguide-based antenna elements. The system exhibits a wide steering range of ±60° in azimuth and ±10° in elevation. With a maximum EIRP of 65.5 dBm and a 3 dB bandwidth of $26.5 - 29.5$ GHz, the proposed phased array system demonstrates excellent performance

and reduced manufacturing complexity, making it an ideal candidate for compact deployment in practical 5G systems. The transmit error vector magnitude (EVM) performance of the slant-polarized gapwaveguide-based phased array is also investigated through non-standardized OTA link measurements. The array showcases high-data-rate transmission capabilities at high EIRP, with a measured EVM of 2.6% during the transmission of modulated signals over a 3 Gbps link at 60.5 dB EIRP.

- The thesis presents the design and experimental verification of a compact, high-EIRP phased array based on GaN high-power amplifiers and gapwaveguide antenna technology. The feasibility of a low-cost GaN-based analog beamforming phased array is experimentally demonstrated. The research outlines a design approach based on the system performance of a compact phased array with analog beamforming capabilities combining various semiconductor technologies. The fully metallic phased array antenna operates within the $26.5 - 29.5$ GHz frequency range, supporting a scanning range of $\pm 60^\circ$ in the azimuth plane. The proposed design improves upon previous approaches by offering efficient heat dissipation and high EIRP output with a relatively small array size of $8 \times 8$ elements. The antenna system holds potential as a cost-effective and highly efficient base station for 5G wireless communications.

- The performance of the proposed phased array antennas in indoor environment channel models is evaluated for high-data-rate communication in mmWave 5G. The findings demonstrate that distributed phased array antenna deployment consistently achieves higher achievable sum rate capacities compared to collocated phased array antennas. The configuration of analog beams and the choice of digital precoding scheme also impact performance, with narrower beams and zero-forcing precoding offering advantages in certain scenarios. Selecting the appropriate phased array antenna for indoor wireless communication requires considering multiple parameters beyond high EIRP to ensure effective high-data-rate communication.

## 6.2 Directions for further research

1. Simplifying the slot layer in a $45^\circ$ slant polarized phased array: One potential direction for future research is to explore design methods that simplify the manufacturing process of the slot layer in a $45^\circ$ slant-polarized phased array. Investigating a design in which the ridge gapwaveguide directly feeds $45^\circ$ slanted slots can employ an alternative manufacturing approach, such as using 2D processes like etching. This research could focus on optimizing the design and fabrication methods to achieve similar or improved performance while simplifying the manufacturing steps.

2. Designing a phased array based on gapwaveguide technology at 60 GHz:

While this thesis primarily focuses on the 28 GHz frequency band, as a widely licensed frequency band for mmWave 5G for indoor applications, another promising frequency band for indoor communications is 60 GHz. In this frequency range, there are opportunities for high data rate communication and the potential to overcome some of the challenges associated with lower frequency bands. Designing a phased array based on gapwaveguide technology for the 60 GHz frequency band would be an exciting avenue to explore. This research could involve designing and optimizing antenna elements, beamforming techniques, and performance analysis specific to the 60 GHz frequency band, considering factors such as path loss, interference, and propagation characteristics in indoor environments.

3. Analysis of the uplink of the proposed 28-GHz phased array antennas: In this thesis, two 28-GHz phased array antennas were designed, and their downlink performance is analyzed in the indoor environment. Further research can extend the analysis to include the uplink aspect of these antennas. This analysis would involve studying the beamforming techniques, power control mechanisms, and signal transmission characteristics in the uplink scenario. It would also consider factors such as UE power requirements, added noise by the phased arrays, multi-user scenarios, and channel conditions. This research would provide valuable insights into the overall system performance, including power consumption, signal quality, interference mitigation, SINR, and achievable sum rate capacity.

4. Determining SINR and maximum achievable sum-rate capacity in the indoor environment with +/-45° slant polarizations and random UE orientation: To assess the performance of phased arrays in indoor environments, it would be valuable to investigate the impact of various factors on the signal-to-interference-plus-noise ratio (SINR) and the maximum achievable sum-rate capacity. Specifically, analyzing the scenarios where the phased arrays have both +45 and -45° polarizations and the user equipment (UE) has a random orientation would provide insights into the system's performance in practical deployment scenarios. This research would involve characterizing the antenna radiation patterns, modeling the indoor environment, and accounting for polarization and orientation effects to determine the reliability and coverage of the link using the SINR and maximum achievable sum-rate capacity. The findings would aid in optimizing system parameters, such as antenna configuration and beamforming strategies, to enhance the performance of indoor mmWave communication systems.

5. Experimental verification of indoor analyses: To validate the analytical and simulation-based findings presented in chapter 5, conducting experimental verification in real-world indoor environments would be a valuable next step. This research would involve setting up testbeds to measure

the performance of the designed phased arrays, evaluating the system's performance metrics, and comparing them with the theoretical analyses. Experimental verification would provide practical insights into the system's behavior, validate the accuracy of the proposed designs, and identify potential areas for further improvement.

Overall, these suggestions for further research aim to expand upon the research presented in this thesis by extending the analysis to different frequency bands, assessing uplink performance, considering practical deployment scenarios, and validating the theoretical findings through experimental verification. These research directions would contribute to advancing gapwaveguide-based phased arrays for mmWave communication systems, particularly in indoor environments.

# Appendix A

# Mathematical derivations and proofs

## A.1 Derivation of SINR formula

Using Eq. (5.3), the total received signal by $k$-th UE, $y_k$, can be written as

$$\begin{aligned} y_k &= \mathbf{H}_{k:}\sqrt{G_{RF}}\mathbf{p} + n_k \\ &= \mathbf{H}_{k:}\sqrt{G_{RF}}\mathbf{W}\mathbf{x} + n_k \\ &= \underbrace{\mathbf{H}_{k:}\sqrt{G_{RF}}\mathbf{W}_{:k}x_k}_{\text{received signal}} + \underbrace{\sum_{k'\neq k}^{K}\mathbf{H}_{k:}\sqrt{G_{RF}}\mathbf{W}_{:k'}x_{k'}}_{\text{interference}} + \underbrace{n_k}_{\text{noise}}, \end{aligned} \tag{A.1}$$

where $\mathbf{H}_{k:}$ is the $k$-th row of matrix $\mathbf{H}$ and $\mathbf{W}_{:k}$ is the $k$-th column of matrix $\mathbf{W}$. The transmit signals $x_k$ are uncorrelated and have unit power. Therefore, the power of a received signal by $k$-th UE can be written as

$$\mathrm{E}\left\{|y_k|^2\right\} = \underbrace{G_{RF}\left|\mathbf{H}_{k:}\mathbf{W}_{:k}\right|^2}_{\text{received signal}} + \underbrace{G_{RF}\sum_{k'\neq k}^{K}\left|\mathbf{H}_{k:}\mathbf{W}_{:k'}\right|^2}_{\text{interference}} + \underbrace{\sigma_n^2}_{\text{noise}}. \tag{A.2}$$

Hence the SINR for $k$-th UE can be written as

$$\begin{aligned} \mathrm{SINR}_k &= \frac{S_k}{I_k + N_k} \\ &= \frac{G_{RF}\left|\mathbf{H}_{k:}\mathbf{W}_{:k}\right|^2}{G_{RF}\sum_{k'\neq k}^{K}\left|\mathbf{H}_{k:}\mathbf{W}_{:k'}\right|^2 + \sigma_n^2} \end{aligned} \tag{A.3}$$

By replacing the ZF's precoding matrix definition in Eq. (5.4) into Eq. (A.3),

as following:

$$\begin{aligned}\mathbf{y} &= \mathbf{H}\sqrt{G_{RF}}\mathbf{W}\mathbf{x} + \mathbf{n} \\ &= \sqrt{G_{RF}}\frac{\mathbf{H}\mathbf{H}^{\dagger}\left(\mathbf{H}\mathbf{H}^{\dagger}\right)^{-1}}{\left\|\mathbf{H}^{\dagger}\left(\mathbf{H}\mathbf{H}^{\dagger}\right)^{-1}\right\|_F}\mathbf{x} + \mathbf{n} \\ &= \sqrt{G_{RF}}\frac{\mathbf{I}_K}{\left\|\mathbf{H}^{\dagger}\left(\mathbf{H}\mathbf{H}^{\dagger}\right)^{-1}\right\|_F}\mathbf{x} + \mathbf{n},\end{aligned} \tag{A.4}$$

where $\mathbf{I}_K$ is the identity matrix of size $K$, the received signal by $k$-th UE can be written as,

$$y_k = \frac{\sqrt{G_{RF}}}{\left\|\mathbf{H}^{\dagger}\left(\mathbf{H}\mathbf{H}^{\dagger}\right)^{-1}\right\|_F}x_k + n_k. \tag{A.5}$$

This equation shows that using the ZF precoding, there will be no interference at the UE locations.

## A.2 Relation between $G_{RF}$ and transmit signal powers

The power of linearly precoded transmit signal $p_m$ is

$$\begin{aligned}\mathrm{E}\left\{|p_m|^2\right\} &= \mathrm{E}\left\{|\mathbf{W}_{m:}\mathbf{x}|^2\right\} \\ &= \mathrm{E}\left\{\mathbf{W}_{m:}\mathbf{x}\mathbf{x}^{\dagger}\mathbf{W}_{m:}^{\dagger}\right\} \\ &= \mathbf{W}_{m:}\mathrm{E}\left\{\mathbf{x}\mathbf{x}^{\dagger}\right\}\mathbf{W}_{m:}^{\dagger} \\ &= \mathbf{W}_{m:}\mathbf{I}_K\mathbf{W}_{m:}^{\dagger} \\ &= \left\|\mathbf{W}_{m:}\right\|^2.\end{aligned} \tag{A.6}$$

$\mathrm{E}\left\{|s_m|^2\right\}$ can be written as (see Fig. 5.1)

$$\mathrm{E}\left\{|s_m|^2\right\} = G_{RF}\mathrm{E}\left\{|p_m|^2\right\} = G_{RF}\left\|\mathbf{W}_{m:}\right\|^2. \tag{A.7}$$

The sum of all the power of linearly precoded transmit signals can be computed as

$$\begin{aligned}\sum_{m=1}^{M}\mathrm{E}\left\{|p_m|^2\right\} &= \sum_{m=1}^{M}\left\|\mathbf{W}_{m:}\right\|^2 \\ &= \left\|\mathbf{W}\right\|_F \\ &= 1,\end{aligned} \tag{A.8}$$

which is due to the normalization of the precoding matrix $\mathbf{W}$. Therefore it can be shown that the total conductive transmit power is

$$\sum_{m=1}^{M} \mathrm{E}\left\{|s_m|^2\right\} = G_{RF}. \tag{A.9}$$

## A.3 Proving $\mathrm{SINR}_k$ is an increasing function of $G_{RF}$

Let us rewrite Eq. (A.3) as below

$$\mathrm{SINR}_k = \frac{G_{RF} S_{k0}}{G_{RF} I_{k0} + N_k}, \tag{A.10}$$

where $S_{k0} = |\mathbf{H}_{k:}\mathbf{W}_{:k}|^2 > 0$, $I_{k0} = \sum_{k' \neq k}^{K} |\mathbf{H}_{k:}\mathbf{W}_{:k'}|^2 \geq 0$ and $N_k > 0$. Because $G_{RF}$ and $\mathbf{W}$ are independent, $G_{RF}$ is also independent of $S_{k0}$ and $I_{k0}$. The derivative of $\mathrm{SINR}_k$ of $G_{RF}$ is

$$\frac{\mathrm{dSINR}_k}{\mathrm{d}G_{RF}} = \frac{S_{k0} N_k}{\left(G_{RF} I_{k0} + N_k\right)^2}, \tag{A.11}$$

which is always greater than zero. Therefore $\mathrm{SINR}_k$ is an increasing function of $G_{RF}$.

# References


[1] Ericsson, "Leveraging the potential of 5G millimeter wave," 2021. [Online]. Available: https://www.ericsson.com/en/reports-and-papers/further-insights/leveraging-the-potential-of-5g-millimeter-wave

[2] P. M. Asbeck, N. Rostomyan, M. Özen, B. Rabet, and J. A. Jayamon, "Power amplifiers for mm-wave 5G applications: Technology comparisons and CMOS-SOI demonstration circuits," *IEEE Transactions on Microwave Theory and Techniques*, vol. 67, no. 7, pp. 3099–3109, 2019.

[3] A. Vosoogh, *Compact RF Integration and Packaging Solutions Based on Metasurfaces for Millimeter-Wave Applications*. Ph.D. Thesis, Chalmers University of Technology, Gothenburg, Sweden, 2018. [Online]. Available: https://research.chalmers.se/publication/505301/file/505301_Fulltext.pdf

[4] Y. Niu, Y. Li, D. Jin, L. Su, and A. V. Vasilakos, "A survey of millimeter wave communications (mmWave) for 5G: opportunities and challenges," *Wireless networks*, vol. 21, no. 8, pp. 2657–2676, 2015.

[5] Accton, "The Emergence of 5G mmWave," 2022. [Online]. Available: https://www.accton.com/Technology-Brief/the-emergence-of-5g-mmwave/

[6] I. Ahmed, H. Khammari, A. Shahid, A. Musa, K. S. Kim, E. De Poorter, and I. Moerman, "A survey on hybrid beamforming techniques in 5G: Architecture and system model perspectives," *IEEE Communications Surveys & Tutorials*, vol. 20, no. 4, pp. 3060–3097, 2018.

[7] S. A. Busari, K. M. S. Huq, S. Mumtaz, L. Dai, and J. Rodriguez, "Millimeter-wave massive MIMO communication for future wireless systems: A survey," *IEEE Communications Surveys & Tutorials*, vol. 20, no. 2, pp. 836–869, 2017.

[8] J. Zhang, X. Yu, and K. B. Letaief, "Hybrid beamforming for 5G and beyond millimeter-wave systems: A holistic view," *IEEE Open Journal of the Communications Society*, vol. 1, pp. 77–91, 2019.

[9] A. F. Molisch, V. V. Ratnam, S. Han, Z. Li, S. L. H. Nguyen, L. Li, and K. Haneda, "Hybrid beamforming for massive MIMO: A survey," *IEEE Communications magazine*, vol. 55, no. 9, pp. 134–141, 2017.

[10] S. Kutty and D. Sen, "Beamforming for millimeter wave communications: An inclusive survey," *IEEE communications surveys & tutorials*, vol. 18, no. 2, pp. 949–973, 2015.

[11] S. Han, I. Chih-Lin, Z. Xu, and C. Rowell, "Large-scale antenna systems with hybrid analog and digital beamforming for millimeter wave 5G," *IEEE Communications Magazine*, vol. 53, no. 1, pp. 186–194, 2015.

[12] G. Federico, D. Caratelli, G. Theis, and A. Smolders, "A review of antenna array technologies for point-to-point and point-to-multipoint wireless communications at millimeter-wave frequencies," *International Journal of Antennas and Propagation*, vol. 2021, pp. 1–18, 2021.

[13] K. Kibaroglu, M. Sayginer, T. Phelps, and G. M. Rebeiz, "A 64-element 28-GHz phased-array transceiver with 52-dBm EIRP and 8–12-Gb/s 5G link at 300 meters without any calibration," *IEEE Transactions on Microwave Theory and Techniques*, vol. 66, no. 12, pp. 5796–5811, 2018.

[14] A. Nafe, M. Sayginer, K. Kibaroglu, and G. M. Rebeiz, "2×64-element dual-polarized dual-beam single-aperture 28-GHz phased array with 2×30 Gb/s links for 5G polarization MIMO," *IEEE Transactions on Microwave Theory and Techniques*, vol. 68, no. 9, pp. 3872–3884, 2020.

[15] K. Klionovski, M. S. Sharawi, and A. Shamim, "A dual-polarization-switched beam patch antenna array for millimeter-wave applications," *IEEE Transactions on Antennas and Propagation*, vol. 67, no. 5, pp. 3510–3515, 2019.

[16] X. Gu, D. Liu, C. Baks, O. Tageman, B. Sadhu, J. Hallin, L. Rexberg, P. Parida, Y. Kwark, and A. Valdes-Garcia, "Development, implementation, and characterization of a 64-element dual-polarized phased-array antenna module for 28-GHz high-speed data communications," *IEEE Transactions on Microwave Theory and Techniques*, vol. 67, no. 7, pp. 2975–2984, 2019.

[17] J. Pang, R. Wu, Y. Wang, M. Dome, H. Kato, H. Huang, A. T. Narayanan, H. Liu, B. Liu, T. Nakamura *et al.*, "A 28-GHz CMOS phased-array transceiver based on LO phase-shifting architecture with gain invariant phase tuning for 5G new radio," *IEEE Journal of Solid-State Circuits*, vol. 54, no. 5, pp. 1228–1242, 2019.

[18] D. Caratelli, A. Al-Rawi, J. Song, and D. Favreau, "Dielectric Resonator Antenna Arrays for 5G Wireless Communications." *Microwave Journal*, vol. 63, no. 2, 2020.

[19] C. Bencivenni, T. Emanuelsson, and M. Gustafsson, "Gapwaves platform integrates 5G mmwave arrays," *Microwave Journal*, vol. 62, no. 2, 2019.

[20] C. Bencivenni, M. Gustafsson, A. Haddadi, A. U. Zaman, and T. Emanuelsson, "5G mmWave beam steering antenna development and testing," in *2019 13th European Conference on Antennas and Propagation (EuCAP)*. IEEE, 2019, pp. 1–4.

[21] T. Mark, G. H. NG, and T. Roger, "A 2-by-2 sub-array for scalable 28GHz mmWave phased array horn antenna in 5G network," in *2019 13th European Conference on Antennas and Propagation (EuCAP)*. IEEE, 2019, pp. 1–5.

[22] D. Zhao, P. Gu, J. Zhong, N. Peng, M. Yang, Y. Yi, J. Zhang, P. He, Y. Chai, Z. Chen *et al.*, "Millimeter-wave integrated phased arrays," *IEEE Transactions on Circuits and Systems I: Regular Papers*, vol. 68, no. 10, pp. 3977–3990, 2021.

[23] H.-T. Kim, B.-S. Park, S.-S. Song, T.-S. Moon, S.-H. Kim, J.-M. Kim, J.-Y. Chang, and Y.-C. Ho, "A 28-GHz CMOS Direct Conversion Transceiver With Packaged 2 × 4 Antenna Array for 5G Cellular System," *IEEE Journal of Solid-State Circuits*, vol. 53, no. 5, pp. 1245–1259, 2018.

[24] Y. Wang, R. Wu, J. Pang, D. You, A. A. Fadila, R. Saengchan, X. Fu, D. Matsumoto, T. Nakamura, R. Kubozoe *et al.*, "A 39-GHz 64-element phased-array transceiver with built-in phase and amplitude calibrations for large-array 5G NR in 65-nm CMOS," *IEEE Journal of Solid-State Circuits*, vol. 55, no. 5, pp. 1249–1269, 2020.

[25] K. Kibaroglu, M. Sayginer, A. Nafe, and G. M. Rebeiz, "A dual-polarized dual-beam 28 GHz beamformer chip demonstrating a 24 Gbps 64-QAM 2 × 2 MIMO link," in *2018 IEEE Radio Frequency Integrated Circuits Symposium (RFIC)*. IEEE, 2018, pp. 64–67.

[26] B. Sadhu, Y. Tousi, J. Hallin, S. Sahl, S. K. Reynolds, Ö. Renström, K. Sjögren, O. Haapalahti, N. Mazor, B. Bokinge *et al.*, "A 28-GHz 32-element TRX phased-array IC with concurrent dual-polarized operation and orthogonal phase and gain control for 5G communications," *IEEE Journal of Solid-State Circuits*, vol. 52, no. 12, pp. 3373–3391, 2017.

[27] A. Inoue, "Millimeter-Wave GaN Devices for 5G: Massive MIMO Antenna Arrays for Sub-6-GHz and mm-Wave Bandwidth," *IEEE Microwave Magazine*, vol. 22, no. 5, pp. 100–110, 2021.

[28] A. Hajimiri, A. Komijani, A. Natarajan, R. Chunara, X. Guan, and H. Hashemi, "Phased array systems in silicon," *IEEE Communications Magazine*, vol. 42, no. 8, pp. 122–130, 2004.

[29] A. Hajimiri, H. Hashemi, A. Natarajan, X. Guan, and A. Komijani, "Integrated phased array systems in silicon," *Proceedings of the IEEE*, vol. 93, no. 9, pp. 1637–1655, 2005.

[30] K. Kibaroglu, M. Sayginer, and G. M. Rebeiz, "A quad-core 28–32 GHz transmit/receive 5G phased-array IC with flip-chip packaging in SiGe BiCMOS," in *2017 IEEE MTT-S International Microwave Symposium (IMS)*. IEEE, 2017, pp. 1892–1894.

[31] J. Pang, Z. Li, R. Kubozoe, X. Luo, R. Wu, Y. Wang, D. You, A. A. Fadila, R. Saengchan, T. Nakamura, J. Alvin, D. Matsumoto, B. Liu, A. T. Narayanan, J. Qiu, H. Liu, Z. Sun, H. Huang, K. K. Tokgoz, K. Motoi, N. Oshima, S. Hori, K. Kunihiro, T. Kaneko, A. Shirane, and K. Okada, "A 28-GHz CMOS Phased-Array Beamformer Utilizing Neutralized Bi-Directional Technique Supporting Dual-Polarized MIMO for 5G NR," *IEEE Journal of Solid-State Circuits*, vol. 55, no. 9, pp. 2371–2386, 2020.

[32] X. Gu, D. Liu, C. Baks, O. Tageman, B. Sadhu, J. Hallin, L. Rexberg, and A. Valdes-Garcia, "A multilayer organic package with 64 dual-polarized antennas for 28GHz 5G communication," in *2017 IEEE MTT-S International Microwave Symposium (IMS)*. IEEE, 2017, pp. 1899–1901.

[33] Y. Yin, Z. Zhang, T. Kanar, S. Zihir, and G. M. Rebeiz, "A 24-29.5 GHz 256-element 5G phased-array with 65.5 dBm peak EIRP and 256-QAM modulation," in *2020 IEEE/MTT-S International Microwave Symposium (IMS)*. IEEE, 2020, pp. 687–690.

[34] Y. Yin, B. Ustundag, K. Kibaroglu, M. Sayginer, and G. M. Rebeiz, "Wideband 23.5–29.5-GHz Phased Arrays for Multistandard 5G Applications and Carrier Aggregation," *IEEE Transactions on Microwave Theory and Techniques*, vol. 69, no. 1, pp. 235–247, 2021.

[35] A. Nafe, M. Sayginer, K. Kibaroglu, and G. M. Rebeiz, "2x64 dual-polarized dual-beam single-aperture 28 GHz phased array with high cross-polarization rejection for 5G polarization MIMO," in *2019 IEEE MTT-S International Microwave Symposium (IMS)*. IEEE, 2019, pp. 484–487.

[36] J. Liu, A. Vosoogh, A. U. Zaman, and J. Yang, "A slot array antenna with single-layered corporate-feed based on ridge gap waveguide in the 60 GHz band," *IEEE Transactions on Antennas and Propagation*, vol. 67, no. 3, pp. 1650–1658, 2018.

[37] A. Vosoogh, P.-S. Kildal, and V. Vassilev, "Wideband and high-gain corporate-fed gap waveguide slot array antenna with ETSI class II radiation pattern in *v*-band," *IEEE Transactions on Antennas and Propagation*, vol. 65, no. 4, pp. 1823–1831, 2016.

[38] L. Li, J. Chen, L. Kong, P. Zhang, Q. Lv, B. Zhang, B. Tian, and C. Jin, "W-band ridge gap waveguide slot array antenna with low sidelobe and high-gain characteristics," *Microwave and Optical Technology Letters*, vol. 64, no. 3, pp. 565–570, 2022.

[39] P.-S. Kildal, E. Alfonso, A. Valero-Nogueira, and E. Rajo-Iglesias, "Local metamaterial-based waveguides in gaps between parallel metal plates," *IEEE Antennas and Wireless Propagation Letters*, vol. 8, pp. 84–87, 2009.

[40] P.-S. Kildal, "Metasurfing since 1987-a personal story involving soft and hard surfaces, EBG surfaces, cloaking, gap waveguides and mass production," in *2014 IEEE Antennas and Propagation Society International Symposium (APSURSI)*. IEEE, 2014, pp. 529–530.

[41] P.-S. Kildal, A. U. Zaman, E. Rajo-Iglesias, E. Alfonso, and A. Valero-Nogueira, "Design and experimental verification of ridge gap waveguide in bed of nails for parallel-plate mode suppression," *IET Microwaves, Antennas & Propagation*, vol. 5, no. 3, pp. 262–270, 2011.

[42] M. Khalily, R. Tafazolli, P. Xiao, and A. A. Kishk, "Broadband mm-wave microstrip array antenna with improved radiation characteristics for different 5G applications," *IEEE Transactions on Antennas and Propagation*, vol. 66, no. 9, pp. 4641–4647, 2018.

[43] P. A. Dzagbletey and Y.-B. Jung, "Stacked microstrip linear array for millimeter-wave 5G baseband communication," *IEEE Antennas and Wireless Propagation Letters*, vol. 17, no. 5, pp. 780–783, 2018.

[44] B. Molaei and A. Khaleghi, "A novel wideband microstrip line to ridge gap waveguide transition using defected ground slot," *IEEE Microwave and Wireless Components Letters*, vol. 25, no. 2, pp. 91–93, 2015.

[45] A. A. Brazález, J. Flygare, J. Yang, V. Vassilev, M. Baquero-Escudero, and P.-S. Kildal, "Design of *F*-Band Transition From Microstrip to Ridge Gap Waveguide Including Monte Carlo Assembly Tolerance Analysis," *IEEE Transactions on Microwave Theory and Techniques*, vol. 64, no. 4, pp. 1245–1254, 2016.

[46] A. U. Zaman, T. Vukusic, M. Alexanderson, and P.-S. Kildal, "Design of a simple transition from microstrip to ridge gap waveguide suited for MMIC and antenna integration," *IEEE Antennas and wireless propagation letters*, vol. 12, pp. 1558–1561, 2013.

[47] S. Peng, Y. Pu, W. Shao, X. Wang, and Y. Luo, "A Broadband Ridge Gap Waveguide to Micro-strip Transition Using Probe Current Coupling," in *2019 International Vacuum Electronics Conference (IVEC)*. IEEE, 2019, pp. 1–2.

[48] Z. Liu and D. Sun, "Transition from rectangular waveguide to empty substrate integrated gap waveguide," *Electronics Letters*, vol. 55, no. 11, pp. 654–656, 2019.

[49] C. Bencivenni, A. U. Zaman, A. Haddadi, and T. Emanuelsson, "Towards Integrated Active Antennas for 5G mm-wave Applications at Gapwaves," in *2018 IEEE International Symposium on Antennas and Propagation & USNC/URSI National Radio Science Meeting*. IEEE, 2018, pp. 415–416.

[50] Y.-C. Shih, T.-N. Ton, and L. Q. Bui, "Waveguide-to-microstrip transitions for millimeter-wave applications," in *1988., IEEE MTT-S International Microwave Symposium Digest*. IEEE, 1988, pp. 473–475.

[51] Y.-C. Leong and S. Weinreb, "Full band waveguide-to-microstrip probe transitions," in *1999 IEEE MTT-S International Microwave Symposium Digest (Cat. No. 99CH36282)*, vol. 4. IEEE, 1999, pp. 1435–1438.

[52] J. Zhu, S. Liao, S. Li, and Q. Xue, "60 GHz substrate-integrated waveguide-based monopulse slot antenna arrays," *IEEE Transactions on Antennas and Propagation*, vol. 66, no. 9, pp. 4860–4865, 2018.

[53] T. Tomura, Y. Miura, M. Zhang, J. Hirokawa, and M. Ando, "A 45° Linearly Polarized Hollow-Waveguide Corporate-Feed Slot Array Antenna in the 60-GHz Band," *IEEE Transactions on Antennas and Propagation*, vol. 60, no. 8, pp. 3640–3646, 2012.

[54] M. Ferrando-Rocher, J. I. Herranz-Herruzo, A. Valero-Nogueira, B. Bernardo-Clemente, A. U. Zaman, and J. Yang, "8×8 Ka-Band Dual-Polarized Array Antenna based on Gap Waveguide Technology," *IEEE Transactions on Antennas and Propagation*, 2019.

[55] D.-y. Kim, W.-S. Chung, C.-H. Park, S.-J. Lee, and S. Nam, "A Series Slot Array Antenna for 45°-Inclined Linear Polarization With SIW Technology," *IEEE Transactions on Antennas and Propagation*, vol. 60, no. 4, pp. 1785–1795, 2012.

[56] H. Iizuka, T. Watanabe, K. Sato, and K. Nishikawa, "Millimeter-wave microstrip array antenna for automotive radars," *IEICE transactions on communications*, vol. 86, no. 9, pp. 2728–2738, 2003.

[57] EU Radio Spectrum Policy Group, "Strategic spectrum roadmap towards 5g for europe," https://circabc.europa.eu/sd/a/fe1a3338-b751-43e3-9ed8-a5632f051d1f/RSPG18-005final-2nd_opinion_on_5G.pdf, 2018, [Online].

[58] P. von Butovitsch, D. Astely, C. Friberg, A. Furuskär, B. Göransson, B. Hogan, J. Karlsson, and E. Larsson, "Advanced antenna systems for 5G networks," *Ericsson White Paper*, 2018.

[59] J. Petersson, "Phased array antenna with series fed transverse slots based on gap-waveguide technology." M.Sc. Thesis, Chalmers University of Technology, Gothenburg, Sweden, 2018. [Online]. Available: https://hdl.handle.net/20.500.12380/304259

[60] E. Holzman, "On the use of dummy elements to match edge elements in transmit arrays," in *2013 IEEE International Symposium on Phased Array Systems and Technology*. IEEE, 2013, pp. 549–552.

[61] D. M. Pozar, "A relation between the active input impedance and the active element pattern of a phased array," *IEEE Transactions on Antennas and Propagation*, vol. 51, no. 9, pp. 2486–2489, 2003.

[62] J. Dunworth, B.-H. Ku, Y.-C. Ou, D. Lu, P. Mouat, A. Homayoun, K. Chakraborty, A. Arnett, G. Liu, T. Segoria *et al.*, "28GHz phased array transceiver in 28nm bulk CMOS for 5G prototype user equipment and base stations," in *2018 IEEE/MTT-S International Microwave Symposium-IMS*. IEEE, 2018, pp. 1330–1333.

[63] Y. Yin, S. Zihir, T. Kanar, Q. Ma, H. Chung, L. Gao, and G. M. Rebeiz, "A 37–42-GHz 8× 8 Phased-Array With 48–51-dBm EIRP, 64–QAM 30-Gb/s Data Rates, and EVM Analysis Versus Channel RMS Errors," *IEEE Transactions on Microwave Theory and Techniques*, vol. 68, no. 11, pp. 4753–4764, 2020.

[64] C.-N. Chen, Y.-H. Lin, L.-C. Hung, T.-C. Tang, W.-P. Chao, C.-Y. Chen, P.-H. Chuang, G.-Y. Lin, W.-J. Liao, Y.-H. Nien *et al.*, "38-GHz Phased Array Transmitter and Receiver Based on Scalable Phased Array Modules With Endfire Antenna Arrays for 5G MMW Data Links," *IEEE Transactions on Microwave Theory and Techniques*, vol. 69, no. 1, pp. 980–999, 2020.

[65] AWMF-0153, *26.5-29.5 GHz Tx/Rx Up and Down Converter IFIC*, Anokiwave.

[66] MMW9002KC, *26.5-29.5 GHz 4-Channel Analog Beamforming Integrated Circuit*, NXP Semiconductors. [Online]. Available: https://www.nxp.com/products/radio-frequency/rf-power/rf-cellular-infrastructure/5g-mmwave/26-5-29-5-ghz-4-channel-analog-beamforming-integrated-circuit:MMW9002KC

[67] T. Takahashi, Y. Konishi, S. Makino, H. Ohmine, and H. Nakaguro, "Fast measurement technique for phased array calibration," *IEEE Transactions on Antennas and Propagation*, vol. 56, no. 7, pp. 1888–1899, 2008.

[68] B. Yang, Z. Yu, R. Zhang, J. Zhou, and W. Hong, "Local oscillator phase shifting and harmonic mixing-based high-precision phased array for 5G millimeter-wave communications," *IEEE Transactions on Microwave Theory and Techniques*, vol. 67, no. 7, pp. 3162–3173, 2019.

[69] "5G NR Base Station (BS) radio transmission and reception," 3rd Generation Partnership Project, Tech. Rep. TR 38.104 V15.3.0, November 2018.

[70] B. Ustundag, K. Kibaroglu, M. Sayginer, and G. M. Rebeiz, "A wideband high-power multistandard 23–31 GHz 2×2 quad beamformer chip in SiGe with >15 dBm OP1dB per channel," in *2018 IEEE Radio Frequency Integrated Circuits Symposium (RFIC)*. IEEE, 2018, pp. 60–63.

[71] T. Kuwabara, N. Tawa, Y. Tone, and T. Kaneko, "A 28 GHz 480 elements digital AAS using GaN HEMT amplifiers with 68 dBm EIRP for 5G long-range base station applications," in *2017 IEEE Compound Semiconductor Integrated Circuit Symposium (CSICS)*. IEEE, 2017, pp. 1–4.

[72] L. Belostotski and S. Jagtap, "Down with noise: an introduction to a low-noise amplifier survey," *IEEE Solid-State Circuits Magazine*, vol. 12, no. 2, pp. 23–29, 2020.

[73] R. J. Mailloux, *Phased array antenna handbook*. Artech house, 2017.

[74] H. Wang, P. M. Asbeck, and C. Fager, "Millimeter-wave power amplifier integrated circuits for high dynamic range signals," *IEEE Journal of Microwaves*, vol. 1, no. 1, pp. 299–316, 2021.

[75] QPF4001, *26-30 GHz 1 Watt GaN Front End Module*, Qorvo.

[76] QPF4002, *26-30 GHz 1 Watt GaN Dual Channel Front End Module*, Qorvo.

[77] P.-S. Kildal, E. Alfonso, A. Valero-Nogueira, and E. Rajo-Iglesias, "Local metamaterial-based waveguides in gaps between parallel metal plates," *IEEE Antennas and wireless propagation letters*, vol. 8, pp. 84–87, 2008.

[78] A. U. Zaman, M. Alexanderson, T. Vukusic, and P.-S. Kildal, "Gap waveguide PMC packaging for improved isolation of circuit components in high-frequency microwave modules," *IEEE Transactions on Components, Packaging and Manufacturing Technology*, vol. 4, no. 1, pp. 16–25, 2013.

[79] G. Magalhães, J. León, and M. de Menezes, "A Novel Calibration Method for Phased-Array Radar based on Element-wise Time Offsetting and Multi-Element Phase Toggle," in *2019 IEEE Radar Conference (RadarConf)*. IEEE, 2019, pp. 1–6.

[80] Y. Yin, B. Ustundag, K. Kibaroglu, M. Sayginer, and G. M. Rebeiz, "Wideband 23.5–29.5-GHz phased arrays for multistandard 5G applications and carrier aggregation," *IEEE Transactions on Microwave Theory and Techniques*, vol. 69, no. 1, pp. 235–247, 2020.

[81] S. Rangan, T. S. Rappaport, and E. Erkip, "Millimeter-wave cellular wireless networks: Potentials and challenges," *Proceedings of the IEEE*, vol. 102, no. 3, pp. 366–385, 2014.

[82] A. Ghosh, T. A. Thomas, M. C. Cudak, R. Ratasuk, P. Moorut, F. W. Vook, T. S. Rappaport, G. R. MacCartney, S. Sun, and S. Nie, "Millimeter-wave enhanced local area systems: A high-data-rate approach for future wireless networks," *IEEE Journal on Selected Areas in Communications*, vol. 32, no. 6, pp. 1152–1163, 2014.

[83] J. Kim, M. Sung, S.-H. Cho, Y.-J. Won, B.-C. Lim, S.-Y. Pyun, J.-K. Lee, and J. H. Lee, "MIMO-supporting radio-over-fiber system and its application in mmWave-based indoor 5G mobile network," *Journal of Lightwave Technology*, vol. 38, no. 1, pp. 101–111, 2019.

[84] F. Rusek, D. Persson, B. K. Lau, E. G. Larsson, T. L. Marzetta, O. Edfors, and F. Tufvesson, "Scaling up MIMO: Opportunities and challenges with very large arrays," *IEEE Signal Processing Magazine*, vol. 30, no. 1, pp. 40–60, 2012.

[85] T. L. Marzetta, "Noncooperative cellular wireless with unlimited numbers of base station antennas," *IEEE Transactions on Wireless Communications*, vol. 9, no. 11, pp. 3590–3600, 2010.

[86] M. Xiao, S. Mumtaz, Y. Huang, L. Dai, Y. Li, M. Matthaiou, G. K. Karagiannidis, E. Björnson, K. Yang, I. Chih-Lin *et al.*, "Millimeter wave communications for future mobile networks," *IEEE Journal on Selected Areas in Communications*, vol. 35, no. 9, pp. 1909–1935, 2017.

[87] E. Bjornson, L. Van der Perre, S. Buzzi, and E. G. Larsson, "Massive MIMO in sub-6 GHz and mmWave: Physical, practical, and use-case differences," *IEEE Wireless Communications*, vol. 26, no. 2, pp. 100–108, 2019.

[88] N. Akbar, E. Björnson, E. G. Larsson, and N. Yang, "Downlink power control in massive MIMO networks with distributed antenna arrays," in *2018 IEEE International Conference on Communications (ICC)*. IEEE, 2018, pp. 1–6.

[89] D. Wang, J. Wang, X. You, Y. Wang, M. Chen, and X. Hou, "Spectral efficiency of distributed MIMO systems," *IEEE Journal on Selected Areas in Communications*, vol. 31, no. 10, pp. 2112–2127, 2013.

[90] C.-X. Wang, F. Haider, X. Gao, X.-H. You, Y. Yang, D. Yuan, H. M. Aggoune, H. Haas, S. Fletcher, and E. Hepsaydir, "Cellular architecture and key technologies for 5G wireless communication networks," *IEEE Communications Magazine*, vol. 52, no. 2, pp. 122–130, 2014.

[91] G. N. Kamga, M. Xia, and S. Aïssa, "Spectral-efficiency analysis of massive MIMO systems in centralized and distributed schemes," *IEEE Transactions on Communications*, vol. 64, no. 5, pp. 1930–1941, 2016.

[92] C.-M. Chen, A. P. Guevara, and S. Pollin, "Scaling up distributed massive MIMO: Why and how," in *2017 51st Asilomar Conference on Signals, Systems, and Computers*. IEEE, 2017, pp. 271–276.

[93] X.-H. You, D.-M. Wang, B. Sheng, X.-Q. Gao, X.-S. Zhao, and M. Chen, "Cooperative distributed antenna systems for mobile communications [coordinated and distributed MIMO]," *IEEE Wireless Communications*, vol. 17, no. 3, pp. 35–43, 2010.

[94] D.-W. Yue and H. H. Nguyen, "Multiplexing gain analysis of mmWave massive MIMO systems with distributed antenna subarrays," *IEEE Transactions on Vehicular Technology*, vol. 68, no. 11, pp. 11 368–11 373, 2019.

[95] S. F. Islam, "Distributed massive MIMO in millimetre wave communication," Ph.D. dissertation, University of York, 2022.

[96] N. Sheng, J. Zhang, F. Zhang, and L. Tian, "Downlink performance of indoor distributed antenna systems based on wideband MIMO measurement at 5.25 GHz," in *2011 IEEE Vehicular Technology Conference (VTC Fall)*. IEEE, 2011, pp. 1–5.

[97] M. Arnold, P. Baracca, T. Wild, F. Schaich, and S. ten Brink, "Measured distributed vs co-located massive MIMO in industry 4.0 environments," in *2021 Joint European Conference on Networks and Communications & 6G Summit (EuCNC/6G Summit)*. IEEE, 2021, pp. 306–310.

[98] T. Choi, P. Luo, A. Ramesh, and A. F. Molisch, "Co-located vs distributed vs semi-distributed MIMO: Measurement-based evaluation," in *2020 54th Asilomar Conference on Signals, Systems, and Computers*. IEEE, 2020, pp. 836–841.

[99] J. R. Pérez, Ó. Fernández, L. Valle, A. Bedoui, M. Et-tolba, and R. P. Torres, "Experimental analysis of concentrated versus distributed massive MIMO in an indoor cell at 3.5 GHz," *Electronics*, vol. 10, no. 14, p. 1646, 2021.

[100] S. Jeong, A. Farhang, F. Gao, and M. F. Flanagan, "Frequency synchronisation for massive MIMO: a survey," *IET Communications*, vol. 14, no. 16, pp. 2639–2645, 2020.

[101] S. Elhoushy and W. Hamouda, "Performance of distributed massive MIMO and small-cell systems under hardware and channel impairments," *IEEE Transactions on Vehicular Technology*, vol. 69, no. 8, pp. 8627–8642, 2020.

[102] Y.-H. Zhu, G. Callebaut, H. Çalık, L. Van der Perre, and F. Rottenberg, "Energy efficient access point placement for distributed massive MIMO," *Network*, vol. 2, no. 2, pp. 288–310, 2022.

[103] S. D. Van, H. Q. Ngo, and S. L. Cotton, "Wireless powered wearables using distributed massive MIMO," *IEEE Transactions on Communications*, vol. 68, no. 4, pp. 2156–2172, 2020.

[104] S. Jaeckel, L. Raschkowski, K. Börner, and L. Thiele, "QuaDRiGa: A 3-D multi-cell channel model with time evolution for enabling virtual field trials," *IEEE Transactions on Antennas and Propagation*, vol. 62, no. 6, pp. 3242–3256, 2014.

[105] S. Jaeckel, L. Raschkowski, K. Börner, L. Thiele, F. Burkhardt, and E. Eberlein, "QuaDRiGa - quasi deterministic radio channel generator, user manual and documentation," Fraunhofer Heinrich Hertz Institute, Tech. Rep. V2.6.1, 2021.

[106] "Study on channel model for frequencies from 0.5 to 100 GHz," 3rd Generation Partnership Project, Tech. Rep. TR 38.901 V14.1.0, June 2017.

[107] N. Fatema, G. Hua, Y. Xiang, D. Peng, and I. Natgunanathan, "Massive MIMO linear precoding: A survey," *IEEE Systems Journal*, vol. 12, no. 4, pp. 3920–3931, 2017.

[108] Y.-G. Lim, C.-B. Chae, and G. Caire, "Performance analysis of massive MIMO for cell-boundary users," *IEEE Transactions on Wireless Communications*, vol. 14, no. 12, pp. 6827–6842, 2015.

[109] T. Parfait, Y. Kuang, and K. Jerry, "Performance analysis and comparison of ZF and MRT based downlink massive MIMO systems," in *2014 Sixth International Conference on Ubiquitous and Future Networks (ICUFN)*. IEEE, 2014, pp. 383–388.

[110] Y. Han, S. Jin, J. Zhang, J. Zhang, and K.-K. Wong, "Analog beam selection schemes of DFT-based hybrid beamforming multiuser systems," in *2017 23rd Asia-Pacific Conference on Communications (APCC)*. IEEE, 2017, pp. 1–6.

[111] I. Hadj-Kacem, H. Braham, and S. B. Jemaa, "SINR and rate distributions for downlink cellular networks," *IEEE Transactions on Wireless Communications*, vol. 19, no. 7, pp. 4604–4616, 2020.

9 789036 557375